TECHNISCHE UNIVERSITÄT DRESDEN

Fakultät Umweltwissenschaften Institut für Siedlungs- und Industriewasserwirtschaft

Professur für Verfahrenstechnik in Hydrosystemen

Title of the Doctoral Thesis

The Treatment of Saline Solutions Utilizing Ceramic Membranes in Membrane Distillation Processes

Submitted in fulfilment of the requirements for the degree of
Doctor of Engineering (Dr.-Ing.)

Submitted by
M.Sc. Schnittger, Johann

Supervisors:

Prof. Dr.-Ing. André Lerch
Technische Universität Dresden, Institut für Siedlungs- und Industriewasserwirtschaft,
Professur für Verfahrenstechnik in Hydrosystemen, Dresden, Germany

Prof. Dr. rer. nat. Ingolf Voigt
Ernst-Abbe-University, Department SciTec, Jena, Germany
Fraunhofer Institute for Ceramic Technologies and Systems, Hermsdorf, Germany

Prof. Kuo-Lun Tung
National Taiwan University, Chemical Engineering, Membrane Filtration Laboratory,
Taipei City, Taiwan

Dresden, 25.11.2021

Dedicated to

Manuela Schnittger

Affidavit

I hereby declare that I have written the attached dissertation independently and have not used any other aids than those indicated. I have marked all the passages taken over literally or in terms of content as such. I also confirm that I have submitted the attached dissertation only in this and no other doctoral procedure and that this doctoral procedure has not been preceded by any definitively failed doctoral procedures.

Berlin, den

Eidesstattlicher Erklärung

Hiermit erkläre ich, dass ich die beigefügte Dissertation selbstständig verfasst und keine anderen als die angegebenen Hilfsmittel genutzt habe. Alle wörtlich oder inhaltlich übernommenen Stellen habe ich als solche gekennzeichnet. Ich versichere außerdem, dass ich die beigefügte Dissertation nur in diesem und keinem anderen Promotionsverfahren eingereicht habe und, dass diesem Promotionsverfahren keine endgültig gescheiterten Promotionsverfahren vorausgegangen sind.

Berlin, den

Abstract

Desalination has become one of the most important approaches to secure the fresh water supply for many regions and their significance is expected to gain further momentum with ongoing population growth, climate change and accelerated consumption. Despite their technical maturity conventional desalination processes exhibit limitations that manifest themselves in considerable ecological footprints or high economic costs. Therefore, unconventional desalination processes such as membrane distillation (MD) have been attracting significant attention from the scientific community offering benefits that could help to overcome some of these limitations.

MD is a thermally driven process that uses a hydrophobic membrane as a barrier between a warm liquid feed and a cooler permeate side allowing only vapor molecules to pass from the feed to the permeate side. As is the case for all membrane-based separation processes, the characteristics of the membranes utilized in MD mainly define the performance (mass transfer rate, rejection rate and energy efficiency) of the process and thus the commercial interest. Due to their intrinsic hydrophobic characteristics as well as their good mass transfer properties the utilization of polymeric membranes is state of the art in MD. However, in order to extend the areas of application of MD processes to aggressive solutions, thermally, mechanically and chemically robust membranes are required. While ceramic membranes offer a superior stability in comparison with polymeric membranes (which could facilitate the treatment of aggressive solutions with MD) research must yet demonstrate their suitability for MD processes as well as highlight approaches for membrane optimization.

For this work, a variety of different types of modified ceramic membranes (e.g. material and layer design) was fully characterized regarding their specific membrane properties (e.g. pore size, thermal conductivity and hydrophobic characteristics) and subsequently tested in direct contact membrane distillation (DCMD) and vacuum membrane distillation (VMD) treating synthetic and real saline solutions. This data was then used to calculate the mass transfer of asymmetric ceramic membranes using a VMD model (based on the Dusty-Gas Model) suggested by the literature and to assess the performance (i.e. stability, mass transfer, selectivity and energy efficiency) of modified ceramic membranes in MD in respect to specific membrane properties and operational parameters. Subsequently, the aptitude of ceramic membranes for MD processes could be evaluated and concepts for the optimization of ceramic membranes proposed. By doing that, a foundation was established that can help to boost the commercialization of ceramic membranes in MD.

Ceramic membranes were modified with several hydrophobic agents which led to the identification of a non-fluorinated hydrophobic molecule as a potential alternative to the fluorinated agents that

are commonly used. The liquid entry pressure (LEP) was determined to be higher than 2.5 bar for all membranes with pore sizes smaller or equal to 400 nm modified with fluorinated and non-fluorinated hydrophobic agents but showed a strong dependency on the testing solution characteristics. While symmetrically structured ceramic membranes modified with a fluorinated agent were the only membrane type robust enough to withstand the contact with a hot saline acidic solution over 96 hours, they showed considerably lower permeate fluxes in VMD than asymmetrically structured ceramic membranes. Modified asymmetrically structured ceramic membranes showed higher mass transfer rates in VMD than in DCMD. While the support properties mainly defined the extent of the mass transport of asymmetrically structured ceramic membranes in VMD, the mass transport in DCMD was considerably affected by the membrane layer characteristics (e.g. pore size of the final membrane layer). A VMD model suggested by the literature was successfully adapted using corrections factors to facilitate mass transfer calculations for asymmetrically structured TiO_2 membranes. TiO_2 and Al_2O_3 membranes were successfully used to treat highly saline solutions (synthetic and real) in VMD. However, TiO_2 membranes outperformed Al_2O_3 membranes in DCMD and VMD because they are less affected by temperature polarization due to their lower thermal conductivity. For instance, excellent rejections above 99.9 % and permeate fluxes of up to 35 kg/(m² h) were achieved treating a highly concentrated NaCl solution (350 g NaCl per kg H_2O) using a TiO_2 membrane (final pore size: 100 nm) in VMD. The mass transfer rates achieved using modified ceramic membranes in VMD were essentially competitive to the permeate fluxes of polymeric membranes determined under similar test conditions (derived from the literature). However, it was shown that the low energy efficiency of ceramic membranes remains a big obstacle for their commercialization in MD processes and must be the focal point of membrane optimization efforts.

Keywords

Ceramic membranes, contact angle, desalination, direct contact membrane distillation, energy efficiency, hydrophobic agent, liquid entry pressure, membrane layer design, membrane distillation, membrane modification, membrane stability, modelling, permeance, permeate flux, rejection, real solutions, saline solution, vacuum membrane distillation

Kurzfassung

Die Entsalzung ist eine der wichtigsten Technologien, um den Frischwasserbedarf in vielen Regionen der Welt sicherzustellen. Bevölkerungswachstum, der Klimawandel und stetig steigender Konsum werden die Bedeutung von Entsalzungstechnologien weiterwachsen lassen. Die Möglichkeit des Einsatzes etablierter konventioneller Verfahren wird begrenzt durch die hohen ökologischen und ökonomischen Kosten dieser Verfahren. Unkonventionelle Entsalzungsverfahren wie die Membrandestillation (MD) bieten einige Vorteile, mit denen sie konventionelle Verfahren jenseits dieser Limitationen ergänzen können. Die MD ist ein thermisch angetriebener Prozess, in welchem eine hydrophobe Membran das warme, flüssige Feed räumlich von der kälteren Permeatseite trennt, während nur dampfförmige Moleküle durch die Membran permeieren können. Wie in allen membranbasierten Trennprozessen bestimmen die Charakteristika der verwendeten Membran die Leistungsfähigkeit (Massentransport, Rückhaltevermögen und Energieeffizienz) des Prozesses und das damit verbundene kommerzielle Interesse. Durch ihre intrinsisch hydrophoben Materialeigenschaften und ihren guten Massentransfercharakteristika ist die Verwendung von Polymermembranen in der MD aktuell Stand der Technik. Um die Einsatzmöglichkeiten von MD Verfahren auf aggressive Lösungen zu erweitern, werden thermisch, mechanisch und chemisch stabile Membranen benötigt. Obwohl keramische Membranen im Vergleich zu Polymermembranen eine höhere Stabilität aufweisen (wodurch die Behandlung von aggressiven Lösungen mit MD-Verfahren prinzipiell möglich wird) muss die Eignung von keramischen Membranen für MD-Verfahren wissenschaftlich belegt und ein Konzept zur Membranoptimierung entwickelt werden.

Im Rahmen dieser Arbeit wurden verschiedene Typen modifizierter keramischer Membranen (z.B. Materialauswahl und Schichtaufbau) vollständig im Hinblick auf ihre spezifischen Membraneigenschaften (z.B. Porengröße, Wärmeleitfähigkeit und hydrophobe Eigenschaften) charakterisiert und anschließend unter Verwendung von salzhaltigen Lösungen in der Direktkontaktmembrandestillation (DCMD) und der Vakuummembrandestillation (VMD) getestet. Diese Daten wurden genutzt, um den Stofftransport von asymmetrischen keramischen Membranen unter Verwendung eines anerkannten VMD-Modells (basierend auf dem Dusty-Gas-Modell) zu berechnen und um die Leistungsfähigkeit (d.h. Stabilität, Stofftransport, Selektivität und Energieeffizienz) von modifizierten keramischen Membranen in der MD in Hinblick auf spezifische Membraneigenschaften und Verfahrensparameter zu bewerten. Anschließend wurde die Eignung von keramischen Membranen für MD-Prozesse evaluiert und Optimierungskonzepte für keramische Membranen vorgeschlagen. Damit wurde mit dieser Arbeit die Grundlage gelegt, die Kommerzialisierung von keramischen Membranen in der MD voranzutreiben.

Keramische Membranen wurde mit verschiedenen Molekülen hinsichtlich ihrer Oberflächeneigenschaften modifiziert. Dadurch konnte ein nicht-fluorisiertes Molekül als potenzielle Alternative zu den üblicherweise verwendeten fluorierten Molekülen identifiziert wurde. Für alle modifizierten Membranen (unabhängig von dem Hydrophobierungsmittel) mit Porengrößen kleiner oder gleich 400 nm, wurde ein Flüssigkeitseindringdruck (LEP) über 2,5 bar gemessen, welcher jedoch eine starke Abhängigkeit von den Eigenschaften der Testlösung zeigt. Während symmetrisch aufgebaute keramische Membranen modifiziert mit einem fluorierten Hydrophobierungsmittel die Behandlung mit heißer, salzhaltiger Lösung über 96 Stunden standhielten, zeigten diese deutlich geringere Permeatflüsse in der VMD als asymmetrisch strukturierte keramische Membranen. Der Stofftransport von asymmetrischen keramischen Membranen war in der VMD höher ausgeprägt als in der DCMD. Der Stofftransport von asymmetrischen keramischen Membranen wird in der VMD vorwiegend von den Supporteigenschaften beeinflusst, während der Strofftransport in der DCMD erheblich von den Eigenschaften der trennaktiven Membranschicht (z. B. die Porengröße) bestimmt wird. Ein in der Literatur beschriebenes VMD-Modell in Bezug vorhandener Defizite durch Korrekturfaktoren erfolgreich erweitert und zur Berechnung des Strofftransportes für asymmetrische TiO_2 Membranen angewandt. TiO_2 und Al_2O_3 Membranen wurden in der VMD erfolgreich zur Behandlung hochkonzentrierter Salzlösungen (synthetische und reale Lösungen) verwendet. TiO_2 Membranen zeigten höhere Permeateflüsse als Al_2O_3 Membranen in der DCMD und der VMD. Das begründet sich insbesondere bedingt durch die bessere Moderierung von Temperaturpolarisationseffekten aufgrund der geringen Wärmeleitfähigkeit von TiO_2 Membranen. Beispielsweise wurden bei der Behandlung einer hochkonzentrierte NaCl-Lösung (350 g NaCl pro kg H2O) mit einer TiO_2 Membran (Finale Porengröße: 100 nm) in der VMD hervorragende Salzrückhalte von über 99,9 % und Permeatflüsse von bis zu 35 kg/(m² h) erreicht. Die Stofftransportraten der modifizierten keramischen Membranen in der VMD sind im Vergleich zu den Permeatflüssen von Polymermembranen (Literaturwerte) unter ähnlichen Testbedingungen wettbewerbsfähig. Es wurde gezeigt, dass die geringe Energieeffizienz von keramischen Membranen weiterhin die größte Herausforderung für deren kommerzielle Nutzung in MD-Prozessen darstellt und diese der Fokus der Membranoptimierung darstellen sollte.

Keywords

Entsalzung, Direktkontaktmembrandestillation, Energieeffizienz, Flüssigkeitseindringdruck Hydrophobierung, Keramische Membranen, Kontaktwinkel, Membrandestillation, Membranemodifizierung Membranschichtaufbau, Membranstabilität, Modellierung, Permeanz, Permeatfluss, reale Lösungen, Salzrückhalt, Vakuummembrandestillation

Acknowledgements

This work was conducted at the Fraunhofer Institute for Ceramic Technologies and Systems (Fraunhofer IKTS) and was funded through a doctoral scholarship from the German Federal Environment Foundation (DBU).

I would like to express my uttermost gratitude towards my supervisors Prof. André Lerch and Prof. Ingolf Voigt. Not only did they give me the opportunity to carry out this project but guided me through the ‘muddy waters’ of this work while giving me the scientific freedom to truly call this work my own.

Furthermore, I would like to thank my colleagues at the Fraunhofer IKTS in Hermsdorf: Steffen Wöhner, Matthias Bernhardt, Christian Pflieger, Petra Puhlfürß, Gundula Fischer, Thomas Hoyer, Steve Wagner, Robert Sander and Marcus Weyd who helped me to extend my practical skillset as well as my theoretical knowledge by sharing their extensive experience in their specific field of expertise. Special thanks is owned to Marcus Weyd. He showed constant support for this project and acted as genuine mentor throughout the years becoming what I would now call a friend.

I would also like to express my gratitude towards my family, my friends and my life partner who provided support, love and joy in times of need and beyond.

CONTENT

LIST OF FIGURES ……IV

LIST OF TABLES……X

NOMENCLATURE……XI

1 INTRODUCTION 1

1.1 Motivation and Background 1

1.2 Main Objective, Approach and Outline of this Work 4

2 MD THEORY 7

2.1 Principle, Applications and Configurations 7

2.2 General Characteristics of Membranes used in Membrane Distillation Processes 12

2.2.1 Hydrophobicity 12

2.2.2 Morphological Properties 14

2.2.3 Thermal Conductivity and Membrane Stability 15

2.3 Polymeric Membranes in Membrane Distillation 16

2.4 Ceramic Membranes in Membrane Distillation 18

2.4.1 Surface Modification of Ceramic Membranes 22

2.5 Heat and Mass Transfer 24

2.5.1 Driving Force in Consideration of Temperature and Concentration Polarization 25

2.5.2 Mass Transfer and Mass Transfer Resistance 30

2.6 The Impact of Process Parameters 33

2.6.1 Feed Temperature, Experimental Set-Up and Cooling of the Permeate Side 34

2.6.2 Absolute Pressure on the Permeate Side 35

2.6.3 Feed Composition 35

2.6.4 Feed and Coolant Flow Velocity 36

3 MATERIAL AND METHODS 37

3.1 Membranes and Membrane Preparation 37

3.2 Characterization of Membrane Properties 39

3.2.1 Standard Characterization Methods 39
3.2.2 Steady State Gas Permeation 40
3.2.3 Thermal Conductivity 40
3.2.4 Contact Angle 42
3.2.5 Liquid Entry Pressure 43
3.3 Direct Contact Membrane Distillation and Vacuum Membrane Distillation Tests 45
3.3.1 Experimental Set-Up and Testing Procedure 45
3.3.2 Operational Parameters and Feed Composition 49
3.4 Membrane Treatment to Determine Membrane Stability and Overview of Membrane Types Investigated 50
3.5 Mass Transfer Modelling 54
4 RESULTS AND DISCUSSION 57
4.1 Characterization of Ceramic Membrane Properties 57
4.1.1 Thermal conductivity 58
4.1.2 Contact Angle Measurements 59
4.1.3 Liquid Entry Pressure – Impact of Pore Size, Feed Characteristics and Surface Modification 62
4.1.4 Steady State Gas Permeation – Impact of Coating Process and Layer Design 68
4.2 Impact of Membrane Characteristics on MD Performance and Stability 74
4.2.1 Impact of Membrane Properties in DCMD 74
4.2.2 Impact of Membrane Properties in VMD 76
4.2.3 The Effect of the Support Thickness in VMD and DCMD 78
4.2.4 Impact of layer structure and Modification in VMD 80
4.2.5 Stability of Asymmetric and Symmetric Ceramic Membranes 82
4.3 Impact of Process Parameters in VMD Using Ceramic Membranes to Treat Synthetic and Real Solutions 89
4.3.1 Impact of the Feed Temperature and Permeate Pressure in VMD 89
4.3.2 Impact of the Feed Flow Velocity in VMD 91
4.3.3 Impact of the Salt Concentration in VMD 95
4.3.4 Treatment of a Highly Saline Leachate Using Ceramic Membranes in VMD 98
4.3.5 Treatment of a RO Concentrate from the Dairy Industry Using Ceramic Membranes in VMD 100
4.4 Mass Transfer Modelling Through Asymmetric Ceramic Membranes 103

4.5 Performance Evaluation of Ceramic Membranes in MD Processes and an Approach to Membrane Optimization 108

5 SUMMARY AND CONCLUSION 111

5.1 Membrane Properties and Membrane Performance 111

5.2 Operational Parameters, Real Solutions and Mass Transfer Modelling 115

REFERENCES 118

List of Figures

Figure 1: Schematic representation of the structure of this work and the underlying research activities in reference to the respective chapter of this thesis and the specific research question that governed a particular part of this work 6

Figure 2: Schematic representation of the MD process (p_i: partial pressure of the respective species, e. g. water vapor) 7

Figure 3: Schematic representation of the four main MD configurations (DCMD, AGMD, VMD and SGMD) 9

Figure 4: Schematic representation of a contact angle describing a hydrophobic surface (a: $\theta > 90°$) and a contact angle defining a hydrophilic surface (b: $\theta < 90°$) 13

Figure 5: Schematic depiction of a plate and frame module in cross-flow mode (a) [30], the flow regime inside a spiral wound module (b) [108] and a hollow fiber module in cross flow mode (c) [30] ... 18

Figure 6: Cross-sectional SEM image of an asymmetrically structured tubular Al_2O_3 membrane with a final pore size of 400 nm [55] 19

Figure 7: Schematic representations of the cross-section of different ceramic (single and multichannel) tubes (a) [113], cross section of a multichannel membrane element (b) 20

Figure 8: Multichannel Tubes (Fraunhofer IKTS 2020) (a), Multichannel Tube Module (Fraunhofer IKTS 2020) (b), Hollow Fiber Module without Housing (Fraunhofer IKTS 2020) (c) 21

Figure 9: Material of ceramic membranes used in MD processes (a), ceramic membranes and membrane modules used in MD processes (b) and configuration studied using ceramic membranes (c), (adapted from [36]) 22

Figure 10: Schematic overview of the grafting process using two different molecules for the surface modification of tubular ceramic membranes 24

Figure 11: Temperature and Concentration Polarization Profile in DCMD cf,b: bulk stream solute concentration, $C_{f,m}$: interfacial solute concentration, $T_{f,b}$: Temperature of the bulk stream on the feed-side, $T_{p,b}$: Temperature of the bulk stream on the permeate-side) 25

Figure 12: Cross-sectional SEM image of a symmetric TiO_2 membrane with an average pore size of 200 nm and a wall thickness of 0.8 mm (Fraunhofer IKTS 2020) 38

Figure 13: Schematics of a thermal conductivity scan (modified after Popov et al. 1999), the solid line indicates the measured temperature rise (Θ) of the reference (black arrow) and unknown sample material (red arrows). The dashed line presents the calculated thermal conductivity of the samples ($ksample$) based on the equation 33 [55]..... 41

Figure 14: Illustration and components of the optical contact angle measuring and contour analysis systems (OCA 20)..... 42

Figure 15: Measuring of the static, advancing and the receding CA..... 43

Figure 16: P&I Diagram of the LEP test bed 44

Figure 17: Wetted tubular TiO_2 membrane..... 45

Figure 18: P&I Diagram of the DCMD test bed 47

Figure 19: P&I Diagram of the VMD test bed 48

Figure 20: Test Rig to cook modified single channel membranes (length: 250 mm) in either a saline alkaline, neutral or saline acidic solution for 96 hours 51

Figure 21: P&I Diagramm of the abrasion test bed 51

Figure 22: Schematic representation of the modelling approach 54

Figure 23: Thermal conductivity of different membranes made of Al_2O_3 (coated with Al_2O_3 layers), TiO_2 (coated with TiO_2), cordierite (Cor) and mixed oxide (MO), In case of Membrane Coating: final pore size = 100 nm, HOC refers to the hydrophobic agent as defined in chapter 3.1, 5 tests, the error bars depict the confidence intervals of the average value 58

Figure 24: Contact angle measurements of Al_2O_3 flat sheet membranes (final pore size: 200 nm) modified with 11 different hydrophobic agents (HA: Hydrophobic Agent (1 wt.%), HOC/HOG: internal standard, testing solution: pure water at room temperature, minimum of 4 tests, the error bars depict the confidence intervals of the respective average value 60

Figure 25: Contact angle hysteresis of Al_2O_3 flat sheet membranes modified with 7 different hydrophobic agents (light grey bars: advancing CA, dark grey bars: receding CA and hysteresis CAH, testing solution: pure water at room temperature, minimum of 4 tests, the error bars depict the confidence intervals of the respective average value 61

Figure 26: LEP in dependence of the material (light grey: Al_2O_3, dark gray: TiO_2), layer structure (symmetric and asymmetric), pore size (asymmetric membranes: final membrane layer, symmetric membranes: support) and the type and concentration of the hydrophobic agent (HOC and HOM), minimum of 4 tests, the error bars depict the confidence intervals of the respective average value 63

Figure 27: LEP in dependence of the pore size and testing solution temperature, the maximum LEP that could be measured was 7 bar (membrane: TiO_2 modified with 1 wt.% HOC, testing solution: pure water, 3 to 6 tests were conducted on separate membranes for each temperature), the error bars depict the confidence intervals of the respective average value 64

Figure 28: LEP in dependence of the pore size and NaCl concentration of the testing solution, the maximum LEP that could be measured was 7 bar (membrane: TiO_2 modified with 1 wt.% HOC, testing solution: 1 g NaCl /kg H_2O to 300 g NaCl /kg H_2O at 20 °C, minimum of 3 tests, the error bars depict the confidence intervals of the respective average value 66

Figure 29: LEP in dependence of the pore size and sucrose as and ethanol concentration of the testing solution, the maximum LEP that could be measured was 7 bar (membrane: TiO_2 modified with 1 wt.% HOC, testing solutions: 20 wt.% ethanol and 20 wt.% sucrose at 20 °C, minimum of 3 tests, the error bars depict the confidence intervals of the respective average value 67

Figure 30: N_2 permeance in dependency of the membrane material, pore size, thickness and layer structure (light grey bars: Al_2O_3 and dark grey bars: TiO_2), exact layer structure is given in Table 5, minimum of 3 tests, the error bars depict the confidence intervals of the respective average value 69

Figure 31: N_2 permeance as a function of pore size of an incrementally coated TiO_2, Al_2O_3, cordierite and mixed oxide supports (white shapes) to the pore size of 100 nm, the black markers symbolize the modification of 100 nm TiO_2 and Al_2O_3 membrane systems modified with 1 wt.% HOC molecules, test conditions: T: ambient temperature, $p_{permeate}$: ambient pressure, $_{\Delta}p_{,Feed\text{-}Permeate}$: 1000 mbar, minimum of 3 tests, the error bars depict the confidence intervals of the respective average value 71

Figure 32: N_2 permeance as a function (x axis: logarithmic) of incrementally coated mixed oxides supports (pore size: 1.0 µm) towards a pore size of an active membrane layer of 100 nm (TiO_2, Al_2O_3) or 110 nm (ZrO_2, test conditions: T: ambient temperature, $p_{permeate}$: ambient pressure, $p_{\Delta,Feed\text{-}Permeate}$: 1000 mbar, minimum of 3 tests, the error bars depict the confidence intervals of the respective average value 73

Figure 33: Permeate flux for different membranes (MO = mixed oxide support) in DCMD configuration, test conditions: Feed: 30 g NaCl/ kg H_2O, T_{Feed}: 60 °C, $T_{Coolant}$: 20 °C, v = 0.7 m/s, a minimum of 4 tests, the error bars depict the confidence intervals of the respective average value..... 75

Figure 34: Permeate fluxes (bars) for different membranes (MO = mixed oxide support) in VMD configuration and the corresponding salt rejection (dots), test conditions: Feed: 30 g NaCl/kg H_2O, T_{Feed}: 60 °C, $T_{Coolant}$: 3 °C, v = 0.7 m/s, p_{abs}: (VMD): 100 mbar, minimum of 3 test, the error bars depict the confidence intervals of the respective average value..... 77

Figure 35: Permeate flux (columns) and salt rejection (dots, only VMD) for TiO_2 (100 nm and 400 nm) and Al_2O_3 (100 nm) membranes with a support wall thickness of 1.5 mm and 1.0 mm in DCMD (dark grey bars) and VMD (light grey bars) configuration, DCMD test conditions: Feed: 30 g NaCl/ kg H_2O, T_{Feed}: 60 °C, $T_{Coolant}$: 20 °C, v = 0.7 m/s, VMD test conditions: Feed: 30 g NaCl/ kg H_2O, T_{Feed}: 60 °C, $T_{Coolant\ (VMD)}$: 3 °C, v = 0.7 m/s, $p_{abs\ (VMD)}$: 100 mbar, minimum of 3 tests, the error bars depict the confidence intervals of the respective average value..... 79

Figure 36: Permeate flux (bars) and salt rejection (dots) for Al_2O_3 (light gray bars) and TiO_2 (dark gray bars) membranes in dependence to the layer design, pore size, thickness (1.0 ,mm and 1.5 mm) and surface modification (2 wt.% HOC and 2 wt.% HOM) in VMD, test conditions: Feed: 30 g NaCl/ kg H_2O, T_{Feed}: 60 °C, $T_{Coolant\ (VMD)}$: 3 °C, v = 0.7 m/s, $p_{abs\ (VMD)}$: 100 mbar, minimum of 3 tests, the error bars depict the confidence intervals of the respective average value..... 81

Figure 37: LEP in regard to membrane material and pore size before and after stress tests with an alkaline (50 g Na_2CO_3 + 50 g NaCl per kg H_2O), neutral (pure water) and acidic solution (135 g HCl (37 wt.%) + 50 g NaCl per kg H_2O) for 96 hours at around 100 °C, modification: 1 wt% HOC, 2 tests per membrane type (exception: 400 nm TiO_2: one test), the results depicted above are based on individual tests (2x per solutions and membrane type)..... 82

Figure 38: LEP in regard to membrane material and pore size before and after stress tests with an alkaline (50 g Na_2CO_3 + 50 g NaCl per kg H_2O), neutral (pure water) and acidic solution (135 g HCl (37 wt.%) + 50 g NaCl per kg H_2O) for 96 hours at around 100 °C, modification: 1 wt.% HOG, 2 tests per membrane type,), the results depicted above are based on individual tests (2x per solutions and membrane type)..... 83

Figure 39: LEP in regard to membrane material (Al_2O_3: light gray bars and TiO_2: dark gray bars), layer design, pore size, thickness (1.0 mm and 1.5 mm) and surface modification (2 wt.% HOC and 2 wt.% HOM) before and after stress tests using an alkaline and saline solution (96 hours,

100 °C, 250 g NaCl + 50 g Na_2CO_3 per kg H_2O), minimum of 3 tests, the error bars depict the confidence intervals of the respective average value 85

Figure 40: LEP in regard to membrane material (Al_2O_3: light gray bars and TiO_2: dark gray bars), layer design, pore size, thickness (1.0 mm and 1.5 mm) and surface modification (2 wt.% HOC and 2 wt.% HOM) before and after stress tests using a hot saline solution (96 hours, 100 °C, 250 g NaCl per kg H_2O), minimum of 3 tests, the error bars depict the confidence intervals of the respective average value 86

Figure 41: LEP in regard to membrane material (Al_2O_3: light gray bars and TiO_2: dark gray bars), layer design, pore size, thickness (1.0 mm and 1.5 mm) and surface modification (2 wt.% HOC and 2 wt.% HOM) before and after stress tests using an acidic and saline solution (96 hours, 100 °C, 250 g NaCl + 1 kg HCl (5 wt.%) minimum of 3 tests, the error bars depict the confidence intervals of the respective average value 87

Figure 42: LEP of symmetric and asymmetric Al_2O_3 and TiO_2 membranes modified with 2 % HOC in regard to pore size before and after a abrasion test for 7 hours and 56 hours (discontinuously: 7 days x 8 h), test conditions: Feed: 38.48 g $MgSO_4$ + 284.50 $MgCl_2$ + 69.98 g NaCl + 54.13 g KCl per kg H_2O, T_{Feed}: ambient temperature, p: ambient pressure, v = 0.73 m/s (the LEP of the same membrane determined before and after the abrasion tests, minimum of 3 tests, the error bars depict the confidence intervals of the respective average value 88

Figure 43: Permeate flux (bars) and rejection (dots) of Al_2O_3 and TiO_2 membranes (final pore size: 100 nm) in dependency of the feed temperature and permeate pressure, test conditions: Feed: 350 g NaCl/kg H_2O, $T_{Coolant}$: 0 °C, v = 1.08 m/s; minimum of 3 tests, the error bars depict the confidence intervals of the respective average value 90

Figure 44: Permeate flux (bars) and rejection (dots) of an Al_2O_3 membrane (final pore size: 100 nm) in dependency of the flow velocity, feed temperature and NaCl concentration, test conditions: p_{abs}: 100 mbar, $T_{Coolant}$: 0 °C; minimum of 3 tests, the error bars depict the confidence intervals of the respective average value 92

Figure 45: Permeate flux (bars) and rejection (dots) of an TiO_2 membrane (final pore size: 100 nm) in dependency of the flow velocity and feed temperature test conditions: Feed: 350 g NaCl per kg H_2O, p_{abs}: 100 mbar, $T_{Coolant}$: 0 °C; minimum of 3 tests, the error bars depict the confidence intervals of the respective average value 93

Figure 46: Energy (thermal) efficiency (unity is the maximum value possible) of Al_2O_3 and TiO_2 membranes (final pore size: 100 nm) in dependency of the flow velocity and feed temperature,

test conditions: Feed: 350 g NaCl/kg H_2O, $T_{Coolant}$: 0 °C, p_{abs}: 100 mbar; minimum of 3 tests, the error bars depict the confidence intervals of the respective average value 94

Figure 47: Permeate flux (bars) of TiO_2 membranes in dependency of the membrane pore size (final pore size: 100 nm, 250 nm and 400 nm) and feed concentration; test conditions: $T_{Feed:}$ 60 °C, p_{abs}: 100 mbar, $T_{Coolant}$: 0 °C; v = 0.72 m/s, minimum of 4 tests, the error bars depict the confidence intervals of the respective average value 96

Figure 48: Permeate flux (blue dots) and energy efficiency (yellow) of an Al_2O_3 membrane (final pore size: 100 nm) in dependency to the salt concentration (initial: 200 g NaCl per kg H_2O, end: saturation point: ~375 g NaCl per kg H_2O at the given feed temperature); p_{abs}: 100 mbar, $T_{Coolant}$: 2 °C; v = 0.72 m/s, $T_{Feed:}$ 70 °C, continuous testing over 24 hours (cumulative testing time) 97

Figure 49: Permeate flux (light grey bars) and energy efficiency (dark grey bars) of an Al_2O_3 membrane (final pore size: 100 nm) in dependency of the flow velocity and permeate pressure; test conditions: Feed: 38.48 g $MgSO_4$ + 284.50 g $MgCl_2$ + 69.98 g NaCl + 54.13 g KCl per kg H_2O, $T_{Feed:}$ 75 °C, $T_{Coolant}$: 15 °C; minimum of 3 tests, the error bars depict the confidence intervals of the respective average value, fresh water extracted was poured back into the feed container after each test 99

Figure 50: Permeate flux (diamond shapes) and salt rejection (circles) in respect to the testing time (cumulative testing period, permeate was poured back into the feed container) test conditions: Feed: ~35 g salts (NaCl, K, Mg_2 and P) + ~10 g humic substances per kg H_2O, $T_{Feed:}$ 60 °C, p_{abs}: 100 mbar, $T_{Coolant}$: 0 °C; v = 0.72 m/s, the permeate was poured back into the feed container 101

Figure 51: Simulated (dotted lines) and measured (squares) fluxes of different asymmetric TiO_2 membranes in respect to the feed temperature under variation of the flow velocity, test conditions: p_{abs}: 100 mbar, $T_{Coolant}$: 0 °C; minimum of 3 tests, the error bars depict the confidence intervals of the respective average value 104

Figure 52: Simulated (dotted lines) and measured (squares) fluxes of different asymmetric TiO_2 membranes in respect to the feed temperature under variation of the flow velocity in consideration of a correction factor (Eq. 40), test conditions: p_{abs}: 100 mbar, $T_{Coolant}$: 0 °C; minimum of 3 tests, the error bars depict the confidence intervals of the respective average value of the experimentally determined permeate flux 106

List of Tables

Table 1: Overview of standard membrane characterization methods for quality control 40

Table 2: Standard operational parameters for DCMD and VMD tests 49

Table 3: Process parameters investigated in VMD 49

Table 4: Composition of solutions that were used to test the stability of tubular ceramic membranes 50

Table 5: Specifications of tubular membrane systems that were studied within the scope of this work (δ is the support wall thickness, ε is the open porosity of the support, d_p is the average pore size, molecule label is the internal reference to a specific surface modification agent and ω is the mass concentration of the applied modification agent 52

Table 6: Mathematical correlations and fit function used to determine the viscosity of the feed ($\eta Feed$), heat capacity of the feed (CP), thermal conductivity of the feed (kf) and the permeate flux (J) for the VMD mass transfer modelling (if unspecified the concentration refers to the total mass of the mixture) 56

Table 7: LEP values of commercially available hydrophobic polymeric membranes given by the manufactures [83] 65

Table 8: Tortuosity values derived using the DGM for the specific TiO_2 layers obtained using N_2 permeance data as well as data on the thickness, porosity and pore size of the membrane layer 103

Nomenclature

AD	Adsorption desalination
AGMD	Air gap membrane distillation
CA	Contact angle
CAH	Contact angel hysteresis
CNT	Carbon nano tubes
Cor	Cordierite
CDI	Capacitive deionization
CVD	Chemical vapor deposition
DCMD	Direct contact membrane distillation
DGM	Dusty gas model
ED/EDR	Electrodialysis and electrodialysis reversal
FAS	Fluoroalkylsilanes
FO	Forward osmosis
GOR	Gained output ratio
LEP	Liquid entry pressure
LGMD	Liquid gap membrane distillation
MCDI	Membrane capacitive deionisation
MED	Multi-effect distillation
MEMD	Multi-effect membrane distillation
MENA	Middle East and North Africa
MGMD	Material Gap Membrane Distillation
MO	Mixed oxide
MD	Membrane distillation
MSF	Multi-stage flash distillation
NF	Nano filtration

PDMS	Polydimethylsiloxane	
PFAS	Perfluoroalkylsilanes	
PGMD	Permeate gap membrane distillation	
P&I	Piping and instrumentation	
PP	Polypropylene	
PTFE	Polytetrafluoroethylene	
PVC	Polyvinyl chloride	
PVDF	Polyvinylidene fluoride	
RO	Reverse osmosis	
SEM	Scanning electron microscope	
SGMD	Sweep gas membrane distillation	
TDS	Total dissolved solids	
TSGMD	Thermostatic sweeping gas membrane distillation	
UF	Ultra filtration	
V-MEMD	Vacuum Multi-Effect Membrane Distillation	
VMD	Vacuum membrane distillation	
VOCs	Volatile Organic Compounds	
ZLD	Zero liquid discharge	
B	Mass transfer coefficient	[kg/(m² s Pa]
B_g	Geometric factor	[-]
C_P	Heat Capacity	[kJ/(kg K)]
c	Concentration	[mol/L], [mol/kg], [g/L], [g/kg]
D	Diffusion Coefficient	[m²/s]
d_p	Pore diameter	[m]
EE	Energy efficiency	[-]
ΔH	Enthalpy	[J/kg]

h	Heat transfer coefficient	[J/(m² s K)]
J	Permeate flux	[mol/m² s], [kg/(m² h)]
Kn	Knudsen number	[-]
k	Thermal conductivity	[W/(m K)
k_B	Boltzmann constant	[m² kg/(s² K)]
L	Membrane channel length	[m]
M_i	Molar weight of the species i	[kg/mol]
Nu	Nusselt number	[-]
p	Pressure or partial pressure	[Pa]
p_i	Partial pressure of species i	[Pa]
p_0	Partial pressure of pure water	[Pa]
Pr	Prandle number	[-]
Q	heat flux	[W]
r	Pore radius	[m]
R	Universal gas constant	[J/(mol K)]
Re	Reynolds number	[-]
Sc	Schmidt number	[-]
Sh	Sherwood number	[-]
a_w	Water activity	[-]
γ	Interfacial tension	[N/m]
δ	Thickness	[m]
ε	Open porosity	[-]
ρ	Density	[kg/m³]
θ	Temperature	[K], [C]
σ	Collusion diameter	[m]
σ_g	Geometric standard deviation factor	[-]

v	Flow velocity	[m/s]
$\bar{v}$	Molecular velocity	[m/s]
λ	Free mean path	[-]
τ	Tortuosity	[-]
η	Dynamic viscosity	[Pa s]

Subscripts

av	Average
b	Bulk
c	Conduction
f	Feed or feed side
G	Gas
h	Hydraulic
L	Liquid
m	Membrane
max	Maximum
p	Permeate or permeate side
S	Solid
ref	Reference
t	Total
w	Water
th	Thermal
v	Vapor

Superscripts

K	Knudsen diffusion
D	Diffusion
M	Molecular diffusion or ordinary diffusion
V	Viscous Flow or Poiseuille flow

1 Introduction

1.1 Motivation and Background

Resources that are easily accessible by humankind are limited. This applies not only to precious metals and rare earth elements that secure our lifestyle and technological advancement but also to fertile soil and fresh water that are a fundamental requirement for human life. Access to clean water secures the food supply, hygienic standards and industrial growths [1] and is a prerequisite for human health and wellbeing. Although the United Nations General Assembly recognized the access to clean water and sanitation as a human right (Resolution 64/292) [2] and the 2030 Agenda for Sustainable Development (including the goal 6: Clean water and sanitation') was ratified by all United Nations Member States in 2015 around 71 % of the population experiences moderate to severe water scarcity while 66 % (four billion people) face severe physical water scarcity at least one month per year [3]. A growing population (projected to reach 9.7 billion by 2050 [4]) increased urbanization, accelerated consumption and economic activity as well as the deteriorating climate crises (changing precipitation patterns, increasing global temperatures, frequent extreme weather events [5]) and ongoing environmental pollution [6–8] will limit the access to clean water in many regions of the world even more. The water demand is projected to increase by one-third until 2050 [8] while half of the world's population is forecasted to live in water-stressed regions [9]. Conventional fresh water sources such as groundwater, lakes, and rivers (replenished by rain and snowfall) are no longer sufficient to cover the water demand in many regions. Consequently, humanity needs to increase its efforts to provide sufficient freshwater quantities to current and future generations through unconventional instruments. This means that in addition to the reduction of the amount of water that is wasted or lost through carelessness, luxurious lifestyles and aging infrastructure, non-traditional impaired freshwater sources including saline sea, brackish and river water as well as industrial, agricultural and municipal waste waters (e.g. produced water and mining waste water) must be utilized [10].

Due to the overexploitation of traditional fresh water sources (e.g. groundwater) and the improved technical maturity of conventional desalination processes, desalination processes are increasingly acknowledged as a viable option to obtain fresh water from saline water sources and already contribute significantly towards meeting the current domestic and municipal water demand in many regions [6]. In February 2020 the global fresh water production capacity via desalination processes amounted to 114.9 million m^3 per day facilitated by 16,876 desalinations plants [11] with the Middle East and North Africa (MENA) having about 50 % of the desalination capacity [6]. The capacity has been growing by around 7 % on a yearly basis from 2010 and is expected to

grow at the same rate for the MENA countries in the future whereas other regions (e. g. Asia and North America) will experience an even stronger growth. For instance, China was expected to boost its desalination capacity from about 1 million m³ per day in 2013 to over 3 million m³ per day by 2020 [12]. Even though technical mature desalination technologies bring vital relief to regions that are vulnerable to water shortages by providing reliable water supply irrespective of the local freshwater availability they have technical limitations, high economic costs and considerable ecological footprints [6,13]. Conventional desalination processes are grouped into membrane-based and thermal desalination processes. The most popular membrane-based process is Reverse Osmosis (RO) whereas multi-stage-flash (MSF) and multi-effect distillation (MED) are widespread thermal desalination processes. RO progressed significantly in the last decade in terms of energy consumption, permeate flux and capacity flexibility and became the most energy efficient (seawater as feed: 2 - 7 kWh_e/m^3 permeate [14]) and cost effective conventional desalination process [11,15,16] accounting for 69 % of the global desalination capacity in 2019 [6]. MED and MSF make up around 18 % and 7 % of the global desalination capacity respectively [6]. MED and MSF are limited through corrosion processes that inhibit feed salinities above 6 - 7 wt.% [10,17], are not easily scalable, have higher space requirements and higher energy consumptions (MED: 1.5 - 2.5 kWh_e/m^3 + 5 - 8.5 kWh_{th}/m^3 and MSF: 3.4 - 4.5 kWh_e/m^3 + 5.6 - 8.0 kWh_{th}/m^3 [12,14]) than RO processes (2 - 7 kWh_e/m^3 permeate) and are not as cost effective [6,18,19]. Although RO processes are competitive with thermal desalination processes in terms of energy consumption, costs, and flexibility they also exhibit limitations. RO processes are limited by the osmotic pressure (the treatment of feeds with TDS concentrations > 70 g/L is not viable [20]), decline in performance due to scaling and fouling processes and require a sufficient pretreatment of the feed [21,22]. Another important issue is the negative effect conventional desalinations processes have on the environment. For instance, 141 million m³ of brines were produced per day (as of 2019) which are typically discharged untreated into the marine ecosystem [6]. Brines (the term brine is usually used for saline streams with concentrations of total dissolved salts (TDS) > 55,000 mg/L [20]) generated as a byproduct of desalination is not only of higher salinity and temperature relative to ambient seawater but can be loaded with pretreatment chemicals organic substances and heavy metals [20,23] and are often discharged into open water bodies where they can do tremendous damage to the environment and local marine ecosystem [24].

Despite the fact, that conventional desalination technologies have proven reliable and achieved technical maturity the above-mentioned limitations (e.g. energy consumption, osmotic pressure, pretreatment requirements) and stricter environmental regulations and guidelines are strong drivers for the optimization and commercialization of emerging desalination technologies such as

membrane distillation (MD), electrodialysis and electrodialysis reversal (ED/EDR), capacitive deionization (CDI), membrane capacitive deionization (MCDI), adsorption desalination (AD), humidification-dehumidification, microbial desalination and forward osmosis (FO) [25,26]. Jones et al. 2019 [6] pointed out that second to RO processes emerging technologies are being investigated the most among all desalination technologies by the scientific community in recent years. This trend clearly indicates the strong demand in alternative technologies addressing the challenges related to desalination and will further increase their recovery ratios (possibly enabling zero liquid discharge (ZLD)), lower their energy demand and costs, increase their flexibility and reduce their environmental footprints in respect to conventional desalination processes.

Due to the fact that MD processes combine the benefits of thermally driven processes (relatively low sensitivity to the feed composition) with the flexibility of membrane-based processes, research interest in MD has grown considerably in the last decades with almost 200 peer-reviewed MD articles published in 2018 [27]. MD processes can operate with temperatures below the boiling point and therefore supports the utilization of low-grade energy sources (e. g. waste heat, solar power and geothermal heat) [28]. Scaling of membrane distillation processes is generally convenient as membrane processes are modularly designed, allowing the adaption of the membrane/evaporation surface by adding or reducing the number of membrane modules. Through the utilization of membranes as contactors in MD processes, the evaporation surface can be adjusted easier than with vacuum distillation processes (= thermal distillation). Thereby MD offers an energy-attractive approach for the (off-grid) treatment of high concentrated solutions (concentrations that are too high for RO processes), potentially enabling ZLD targets [17,29]. Due to the lack of viable heat recovery and multi-stage concepts in pilot scale (no cost competitiveness) as well as the absence of MD-customized membranes MD processes are not fully commercialized yet [30].

Polymeric membranes are most commonly utilized in MD processes due to their low cost, intrinsically hydrophobic surfaces, and good mass transfer characteristics [28,31] but are not robust enough when applied to aggressive feed solutions (e. g. highly concentrated brines with abrasive characteristics, extreme pH, solvent and oxidant laden solutions) which can lead to their permanent degeneration [32–36]. A robust alternative membrane platform for more extreme feed solutions are ceramic membranes which offer superb thermal, chemical and mechanical stability compared to polymeric membranes [37,38]. Ceramic membranes have only been investigated in about 20 % of all MD related publications [36] which is due to their comparatively high manufacturing costs and intrinsic hydrophilic surfaces. Ramelow et al. 2019 [36] give an extensive overview of MD studies (lab-scale) utilizing ceramic membranes with varying characteristics and reported superb salt rejections and competitive permeate fluxes for ceramic membranes in

comparison with polymeric counterparts. Therefore, customized robust ceramic membranes utilized in MD processes could be a viable alternative for treatment of aggressive solutions that are too extreme for polymeric membranes. This assessment establishes the motivation for the research activities and results that are presented within this doctoral thesis that aims to lay the foundation to broaden the applications of ceramic membranes in MD processes.

1.2 Main Objective, Approach and Outline of this Work

The main objective of this work was to evaluate the strengths and limitations of ceramic membranes utilized in MD processes for the treatment of saline solutions. Furthermore, this work aimed to use the obtained information to give stimuli for membrane adaptation and optimization supporting the commercialization of ceramic membranes in MD processes while identifying and extending the most promising areas of application. In order to design and plan the research activities within this work (in respect to the mentioned above objectives) several scientific questions were defined:

1. Does the modification of hydrophilic ceramic membranes using hydrophobic agents enable their utilization in MD?
2. How do specific membrane and solution characteristics affect the extent and stability of the hydrophobic surface properties?
3. How do specific membrane characteristics affect the membrane performance in MD?
4. Is a specific MD configuration more suitable for the use of ceramic membranes in MD?
5. How do process parameters affect the performance of ceramic membranes in MD?
6. Are modified ceramic membranes used in MD processes suitable to treat aggressive media?
7. Can accepted MD mass transfer models facilitate the simulation of the mass transport through asymmetric (multi-layer) ceramic membranes and are adaptations required?
8. Is the mass transfer of ceramic membranes competitive to the mass transfer of polymeric membranes in MD?

By considering these questions specific research activities could be designed and planned that lay the foundation of the structure of the work and enabled a strategic approach to achieve the main objectives stated above.

The structure of this work (research activities and their interconnections) is presented schematically in Figure 1 along with a reference to the respective chapter of this thesis and the

specific research question that governed a particular part of this work. The following paragraph will give an overview of the research activities conducted.

Fluorinated and non-fluorinated hydrophobic agents were used to modify ceramic flat sheet membranes and a selection of single channel membranes (chapter 3.1, Table 5) with different characteristics (e.g. material, pore size).

These membranes and non-modified counterparts were characterized in respect to relevant membrane properties (e.g. pore size, thermal conductivity, hydrophobic characteristics) using standard characterization methods (e.g. mercury porosimetry) as well as other investigative methods such as thermal conductivity scanning, steady state gas permeance tests, contact angle measurements and liquid entry pressure tests, chapter 4.1). For instance, liquid entry pressure tests were used to investigate the impact of the membrane pore size as well as testing solution characteristics (temperature and composition) on the hydrophobic properties of a variety of modified ceramic single channel membranes (chapter 4.1.3).

Direct contact membrane distillation (DCMD) and vacuum membrane distillation (VMD) tests were conducted on different fully characterized modified ceramic single channel membranes using a fixed set of process parameters (chapter 4.2). This was done to gain insight into the interaction between specific membrane properties (e.g. layer design, pore size, membrane thickness and thermal conductivity) and membrane performance (permeate flux and rejection/permeate quality) in respect to these MD configurations.

The stability of a variety of ceramic membranes with different surface modifications and layer designs against hot saline solutions characterized by extreme pH values was investigated using LEP tests (chapter 4.2.5).

The effect of relevant process parameters (e.g. feed temperature, flow velocity and permeate pressure) on the performance of Al_2O_3 and TiO_2 single channel membranes was investigated using synthetic and real feed solutions (chapter 4.3).

Furthermore, mass transfer calculations based on the Dusty-Gas-Model and semi-empirical relationships suggested by the literature were conducted in consideration of crucial membrane characterization data while addressing model deficiencies (chapter 4.4). This was done to establish a mass transfer modelling fundament for ceramic membranes in MD that can be extended in future works and possibly serve as a valuable tool for membrane optimization in the future.

Finally, the performance data of the investigated ceramic membranes is discussed and compared with data on polymeric membranes presented in the literature. The strength and limitations of modified ceramic membranes with focus on real MD applications was highlighted and a path for membrane optimization with focus on the energy efficiency (great impact on cost-efficiency) was

proposed (chapter 4.5).

The in-depth and up-to-date understanding of MD processes (e. g. strength and limitations, applications, configurations and heat and mass transfer) and of the membranes utilized in MD processes (e. g. membrane properties, ceramic membrane manufacturing and modification) given in the theory section (chapter 2) governs the discussion and puts the presented data in perspective. For instance, MD mass transfer simulation data presented in the result section will be based on accepted models and underlying assumptions introduced in the heat and mass transfer chapter of the theory section (chapter 2.5).

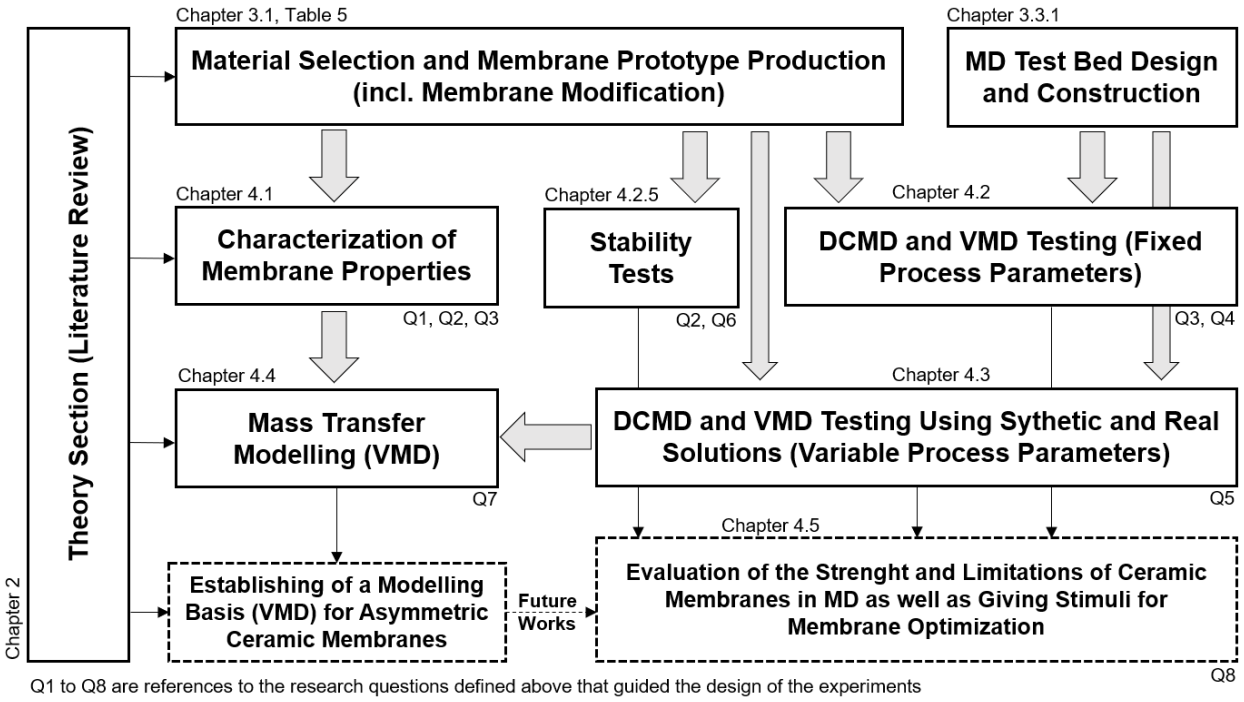

Figure 1: Schematic representation of the structure of this work and the underlying research activities in reference to the respective chapter of this thesis and the specific research question that governed a particular part of this work

2 MD Theory

2.1 Principle, Applications and Configurations

MD is not a novel process. The first patent related to the MD process was filed in 1963 whereas the first scientific paper was published in 1967. But only in 1986, the term 'Membrane Distillation' was chosen by a scientific committee at a workshop in Rome to distinguish the MD process from conventional thermal separation processes [39]. This was necessary since the MD process is – just like all thermal processes – temperature dependent and relies on a phase change based on the vapor-liquid equilibrium [27]. With the term MD, the emphasis was put on the membrane that is imperative to the distillation process.

Since then, the term MD refers to a thermally induced separation process that utilizes a hydrophobic porous membrane as a barrier between a warm feed and a cooler permeate side. The driving force is a partial pressure gradient across the membrane caused by a temperature difference between the interfaces of the membrane. The partial pressure gradient leads to the evaporation of a liquid (e.g. water) and the subsequent transport of its gas phase through the membrane to the permeate side where its condensation takes place (Figure 2) [27,34,40].

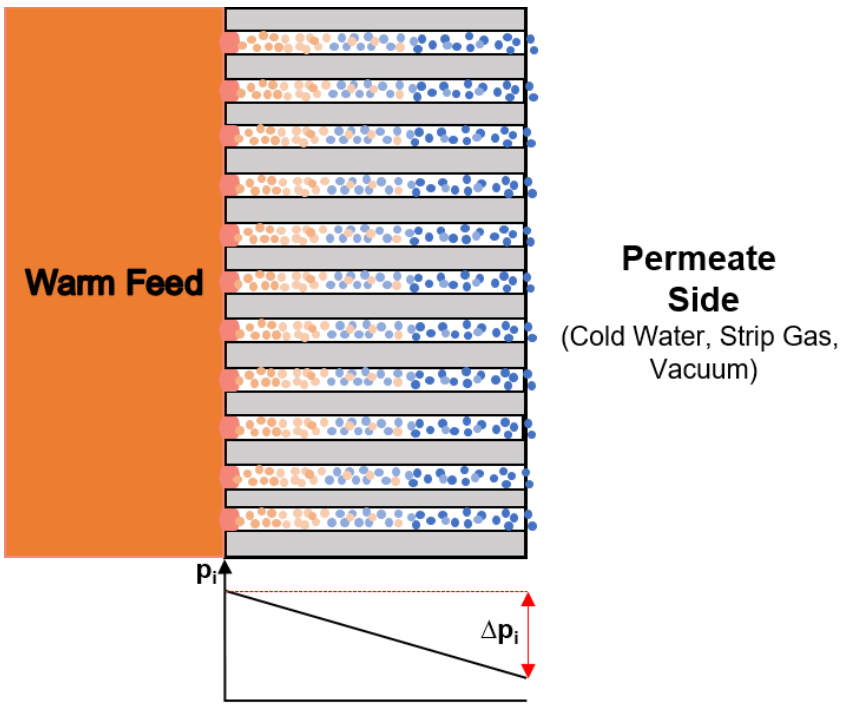

Figure 2: Schematic representation of the MD process (p_i: partial pressure of the respective species, e. g. water vapor)

The most attractive feature of the MD process is that evaporation already occurs below the boiling point and low-grade energy sources such as solar and geothermal energy and waste heat can be applied to generate the driving force. In addition, the MD process hybridizes the benefits of thermal and membrane-based processes and is less sensitive to the salinity levels of the feed than conventional desalination technologies. Additionally, MD processes enable the theoretical rejection of 100 % of non-volatile compounds (e.g. salts, inorganic compounds, and macromolecules), allow low operating pressures and have little space requirements in comparison to conventional thermal desalination processes. Furthermore, MD processes have a good scalability due to their modular design, are easy to couple with other processes and are less prone to fouling than pressure driven membrane processes [41–46].

In the past, these characteristics led to the belief that MD processes could advance beyond the limitations of conventional seawater desalination technologies such as RO, MED and MSF and pose an attractive alternative to them. If the number of studies focused on MD published between 2011 and 2016 is taken as an indicator, sea water desalination is still the most popular potential commercial MD application [31]. However, since conventional desalination technologies have been on the market at an industrial scale for decades and have proven reliable and very few scientific studies demonstrated that MD processes have achieved competitive energy-efficiency, MD processes will not widely replace conventional sea water desalination technologies in the near future [17,47,48]. Thomas et al. 2017 [31] offered an explanation on why MD research is still mainly focused on sea water desalination applications despite the lack of data that supports the competitiveness of MD processes in this area. It is argued that there is a tendency to shape research articles in a way that makes them more attractive for reputed journals and that desalination applications simply offer cheap and easily available feed solutions. For instance, it is easier to make a 3.5 wt.% NaCl feed solution than to obtain a specific solution originating from the food or chemical sector. In addition, the use of the 3.5 wt.% NaCl feed solution makes the data to be published more consistent with topics promoted by the Journal ‘Desalination’ which has a relatively high impact factor. This possibly makes sea water desalination the dominant MD research topic even though MD has yet to prove its competitiveness with conventional sea water desalination processes and other MD applications being significantly more attractive [31].

After the desalination of sea water, waste water treatment (e.g. waste waters from the textile and mining industry and olive mills and produced waters) is the most popular MD research topic followed by brine concentration which is expected to further gain popularity [31]. The MD process allows the further concentration of brines, increased water recovery, limiting brine volumes and even enabling Zero-Liquid-Discharge and resource recovery (e.g. salts) if coupled with a crystallizer unit [49]. The interest in MD brine treatment is growing due to the increasing number

of desalination plants globally which lead to a surge in brine production and subsequently to the intensification of related environmental risks and challenges demanding technical solutions to address those [19,31]. The interest in MD processes applied in the food processing sector (e.g. concentration of fruit juices and flavor/aromatic compounds and removal of volatile compounds such as ethanol [27,31]) and chemical industry (e.g. concentration of butanol, glycerol and isopropanol, removal of ammonia and VOCs and the recovery of acids) for MD applications has been declining significantly over the last years. Other MD research topics such as the removal of arsenic, boron, fluoride, herbicides and the concentration of ginseng extract, medicinal herbal products or lignocellulosic hydrolysates have been investigated in a modest number of publications [31].

Several MD configurations have been developed and studied over the years that mainly differ from each other regarding how the driving force is generated and the way the permeating vapor is being condensed [50]. The four basic MD configurations are referred to as direct contact membrane distillation (DCMD), air gap membrane distillation (AGMD), vacuum membrane distillation (VMD) and sweep gas membrane distillation (SGMD) and are depicted in Figure 3.

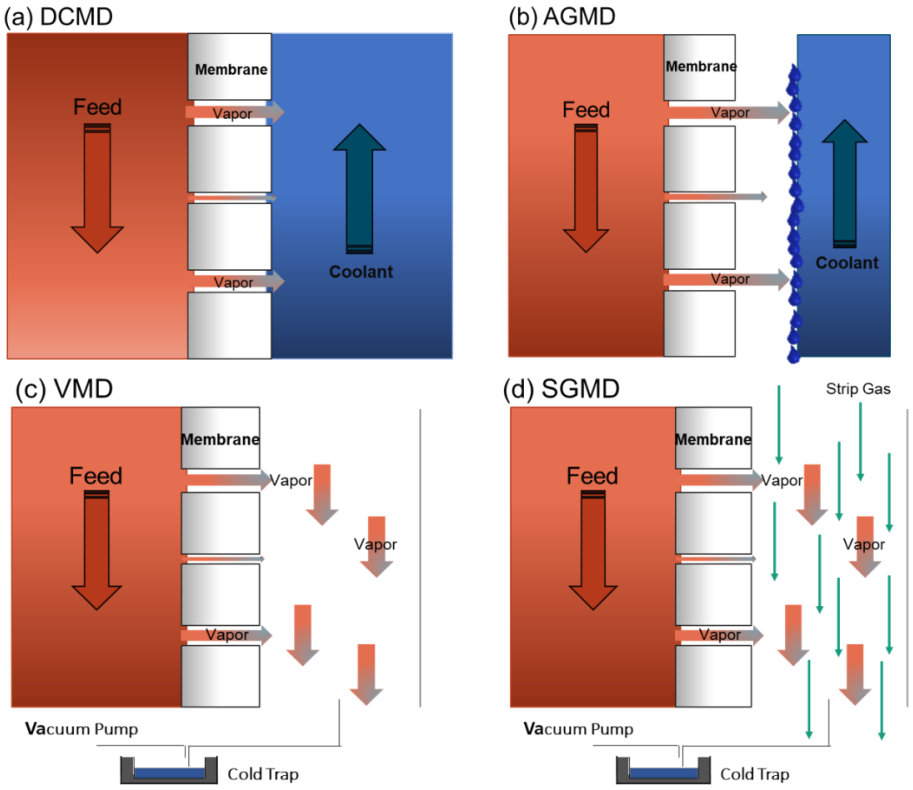

Figure 3: Schematic representation of the four main MD configurations (DCMD, AGMD, VMD and SGMD)

All the configurations have in common that one side of the membrane is in direct contact with the feed solution [51]. In DCMD both sides of the membrane are in direct contact with a liquid. The permeate side of the membrane module is fed with a cooling liquid (usually demineralized water) that causes the permeating vapor to condensate on the permeate side inside the membrane module (Figure 3a) [52]. DCMD is considered to be the most simple MD set-up and thus frequently chosen as the MD configuration used in MD related studies in counter-current flow mode (35 % of all MD studies in 2018 were conducted using DCMD) [17,30,53]. As the membrane is in direct contact with the hot feed and coolant this MD configuration is characterized by the highest conductive heat loss and strongest temperature polarization effects among the four main configurations [28,54] which can greatly reduce the thermal efficiency of the MD process. Another disadvantage of DCMD is the increased risk of wetting on the permeate side of the membrane which subsequently can further affect the mass transport, rejection, and thermal efficiency of the separation process [55].

In AGMD a gap filled with stagnant air is introduced between the permeate side of the membrane and a condensation surface that is being cooled by a coolant from the other side. Thus, the vapor diffuses not only through the membrane but also through the air gap until it eventually condensates on the cold surface (Figure 3b) [29,30,56]. The air gap imposes a thermal insulation and reduces the thermal losses via heat conduction but also increases the mass transfer resistance for the transported molecules due to longer diffusion distances [28,56,61]. In AGMD, the condensed permeate has typically no contact with the membrane surface [56], thus reducing the risk of wetting on the permeate side.

In VMD a vacuum is applied to the permeate side of the membrane. The gradient between the low pressure on the permeate side and the saturation pressure of the respective molecules on the feed side generates the driving force needed to evaporate and transport the volatile molecules across the membrane (Figure 3c) [30]. The condensation typically takes place outside of the membrane module [29]. VMD is characterized by high fluxes and relatively good thermal efficiencies in comparison with the other main MD configurations and particularly suitable for membranes with high thermal conductivities such as ceramic membranes [55,56]. This is because the low pressure on the permeate side leads to the removal of inert gases (air is being continuously evacuated) from the pores that act as resistance to the mass transport and averts strong temperature polarization effects due to the thermal insulation by the vacuum that lowers the heat transported via conduction considerably [56]. Since there is no direct contact with any kind of solution with the permeate side of the membrane, VMD is considered particularly suitable for the separation of molecules with low surface tensions such as alcohols from diluted aqueous solutions [28,57,58]. VMD is catching up to DCMD in regard to the most research MD configuration

accounting for 35 % of all MD publications focus on a specific configuration [30]. The main drawbacks of VMD are the relatively extensive experimental set-up (vacuum pump and external condenser) and the higher risk of pore wetting induced by the vacuum [28,56,59,60].

In SGMD a cold inert gas sweeps through the air gap on the permeate side carrying the evaporated water or volatile molecules to an external condenser (Figure 3d) [41]. The driving force is the vapor pressure gradient across the membrane based on the temperature difference from the feed solution to the sweep gas and the vapor saturation of the sweep gas. A drawback of this configuration is that due to the low thermal capacity of the gas stream and the absorption of warm vapor and conducted heat, a strong increase of the temperature of the sweep gas can occur during operation which in return limits the driving force considerably [56]. Another disadvantage is the technical outlay of this configuration and high equipment costs related to it since a compressor and a large external condenser must be integrated in the process [54,56]. In SGMD, the liquid permeate has no direct contact with the permeate side of the membrane, which makes this configuration suitable for the evaporation of compounds with low surface tension such as alcohols from aqueous solutions [62,63].

Several unconventional MD configurations such as thermostatic sweeping gas membrane distillation, multi-effect membrane distillation, vacuum multi-effect membrane distillation, material-gap membrane distillation and permeate-gap membrane distillation have also been developed and investigated with the goal to lower energy consumption and improve the permeate flux [64]. If the SGMD is combined with the AGMD and the inert gas is passed through the gap between the membrane and a cold condensation surface the configuration is referred to as thermostatic sweeping gas membrane distillation (TSGMD). Part of the vapor condenses on the condensation surface as in AGMD and the rest of the vapor is condensed through the external condenser as used in SGMD. The cold condensation surface is implemented to moderate the increase in the sweeping gas temperature and to subsequently enhance the driving force along the membrane length [63,65]. In multi-effect membrane distillation (MEMD) the AGMD set-up consists of several stages which utilize an internal heat recovery system to enhance the thermal efficiency of the process. In this configuration the cold feed is used to cool the condensation surface. Furthermore, the feed for subsequent stages is preheated by absorbing the heat that is released through the condensed vapor produced by the prior membrane stage [64,66,67]. This configuration was promoted as the commercial Memstill® MD system [66]. Another configuration that was developed to increase the energy efficiency is the vacuum multi-effect membrane distillation (V-MEMD). The V-MEMD configuration is characterized by a vacuum that is applied to the MEMD set-up [67]. As characteristic for MEMD, this configuration involves multiple evaporation–condensation stages [64] but uses the low absolute pressure on the permeate side to decrease unnecessary heat

transfer and to continuously remove inert gases from the process to minimize the mass transport resistance. This configuration is being marketed through the companies SolarSpring GmbH membrane solutions and Memsys Water Technologies GmbH and has achieved commercialization [67]. When the air gap in AGMD is filled with a material the configuration is called Material Gap Membrane Distillation (MGMD). The materials that are typically used are poly urethane (sponge), poly propylene mesh, sand, aluminum mesh and pure water in addition to other materials [64,68,69]. The material is used to either decrease the mass transfer resistance for the vapor molecules while minimizing the heat transfer via heat conduction (low thermal conductivity material) leading to a better thermal efficiency or to simply decrease the mass transport resistance and enhance the permeate flux without considering the thermal efficiency of the process (high thermal conductivity material) [70–72]. If the air gap is filled with pure water or permeate the configuration is also referred to as permeate gap membrane distillation (PGMD) or liquid gap membrane distillation (LGMD) [64]. The liquid in the air gap reduces the mass transfer resistance since the evaporation of the vapor takes immediately places inside the liquid when reaching the permeate side just like in DCMD but exhibits lower heat losses. Another benefit of the PGMD configuration is the use of feed water as a coolant inside the module while effectively preheating the feed solution [69].

2.2 General Characteristics of Membranes used in Membrane Distillation Processes

2.2.1 Hydrophobicity

Most importantly, MD membranes are required to be hydrophobic to prevent the liquid feed from infiltrating the pores of the membrane subsequently leading to the contamination of the permeate side [41] while facilitating the vapor transport. In DCMD, infiltration of the permeate/coolant into the pores of the permeate side of the membrane can also take place. The infiltration on the permeate side can affect the mass transport positively or negatively which is decided by the layer design and thermal conductivity of the membrane [55]. The extent of the hydrophobicity of a membrane surface is proportional to the free surface energy of the membrane and is typically characterized by contact angle (CA) measurements (typically on flat surfaces) or liquid entry pressure (LEP) tests [73–75]. The contact angle is the angle at which a surface is in contact with a liquid interface and determines the wettability of a surface regarding a specific liquid and the surrounding gas phase. The angle represents the mechanical equilibrium of a liquid drop under the action of the interfacial tensions (= surface tension or surface energy) between the membrane

surface and the gas phase γ_{GS} [N/m], the membrane surface and the liquid γ_{LS} [N/m] and the liquid and the gas phase γ_{LG} [N/m].

If a liquid drop rests without a significant spread on the surface (θ_{CA} > 90°, Figure 4a) the surface is hydrophobic towards the liquid. If the drop of a liquid spreads significantly (θ_{CA} < 90°, Figure 4b on a surface the surface is hydrophilic towards the liquid [76].

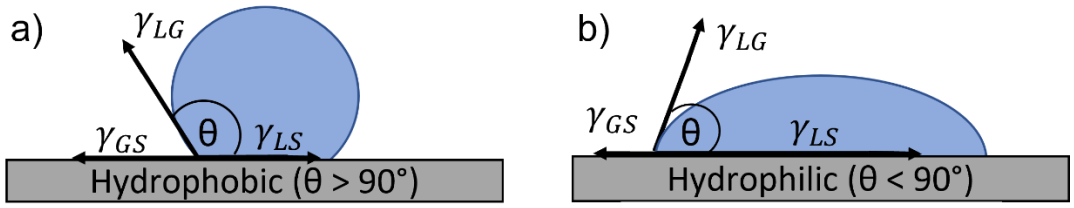

Figure 4: Schematic representation of a contact angle describing a hydrophobic surface (a: θ > 90°) and a contact angle defining a hydrophilic surface (b: θ < 90°)

A contact angle related parameter that is being used to describe the wettability of rough or heterogenous surfaces is the contact angle hysteresis (CAH). This parameter is defined as the mathematical difference between the advancing contact angle and the receding contact angle (on a heterogenic or rough surface the receding CA is typically smaller than the advancing CA.) which are formed if a droplet slides down a slope or is being enlarged or shrunk respectively. [77,78]. Models that consider the roughness and the porosity of a surface have also been proposed and are discussed in more depth elsewhere [79–81].

The LEP is defined as the minimum transmembrane pressure that is required to overcome the hydrophobic forces of the membrane surface and is considered an important key parameter of membranes that are utilized in MD processes [28]. The LEP is strongly dependent on the morphological parameters and the free surface energy of the membrane as well as the feed temperature and composition of the feed [82]. Franken et al. 1987 [73] proposed a model to determine the LEP based on the Laplace-Young equation:

$$LEP = \Delta P = \frac{2B_g cos\theta_{CA}\gamma_{LG}}{r_{max}} \quad (1)$$

With B_g [-] as a fit parameter to describe the pore geometry ($0 < B_g \leq 1$, 1 for perfect cylindrical pores), θ_{CA} [°] is the intrinsic contact angle of the wetting liquid with the membrane surface γ_{LG}

[N/m] is the liquid surface tension and r_{max} [m] as the maximum pore radius. It must be stated that many membrane types do not have cylindrical pores which can lead to an underestimate of the CA [83]. Servi et at. 2016 [84] suggest that the Laplace-Young equation is generally not applicable to membranes with lower contact angles (< 90°). Alternative LEP models have been proposed and are described elsewhere [83–85]. Schneider et al. 1988 [86] recommend a minimal LEP of 2.5 bar (pure water, no surfactants in the feed) to ensure process stability but it is important to notice that the structure and the morphology of the membrane (e.g. pore size distribution, pore shape, surface roughness and heterogeneity) as well as the operating conditions (high temperatures) and the feed composition (liquids with low surface tension) can require a considerably higher LEP [87,88].

2.2.2 Morphological Properties

The general dependency of the permeate flux J on pore size, porosity, membrane thickness and tortuosity can be expressed as [89]:

$$J \propto \frac{r^n \varepsilon}{\tau \delta} \tag{2}$$

where r represents the mean pore radius [m], ε the porosity [-], τ the tortuosity [-], δ the membrane thickness [m] and n the mass transfer mechanism (n = 0 for pure molecular diffusion, n = 1 for pure Knudsen diffusion, n = 2 for pure viscous flow). It is obvious that the pore size and porosity is proportional and the membrane thickness and tortuosity inverse proportional to the permeate flux of the membrane. The pore size determines the mechanisms that govern the mass transport while affecting the selectivity of the membrane. Large pore sizes favor high permeate fluxes but are more likely to be affected by pore wetting. This is the reason why a compromise must be found regarding an ideal pore size that facilitates high mass transfer rates while offering an acceptable risk of wetting [61,90]. Pore sizes larger 0.2 µm make molecular diffusion (DCMD) or viscous flow (VMD) the dominant mass transfer mechanism whereas Knudsen diffusion dominates in pores that are smaller than 0.2 µm as the free path length of the diffusion molecules exceeds the pore diameter (detailed explanation see chapter 2.5.2). Since the effect of molecular diffusion is constant over the pore size [91] and large pores are at a higher risk of pore wetting there is little incentive to use pore sizes greater than 0.5 µm [86]. The pore size distribution is also an important

parameter to consider while selecting a membrane since even a small share of very large pores can lead to the infiltration of feed into the pores and the subsequent contamination of the permeate. Woods et al. 2011 [92] stated that the error caused by the pore size distribution on the mass transport modeling is smaller than 5 % if the pore size distribution is smaller than σ_g < 1.2 for $d_{p,av}$ > 50 nm (DCMD) and VMD: σ_g < 1.07 for all pore sizes (VMD) with σ_g as the geometric standard deviation factor [-] and $d_{p,av}$ as the mean pore diameter [m]. Li et al. 2016 [93] stated that the pore size distribution can be neglected for the mass transfer simulations for Knudsen numbers below 1 and membranes with narrow small size distributions. A high porosity does not only result in a large evaporation surface but also decreases the heat loss via conduction due to the better thermal insulation by the large void fraction. It must be stated that a high porosity leads to a reduced mechanical robustness which can partly be compensated by laminating a membrane on a backing structure [90]. The tortuosity is defined by the ratio of the pore length to the membrane thickness. There is little scientific insight on the impact of the tortuosity on the MD performance since this parameter is very difficult to determine [56,94]. It is generally understood the tortuosity should be as small as possible since the permeate flux is dependent on the distance the vapor molecules must travel to pass through the membrane [41]. The membrane thickness is another membrane property that must be optimized regarding other membrane parameters such as the thermal conductivity. Just like the tortuosity the membrane thickness defines the distance the vapor molecules must travel therefore affecting the overall mass transfer resistance greatly. Even though a thinner membrane reduces the mass transfer resistance it may also lead to a stronger temperature polarization and consequently to a loss of driving force [41]. This means the optimal thickness of a membrane should always be defined in relation to the thermal conductivity of the membrane and the chosen MD configuration [55,90]. In case of multi-layer membranes (= asymmetric membranes, e.g. support layer plus membrane layer that defines the selectivity) the membrane properties should be optimized for each layer.

2.2.3 Thermal Conductivity and Membrane Stability

The thermal conductivity of membranes is often described as a function of the thermal conductivity of the membrane material and gas phase as well as the porosity. The void fraction serves as a thermal insulation. Different models are used to predict the thermal conductivity of polymeric membranes (the Maxwell model is the most commonly used one) and are described elsewhere [55,94,95]. Since the selection of the most suitable model remains uncertain [94] (especially for ceramic membranes [55]) and the accurate determination of the thermal conductivity is not trivial,

this parameter is often used as a fitting parameter in mass transfer models as well [56,96,97]. In general, the thermal conductivity of a MD membrane should be as low as possible [98]. The thermal conductivity can affect the energetic efficiency of the MD processes strongly since a high thermal conductivity leads to an increased heat transfer via heat conduction. High thermal conductivities lead to stronger temperature polarization effects which significantly reduce the driving force. This effect is mainly observed in DCMD configuration since the permeate side of the membrane system is in direct contact with the cooling liquid. In VMD, the effect of the thermal conductivity is considerably smaller. There is no fluid on the permeate side and the heat transferred is predominantly latent heat carried by the vapor [55].

Ideally all types of MD membranes should exhibit a good thermal stability up to 100 °C [41] and a sufficient chemical robustness in respect to the environment they are utilized in. Some authors state that there is no need for MD membranes to be as mechanically robust as membranes that are utilized in pressure driven membranes processes [41] or do not state any requirements regarding the mechanical stability at all [17]. The risk of membrane degeneration due to abrasion and scaling processes caused by high loads of dissolved salts and forming salt crystals in the feed is rarely the focus of MD studies. It is important to state that the stability of asymmetric membranes should extend to all layers and coatings to ensure the hydrophobic characteristics of the membrane and a sufficient selectivity.

2.3 Polymeric Membranes in Membrane Distillation

The utilization of stretched polytetrafluoroethylene (PTFE) or phase inverted polypropylene (PP) and polyvinylidene fluoride (PVDF) (typical pore size: 0.02 µm ≤ d_p ≤ 1.0 µm [30]) membranes in MD processes is state of the art [17]. PTFE membranes are manufactured by sintering or stretching whereas PP membranes are generally made by stretching and thermal phase inversion and PVDF membranes by phase inversion [44]. These membranes were not particularly developed for MD processes [17] but favor them due to their hydrophobic surfaces (surface energy: $9.1 \cdot 10^{-3}$ N/m to $30.3 \cdot 10^{-3}$ N/m), high porosities (60 % to 90 % [[28,41,50]) and low thermal conductivities (material: 0.45 W/(m K) to 0.50 W/(m K) [90]. The tortuosity of polymeric membranes is often assumed to be inverse to the porosity [99,100], assumed to have a value of 2 [91,101,102] or used as an calibration factor [56,97] whereas the membrane thickness of polymeric MD membranes typically ranges between 20 µm and 500 µm [28,91]. Laganà et al. 2000 [103] concluded that the optimal thickness for typical polymeric membranes utilized in DCMD applications ranges between 30 µm and 60 µm. Regarding membrane stability, PTFE membranes

(PTFE is the most tested MD membrane material [41]) exhibit a very good chemical and thermal stability [52] but lack mechanical strength [17,104]. The relatively high porosity of polymeric membranes can make them sensitive towards compaction (even at lower pressures) which can lead to reduced mass transfer rates [105]. Additionally, Zhang et al. 2012 [104] showed that the compaction of a PTFE membranes leads to a significant increase of their thermal conductivity due to the decrease of their porosity. To adapt the thickness or mechanical strength of polymeric membranes the polymeric membrane layer is usually added to a support (mostly PP [90]) [106]. Alternatively, a dual-layer membrane with different surface characteristics (hydrophilic layer + hydrophobic layer) can be used. In this case the hydrophobic layer should be as thin as possible [52]. However, Adnan et al. [106] found that the addition of a support can lead to a decline of permeate flux of up to 56 %. PVDF and PP membranes are characterized by a lower chemical and thermal stability than PTFE membranes but are not as complicated and expensive to manufacture [54,107]. In summary, polymeric membranes can be quite sensitivity toward aggressive chemicals (PVDF, PP), high temperatures (PP) and oxidizing agents (PVDF, PP) which restricts the way the membranes can be cleaned and regenerated and types of chemical that can be used for the pretreatment to prevent scaling or biological growth altogether [34]. PTFE which is generally very robust regarding aggressive chemicals and high temperatures can degenerate quickly due to mechanical forces, such as salt crystals causing abrasion or compaction. In respect to the environment they are applied to these membranes might not be suited for long-term operation [51]. Polymeric membranes typically come in a flat or a tubular shape. These membrane types must be integrated into a housing called module to facilitate the evaporation process and collect the permeate [30]. Commonly used are plate and frame (= flat sheet), spiral wound and hollow fiber modules. In a plate and frame module (Figure 5a), flat sheet membranes and spacers are layered together between plates. These modules are often used for lab-scale MD experiments since they are easy to clean and to replace. The disadvantage of flat-sheet modules is that a support structure for the membrane is needed and only low packing densities (= ratio of membrane area to packing volume) are achieved [61]. In a spiral wound module (Figure 5b) flat sheet membranes and spacers are wrapped around a perforated collection tube. The feed solution flows across the membrane surface (in an axial direction) while the permeate moves radially to the center and drains through the holes of the collection tube. Spiral wounds modules benefit from a high packing density and an acceptable energy consumption [61]. In a hollow fiber module (Figure 5c) thousands of hollow fibers are packed together and sealed inside of a tube. Typically, the feed solution is run through the inner lumen of the fibers while the permeate is collected on the outside of the fibers or vice versa [44]. The advantages of hollow

fiber modules are the high packing density. The disadvantages of polymeric hollow fiber modules are difficult to clean and maintain while being prone to fouling processes [61].

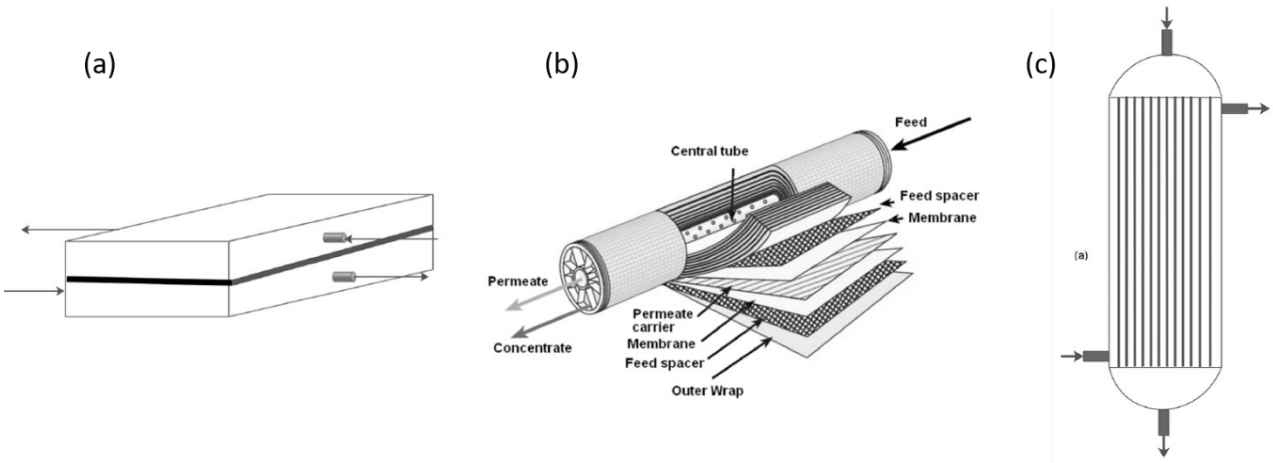

Figure 5: Schematic depiction of a plate and frame module in cross-flow mode (a) [30], the flow regime inside a spiral wound module (b) [108] and a hollow fiber module in cross flow mode (c) [30]

2.4 Ceramic Membranes in Membrane Distillation

Ceramic membranes have rarely been investigated in MD processes due to their hydrophilic surface characteristics [109] and relatively high manufacturing costs [76,110]. Generally, ceramic membranes exhibit superb chemical, mechanical and thermal stability and can withstand environments that are too aggressive for polymeric membranes [110–113]. They are more resistant against biological activity and can be cleaned with high concentrations of aggressive chemicals and at high temperatures and high pressures [76,114,115]. This can ensure a life-span that is hardly achieved by polymeric membranes [51]. The study of Guerra and Pelligrino 2013 [116] suggest that if the potential lifespan of ceramic membranes is considered they can be economically competitive to polymeric membranes. Ceramic membranes made from metal oxide materials such as alumina, titania and zirconia are most commonly used in MD processes (predominantly alumina membranes) [51] while mixed oxides and non-oxide materials such as silicon carbide, silicon nitride, sialon and cordierite are rarely used or have not been studied at all [36,51,55,117]. Ceramic membranes are mostly asymmetrically structured and composed of a mechanical support, several intermediate and a final membrane layer. The macro-porous support secures the mechanical stability of the membrane. The consecutively coating with the intermediate membrane layers reduces the pore size of the overall membrane with each coating step until a thin layer of a final (= ‘active membrane layer’) membrane can be applied (the smaller the final pore size the more intermediate layers are required) that defines the selectivity of the membrane

[113]. The thickness of each intermediate and the final layer can vary between 10 µm to 20 µm where the support is a few mm wide [76]. If the final membrane layer were coated onto the support directly the slurry would infiltrate the large pores of the support completely and cause pore blocking. Figure 6 shows the cross-sectional image of an asymmetrically structured Al_2O_3 membrane with a final pore size of 400 nm.

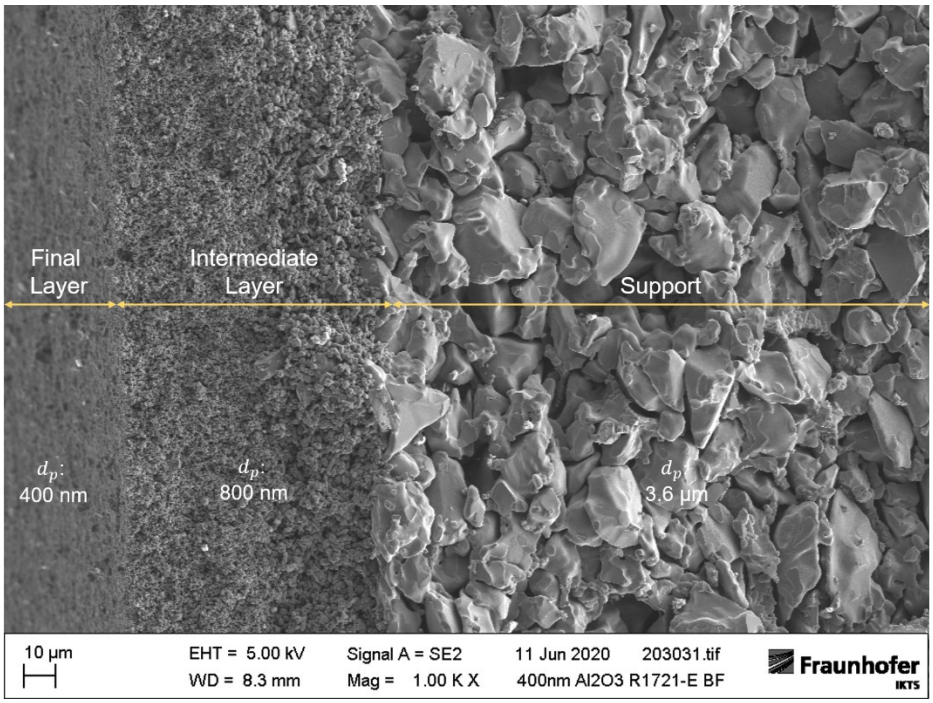

Figure 6: Cross-sectional SEM image of an asymmetrically structured tubular Al_2O_3 membrane with a final pore size of 400 nm [55]

The shape of ceramic membranes is decided by the form of the support which is a tube or a flat sheet. The supports are made by extrusion (tubular) or tape casting (flat sheet) and a subsequent sintering process whereas the intermediate membrane layers are made by a slurry coating and sintering process [113]. Tai et al. 2020 [51] give a good overview on the different manufacturing processes needed to make ceramic membranes. The planar shaped membranes (rectangular sheets or disks) are commonly used in Lab-scale MD test beds because the membrane surface can be inspected easily. Planar membranes are assembled within a plate and frame module. A plate and frame module uses different rows of flat sheet membranes creating a multi-layer structure. One unit consists of a support plate, a membrane sheet and feed and permeate spacers. A membrane sheet connected to a permeate spacer is bent over the support plate forming an envelope open to the feed at both sides. The corners of the membranes are sealed to the support.

A multitude of these units are called cassettes. The stacked together cassettes make up the plate and frame module membrane module. Plate and frame modules are easy to clean and allow the uncomplicated maintenance or replacement of specific units but only enable low packing densities between 30 m²/m³ to 500 m²/m³ [76,110]. Tubular ceramic membranes can be single channel tubes, combine single channels with small diameters within a bundle (e. g. hollow fibers and capillaries) or possess multiple channels (multichannel tubes or honeycomb elements (Figure 7a and Figure 7b).

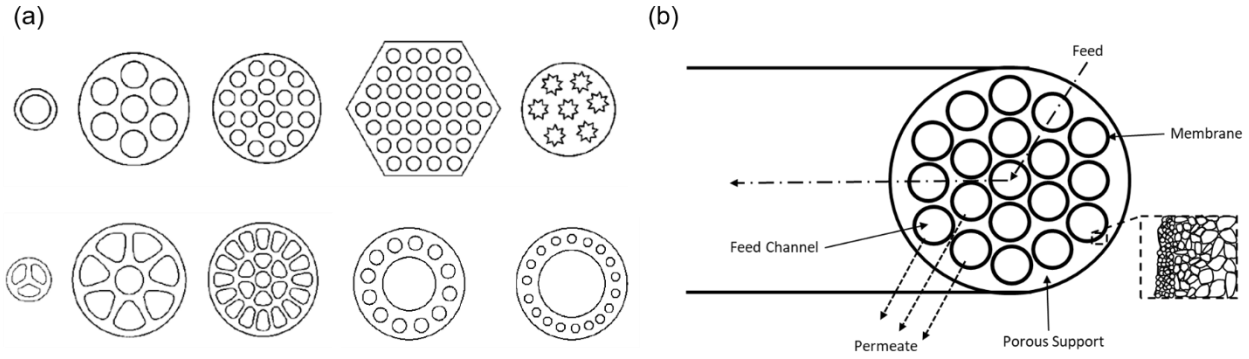

Figure 7: Schematic representations of the cross-section of different ceramic (single and multichannel) tubes (a) [113], cross section of a multichannel membrane element (b)

If the membrane layers are coated into the lumen of the tubular support the feed will be run through the lumen and the permeate will be collected on the outside of the tube (= 'inside out' configuration, Figure 7b). If the supports are coated with the membrane layers on the outside the feed will be run along the outside and the permeate collected inside the lumen of the tube ('outside in' configuration) [51]. Typically, a hollow fiber module (Figure 8c) consists of hundreds or thousands of hollow fibers with diameter smaller or equal to 0.5 mm while the capillaries in a capillary bundle module have a diameter between 0.5 mm and 5 mm [51,76]. The fibers are glued with a resin into the module enabling dead end or cross flow mode. The benefit of a hollow fiber module is the high packing density of up to 9000 m²/m³ and the relative ease of cleaning and replacing of single fibers [76,110]. The main drawback of ceramic hollow fiber modules is the fragility of the single fibers [76]. Tubular modules (Figure 8a and Figure 7b) are created out of single channel or multichannel tubes which come in different shapes, sizes and with a different number of channels (e. g. up to 163 channels). The specific design and number of channels define the packing density that range from 30 m²/m³ to 250 m²/m³ for single channel tube modules, 130 m²/m³ to 400 m²/m³ for

multichannel modules (Figure 8b) and up to 800 m²/m³ for honeycomb multichannel modules [118].

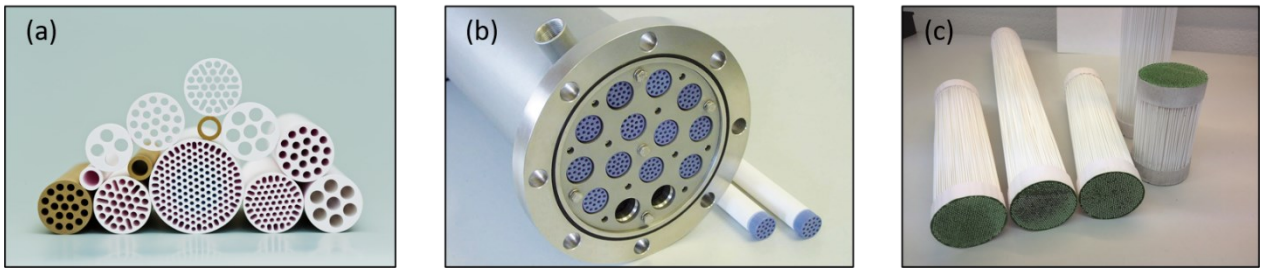

Figure 8: Multichannel Tubes (Fraunhofer IKTS 2020) (a), Multichannel Tube Module (Fraunhofer IKTS 2020) (b), Hollow Fiber Module without Housing (Fraunhofer IKTS 2020) (c)

Most studies with the focus on ceramic membranes use membranes with pore sizes in the range of 0.15 µm to 0.32 µm and porosities from 25 % to 50 % [36]. The tortuosity of ceramic membranes ranges from 1.5 to 5 and is often correlated with the porosity [76]. The thermal conductivity of ceramic membranes is considerably higher than the values for polymeric membranes. That is because the thermal conductivities for inorganic materials used for ceramic membranes (e. g. Al_2O_3: 15 W/(m k) to 30 W/(m K) and cordierite: 1.2 W/(m K) to 2.5 W/(m K) [55,119]) are significantly higher than the material values for polymeric materials (Chapter 2.3) and the porosities of the membranes are significantly lower. Schnittger et al. 2020 [55] reported thermal conductivities for ceramic single channel membranes (Al_2O_3, TiO_2, mixed oxides and cordierite) in the range from 0.5 W/(m K) to 1.6 W/(m K) and showed that the thermal conductivity is mainly depended on the support properties. As illustrated in Figure 9a, the ceramic membranes most widely used in MD processes are made from Al_2O_3. It can also be seen that tubular membrane types/modules (mostly single channel tubes) are widely utilized in MD processes and VMD is the most often studied MD configuration (Figure 9b and Figure 9c) [36].

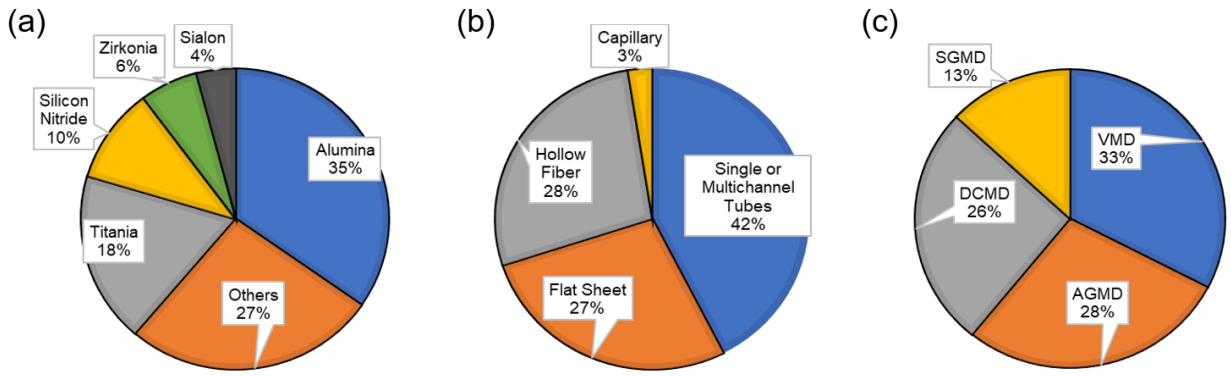

Figure 9: Material of ceramic membranes used in MD processes (a), ceramic membranes and membrane modules used in MD processes (b) and configuration studied using ceramic membranes (c), (adapted from [36])

It can be assumed this is based on the experience research institutes and manufactures of ceramic membranes have obtained on a specific material and the fact that single channel tubes are ideal for membrane prototype production. Ceramic membranes are mostly studied in VMD followed by AGMD because these configurations limit the effects of the relatively high thermal conductivities of ceramic membranes due to the thermal insulation.

2.4.1 Surface Modification of Ceramic Membranes

As stated before, most ceramic membranes have pronounced hydrophilic surface properties caused by the presence of hydroxyl groups (an exception is for instance silicium carbid which can be hydrophobic or hydrophilic in respect of the carbon at the surface) on the metal-oxide surfaces [34,120]. However, the surface characteristics of ceramic membranes can be rendered hydrophobic through surface modification processes. One method of surface modification in favor of hydrophobic characteristics is the creation of rough surfaces (e. g. through plasma etching and nanotexturing, solidification of melted alkyl ketene dimer, microwave plasma-enhanced chemical vapor deposition, anodic oxidization of aluminum and soaking of porous alumina-gel films in boiling water) [109]. The vast majority of studies reported grafting as the method that was used to modify the surface of ceramic membranes [36]. Grafting refers to the attachment of hydrophobic molecules via hydrogen, ionic, van der Waals or covalent bonds (typically silanes [74], Figure 10) onto the surface of membranes [121] reducing the free surface energy [82]. A silane is a molecule composed of one Si atom and four functional groups (SiX_4). Organosilanes are the group of silanes predominantly used for the surface modification due to the simple and short modification

procedure. They refer to compounds that contain at least one carbon-silicon bond which acts as an organic functional group and a hydrolysable functional group such as ethoxy, methoxy or chlorine [82,122–126] (Figure 10a). The organosilane is activated via hydrolysis to yield a reactive silanol species. The reactive substituents (halogen and alkoxy groups) are transformed into hydroxy (OH) groups (Figure 10b). Subsequently the ceramics are immersed in the activated silane solution which causes the reactive silane molecules to be chemisorbed to the ceramic surface via a condensation reaction. The excess Si-OH groups of the chemisorbed silane can form links with the other silane molecules through Si-O-Si bonds forming a polymeric siloxane network on the membrane surface [37,74,82,125–127]. This layer (containing non-polar organic functional groups such as $–CH_3$, $–CH_2–CH_3$, and –(CF2)5–CF3) causes a significant reduction in the free surface energy resulting in hydrophobic surface characteristics [37]. The hydrophobic surface is chemically and mechanically relatively stable due to the strong immobilization of the molecules on the surface, resulting from chemical bonding and the presence of intermolecular attraction forces [74,82]. The effectiveness of the modification is strongly affected by the concentration of the silane agent and the length of the hydrophobic chain, the amount of hydroxyl groups on the surface, the membrane surface roughness and the grafting time and grafting temperature [36,82]. Beside the immersion method that is applied the most, chemical vapor deposition (CVD) and the sol-gel method are also used in the grafting process and are described in detail by Ahmed et al. 2015 [82]. From the group of organosilanes, chloroalkylsilanes, fluoroalkylsilanes, hexadecyltrimethoxysilane, and polydimethylsiloxane have been used successfully in grafting processes [36]. Fluoroalkylsilanes (FAS) are the most widely used modification agents [51,55,109,121,128–134] and from the FAS group, mainly 1H,1H,2H,2H-perfluorooctyltriethoxysilane and 1H,1H,2H,2H-perfluorodecyltriethoxysilane have been studied [120]. For instance, Schondelmaier et al. 2002 [135] gave insight into the orientation and self-assembly of FAS while Kujawa et al. 2014 [131] showed that the length of the FAS molecule has a significant impact on the extent of the hydrophobic surface characteristics of modified TiO_2 membranes. Kujawa et al. 2016 [109] determined the size of the hydrophobic chains of PFAS molecules in the range of 1.5 nm to 2.2 nm and showed they do not cause a considerable blocking of macro pores. The use of non-fluorinated grafting agents has also been promoted since FAS are considered to be toxic [136] and expensive [51,137]. Fluorine-free compounds such as nonfluorinated alkyl silanes [137,138], polydimethylsiloxane (PDMS) [139] or carbon nanotubes (CNTs) have also been investigated [140] [51].

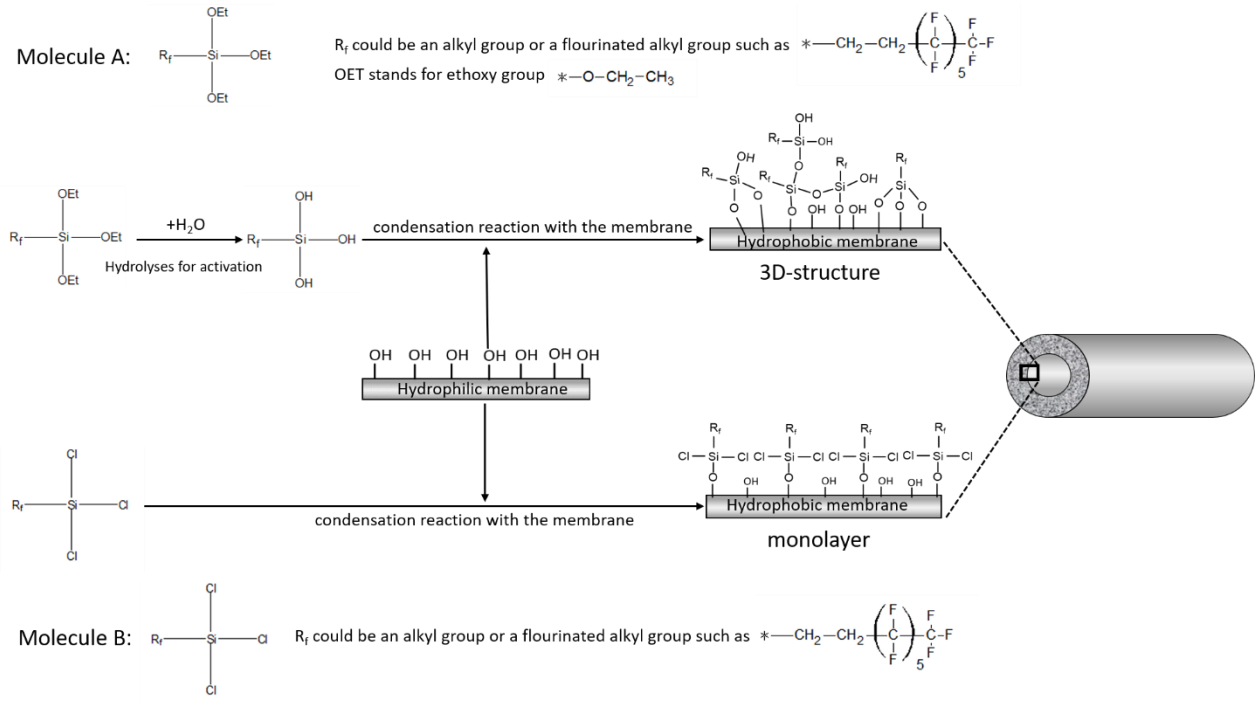

Figure 10: Schematic overview of the grafting process using two different molecules for the surface modification of tubular ceramic membranes

2.5 Heat and Mass Transfer

In all MD configurations, heat and mass transport through the pores take place simultaneously. Theoretical MD models describe the mass and heat flux in respect to the membrane characteristics, MD configurations and temperature and concentration polarization phenomena and are based on the Kinetic Theory of Gases [39]. The transport process can be separated into three different stages, the vapor generation (feed-side, stage 1), the separation/transportation (membrane, stage 2) and the condensation of the water vapor (permeate-side, stage 3) [90]. Generally, the permeate flux in MD through a porous medium can be described by the following equation [28,56]:

$$J = B_m \Delta p_m = B_m (p_{f,m} - p_{p,m}) \quad (3)$$

with B_m as the mass transfer coefficient [kg/(m² h Pa)] that is mainly defined by the membrane characteristics and $P_{f,m}$ and $P_{p,m}$ as the respective water vapor partial pressures [Pa] at the membrane interfaces on the feed- and permeate-side accounting for the driving force in

consideration of temperature and concentration polarization [90]. While DCMD is the most researched MD configuration [30] VMD offers the most benefits for the use of ceramic membranes in MD processes. Therefore, theoretical considerations such as the heat and mass transfer as well as experimental MD investigations were limited to these two configurations.

2.5.1 Driving Force in Consideration of Temperature and Concentration Polarization

In general, the area in which temperature and concentration polarization occurs is being referred to as the temperature or concentration polarization boundary layer (Figure 11) [89,141]. Temperature polarization has a greater impact on the mass transfer then concentration polarization. Both polarization effects can partly be compensated by generating a turbulent flow regime [44,90].

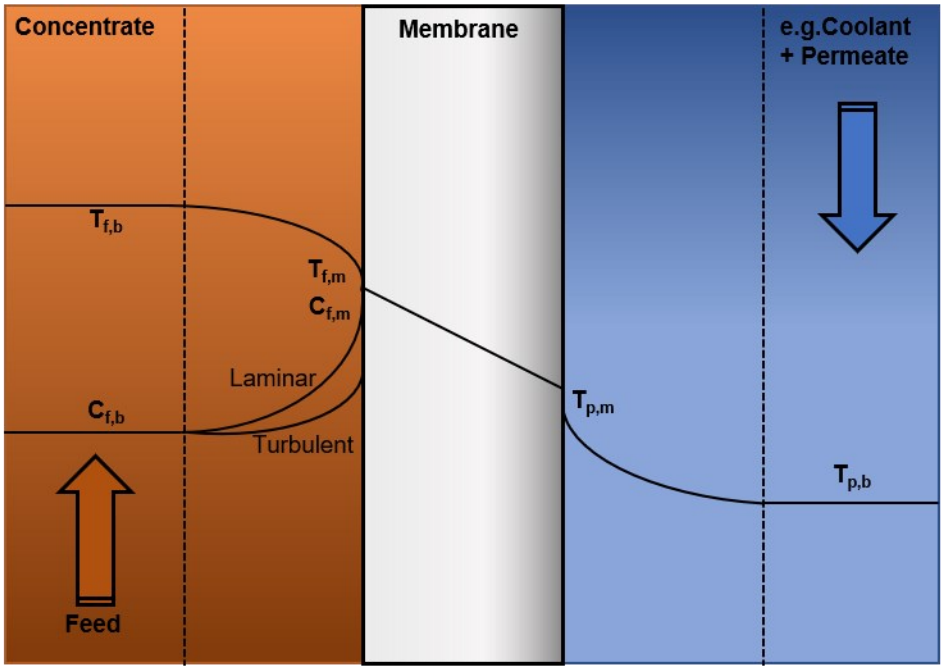

Figure 11: Temperature and Concentration Polarization Profile in DCMD $c_{f,b}$: bulk stream solute concentration, $C_{f,m}$: interfacial solute concentration, $T_{f,b}$: Temperature of the bulk stream on the feed-side, $T_{p,b}$: Temperature of the bulk stream on the permeate-side)

Temperature polarization refers to a heat gradient between the interfaces of the membrane and the corresponding bulk streams [142]. Temperature polarization is caused by two heat transfer

processes. Firstly, heat is transported across the membrane matrix (Q_c) through heat conduction which can account for a significant part of the heat transport [143]. Secondly, heat is transported from the feed to the permeate-side due to the evaporation process and the vapor transferred (Q_v). The total heat Q_t that is transported through the membrane in DCMD can be described in steady state as follows [39]:

$$Q_t = Q_v + Q_c = J\Delta H_v + \frac{k_m}{\delta}(T_{m,f} - T_{m,p}) \quad (4)$$

with ΔH_v as is the enthalpy of vaporization of water [J/mol] and k_m as the thermal conductivity of the membrane [W/(m K)]. The enthalpy of vaporization can be expressed as follows [144]:

$$\Delta H_v = 1.91846 \cdot 10^6 \left(\frac{T}{T - 33.91}\right)^2 \quad (5)$$

with T as the feed temperature [K]. The energy efficiency (EE, also referred to as thermal efficiency) [-] of a single MD process at lab-scale is defined as the ratio of the vaporization heat associated with the vapor transport through the membrane pores over the total heat flux ($Q_c + Q_v$) [17,39]:

$$EE = \frac{Q_v}{Q_t} \quad (6)$$

The interfacial temperatures can only be measured with great effort and are commonly determined via empirical relationships regarding the liquid characteristics and the flow regime (Eq. 7 and 8), the thermal conductivity and thickness of the membrane and the heat of vaporization of water [41,90]. The temperature on the membrane interface (T_m) in consideration of the temperature polarization can be calculated for the feed and permeate side in DCMD as follows [145]:

$$T_{m,f} = \frac{\frac{k_m}{\delta}\left(T_{b,p} + \frac{h_f}{h_p}T_{b,f}\right) + h_f T_{b,f} - J\Delta H_v}{\frac{k_m}{\delta} + h_f\left(1 + \frac{k_m}{\delta h_p}\right)} \tag{7}$$

$$T_{m,p} = \frac{\frac{k_m}{\delta}\left(T_{b,f} + \frac{h_p}{h_f}T_{b,p}\right) + h_f T_{b,p} + J\Delta H_v}{\frac{k_m}{\delta} + h_p\left(1 + \frac{k_m}{\delta h_f}\right)} \tag{8}$$

with h_f und h_p as the heat transfer coefficients [J/(m² s K)] on the feed and permeate side respectively and $T_{b,f}$ and $T_{b,p}$ as the temperature of the bulk feed and cooling solution [K] on the respective membrane side. Due to the thermal insulation caused by the vacuum and the external condensation of the vapor, temperature polarization is typically only located at the feed-side in VMD processes and the heat transfer via conduction is neglected [90]:

$$T_{m,f} = T_{m,b} - \frac{J\Delta H_v}{h_f} \tag{9}$$

The heat transfer coefficients of the feed and the permeate side can be determined via the following equation [146]:

$$h_{f,p} = \frac{Nu_{f,p}k_{f,p}}{d_{h(f,p)}} \tag{10}$$

with Nu as the Nusselt number [-], $k_{f,p}$ as the thermal conductivity of the feed and coolant solution [W (m K)] and $d_{f,p}$ as the hydraulic diameter [m] on the feed and permeate side, respectively. The Nusselt number describes the convective to conductive heat transfer ratio and can be calculated as a function of the Reynolds [-] and Prandtl number [-] that characterize the fluid flow regime [90,146]:

$$Re_{f,p} = \frac{\rho_{f,p} v_{f,p} d_{h(f,p)}}{\eta_{f,p}} \tag{11}$$

$$\mathrm{Pr}_{f,p} = \frac{C_{P(f,p)} \eta_{f,p}}{k_{f,p}} \tag{12}$$

with ρ as the density [kg/m³], v as the flow velocity [m/s], η as the dynamic viscosity [Pa s] and C_P as the heat capacity [kJ/(kg K)] of the respective solution. The density of the feed and coolant stream can be calculated as follows [147]:

$$\begin{aligned}\rho_{f,p} = {} & 750.2834 + 26.78c - 0.26389c^2 + (1.90165 - 0.11734c + 0.00175c^2)T \\ & + (-0.003604 + 0.0001701c - 0.00000261c^2)T^2\end{aligned} \tag{13}$$

with c as the salinity [wt.%] and T the temperature [K] of the respective stream. Having determined Re and Pr the right semi-empirical correlation for the Nusselt number can be chosen [90,148,149]:

laminar: $$Nu = 0.298\, Re^{0.646}\, Pr^{0.316} \tag{14}$$

turbulent: $$Nu = 0.036\, Re^{0.96}\, Pr^{0.33}\, 0.33 \frac{d_h}{L}^{0.055} \tag{15}$$

with d_h as the hydraulic diameter [m] and L as the length of the membrane tube. Concentration polarization refers to an increased concentration of solutes at the membrane interface on the feed-side due to the evaporation and transfer of pure water [44]. The elevated solute concentration imposes a negative impact to the mass transfer due to the limited water and heat transport by the slow diffusion process and by lowering the partial vapor pressure which leads to a driving force reduction. Concentration polarization effects can be neglected for the permeate side in all MD configurations (in DCMD, usually pure water acts as cooling liquid) [90]. The concentration on the membrane interface $c_{m,f}$ [mol] on the feed side can be calculated in consideration of concentration polarization as follows [39]:

$$c_{m,f} = c_{f,b} \exp\left(\frac{J}{K_f \rho_{b,f}}\right) \quad (16)$$

with $c_{f,b}$ as the concentration of the bulk feed solution [mol], K_f as mass transfer coefficient [kg/(m² s Pa)] on the feed side and $\rho_{b,f}$ as the density of the bulk feed solution. The mass transfer coefficient on the feed side can be determined using this equation [146]:

$$K_f = \frac{Sh_f \, D_f}{d_{h,f}} \quad (17)$$

with Sh_f as the Sherwood number (convective to diffusional mass transfer ratio [90]) [-] and D_f as the bulk feed diffusion coefficient [m²/s] that can be approximated as follows [150]:

$$D_f = \frac{k_B T}{6\eta\pi r_{NaCl}} \quad (18)$$

with k_B as the Boltzmann constant [m² kg/(s² K)] and r_{NaCl} as the hydrodynamic radius of the diffusing NaCl molecule [150,151]. To calculate the Sherwood number the following equation can be used [90]:

$$Sh_f = \alpha Re_f^{\beta} Sc_f^{\gamma} \quad (19)$$

with Sh_f as the Schmidt number (provides the ratio of momentum diffusivity to mass diffusivity) [-] and α, β, and γ are experimentally determined coefficients for a specific module design and fluid velocity. Johnson and Nguyen 2017 give an overview of different values of α, β, and γ in relation to the specific flow type [90]. The Schmidt number [-] can be calculated as [146]:

$$Sc_f = \frac{\eta_f}{\rho_f \, D_f} \quad (20)$$

If the interfacial feed concentration $c_{m,f}$ and the temperatures on the interface of the membrane on the feed and permeate side $T_{m,f}$ and $T_{m,p}$ are known the actual driving force for the MD process can be calculated. For this, the partial pressure of water vapor $p_{0(f,p)}$ must be calculated based on the calculated interfacial temperatures and the Antoine Equation [152]:

$$p_{0(f,p)} = \exp\left(23.5377 - \frac{4016.3632}{T_m - 38.6339}\right) \tag{21}$$

In DCMD, $p_{0(p)}$ is considered to be equal to $p_{p,m}$ due to the coolant liquid being free of dissolved salts while the water activity $a_{w,f}$ of the feed solution at the membrane interface (consideration of concentration polarization effect) can be used to determine the actual partial pressure of the water vapor at the interface of the membrane on the feed side [152]:

$$p_{f,m} = p_{0(f)} a_{w,f} \tag{22}$$

The water activity can be calculated based on the NaCl molality x [mol/kg]) using the following correlation [153]:

$$a_{w,f} = 1 - 0.03112 x_{m,f} - 0.001482 x_{m,f}^2 \tag{23}$$

2.5.2 Mass Transfer and Mass Transfer Resistance

In addition to the driving force the mass transfer mechanisms for the vapor molecules inside membrane pores must be determined to model the mass flow. The most commonly models used to describe the resistance to vapor transport through a porous membrane regarding to molecular diffusion, Knudsen diffusion and viscous flow (also referred to as Poiseuille flow) are the so-called Schofield model and Dusty-Gas Model (DGM). Both models are based on the kinetic theory of gas [102,142,146,152,154,155]. Both models consider the morphological properties such as pore size, porosity and tortuosity but do not include the pore size distribution. However, it was concluded that the effect of the pore size distribution on the mass transfer can be neglected for membranes

with a relatively narrow pore size distribution [101,145]. Although both models have proven to show good results the use of the DGM has been recommended. It is considered to be more correct from a physical point of view and offers a more simple approach to determine morphological properties using data from gas permeance tests [152]. The disadvantage of the DGM is that it was derived for isothermal fluxes while the MD process is a non-isothermal process. However, it was shown that an average temperature can be used successfully within the DGM [44,89,156]. In the most general form (accounting for molecular diffusion, Knudsen diffusion and viscous flow) the mass transport in MD can be expressed as [89]:

$$\frac{J_i^D}{D_{ie}^K} = \sum_{j=1\neq i}^{n} \frac{p_j J_i^D - p_i J_j^D}{D_{ij,e}^M} = \frac{-1}{RT} \nabla p_i \tag{24}$$

$$J_i = J_i^D + J_i^V \tag{25}$$

$$J_i^V = \frac{-p_i \frac{\varepsilon r^2}{8\tau}}{RT\eta} \nabla \mathrm{p} \tag{26}$$

$$D_{ij,e}^M = \frac{\varepsilon}{\tau} p D_{ij} \tag{27}$$

$$D_{ie}^K = \frac{2\varepsilon r}{3\tau} \sqrt{\frac{8RT}{\pi M_i}} \tag{28}$$

with J_i^D, J_i^V and J_i are the diffusive, viscous and total fluxes of the component i, p and η are the total pressure [Pa] and dynamic viscosity [Pa s] of the mixture and p_i is the partial pressure of the component i [Pa], respectively. $D_{ij,e}^M$, D_{ie}^K represent the effective molecular and Knudsen diffusion coefficients, R is the universal gas constant [J/(mol K)] and M_i is the molar weight of component i [kg/mol]. Surface diffusion has generally been neglected in MD modeling due to the high porosities of (polymeric) MD membranes [89] and the little affinity of water molecules to the hydrophobic surfaces [41]. Which of the aforementioned transport mechanisms is dominating inside the membrane pores is dependent on the pore size of the membrane, the mean free path

of the molecules transported and the presence of air in the pores [29]. Molecular diffusion is dominant when the probability of vapor molecule – air molecule collisions is greater than the probability of molecule – pore wall collisions whereas Knudsen diffusion is dominant if vapor molecule – pore wall collisions are more likely [41]. Viscous flow describes the convective transport of vapor molecules through the membrane and is relevant for larger membrane pores that are void of air molecules (for instance by applying a vacuum to the permeate side of the membrane as in VMD mode) [90]. The actual operative vapor transfer mechanism through a given membrane pore is determined by the Knudsen number Kn which is defined as [41]:

$$Kn = \frac{\lambda_{v,a}}{d_p} \tag{29}$$

where d_p is the average pore diameter of the membrane [m] and $\lambda_{v,a}$ the mean free path of a water vapor molecule in air [m] at a given temperature and pressure [146,157].

$$\lambda_{v,a} = \frac{K_B T}{\sqrt{2}\pi p \sigma_v^2} \tag{30}$$

with σ_v as the collision diameter for water vapor [m] and T and p as the temperature [K] and pressure [Pa] inside the pores of the membrane respectively. [39]. For instance, $\lambda_{v,a}$ is 0.11 µm at 60 °C and at atmospheric pressure [158]. A Knudsen number smaller or equal to 0.01 indicates that solely molecular diffusion is governing the mass transfer whereas a Knudsen number greater or equal to 10 indicates that only Knudsen diffusion is taking place in the pores [41]. Pore sizes of MD membranes often range from 0.1 µm to 0.45 µm. Thus, typical Knudsen numbers are in the range of 0.2 to 1.0 which suggests a superposition of Knudsen and molecular diffusion for most MD membranes [90]. Based on Eq. 22 to Eq. 25 a combined Knudsen and molecular diffusion model can be used to quantify the vapor flux in DCMD [39,41,89,154]:

$$B_m^{K+M} = \left(\frac{1}{B_m^K} + \frac{1}{B_m^M}\right) = \frac{1}{RT\delta}\left[\frac{\tau}{\varepsilon d_p}\left(\frac{9\pi M_W}{8RT}\right)^{\frac{1}{2}} + \frac{p_{air,av}\tau}{\varepsilon p D_v}\right]^{-1} \tag{31}$$

with B_m^K and B_m^Mdescribing the mass transport resistance in regard to Knudsen diffusion and molecular diffusion respectively [kg/(m² h Pa)], T as the average temperature inside the pores, M_W the molecular weight of water [kg/mol], $p_{air,av}$ the average air pressure in the membrane pores [Pa], p the total pressure [Pa] and D_v the diffusion coefficient of water vapor in air [m²/s]. For water vapor in air, pD_v (temperature range: 273 – 373 K) can be expressed as [159]:

$$pD_v = 1.895 \times 10^{-5} T^{2.072} \tag{32}$$

The following equation can be used to describe the mass transfer resistance of water vapor in VMD in consideration of a superposition of Knudsen diffusion and viscous flow [39,41,42,160]:

$$B_m^{K+V} = \left(\frac{1}{B_m^K} + \frac{1}{B_m^V}\right) = \frac{\varepsilon d_p}{RT\tau\delta}\left(\left(\frac{8RT}{9\pi M_W}\right)^{\frac{1}{2}} + \frac{d_p p_{av}}{2^5 \eta_v}\right) \tag{33}$$

where η_v is the viscosity of water vapor [Pa s] and p_{av} the average pressure inside the pores [Pa]. The viscosity of water vapor can be calculated as follows [161]:

$$\eta_v = \eta_0 + \frac{T_0 + T_S}{T + T_S}\left(\frac{T}{T_0}\right)^{\frac{3}{2}} \tag{34}$$

with T as the temperature of the water vapor [K], T_0, as the zero point for water vapor ($= 373\ K$), $T_S\ as\ the$ Sutherland constant ($= 890\ K$) and η_0 as the dynamic viscosity of water vapor at T_0 ($= 1.23 \cdot$ Pa s). If the operational pressure on the permeate side is below the vapor pressure of the water vapor only traces of air are present in the pores and molecular diffusion can be neglected [160].

2.6 The Impact of Process Parameters

The performance of a MD process is determined by the system design, membrane characteristics and the process parameters. Whereas the membrane facilitates the selective gas transport from

the feed to the permeate side (affected by the mass transfer resistance imposed by the properties of the membrane) the process parameters mainly define the magnitude of the driving force that enables the phase change and mass transport but also determine the properties a membrane should exhibit. For instance, the feed temperature at the membrane surface (consideration of temperature polarization) and the absolute pressure applied to the permeate side will define a theoretical driving force for the mass transfer across the membrane. However, the feed composition can reduce the driving force significantly (high concentrations of salts) and decrease the selectivity of the membrane greatly (presence of organic substances lowering the surface tension of the feed). Insight into the impact of process parameters is imperative to an efficient system design, choosing the right membrane and process control. In the following sections an overview of the relevant process parameters such as fluid temperatures and flow velocities, feed concentration and absolute pressure applied and their impact on process performance in DCMD and VMD is given.

2.6.1 Feed Temperature, Experimental Set-Up and Cooling of the Permeate Side

There is an exponential correlation between the partial water vapor pressure and the feed temperature as described by the Antoine Equation (Eq. 21). This means that increasing feed temperatures (at the same coolant temperature or absolute pressure) should lead to the exponential increase of the driving force and permeate flux [152]. Some authors argue that the increased permeate flux due to higher feed temperatures is also caused by better diffusion coefficients [162–165] and reduced temperature polarization effects (due to a change of the hydrodynamic conditions such as the viscosity) [95,166]. It is also argued that high feed temperatures lead to disproportionate temperature polarization effects that partly compensate for the positive effects of elevated feed temperatures and dampening the exponential relationship between the feed temperature and the driving force [91]. Furthermore, an increasing feed temperature lowers the surface tension of the feed solution which results in lower LEP values. This can increase the risk of membrane wetting throughout the MD process significantly [167]. Therefore, for any given membrane type the highest (ideal) feed temperature should be experimentally determined (regarding the LEP and energy efficiency) instead of choosing the highest temperature the system setup allows. The partial water vapor pressure gradient across the membrane at any given feed temperature can be increased by reducing the coolant stream temperature in DCMD [90]. Due to the very nature of the exponential correlation (the lower the temperature the smaller the effect) between the liquid temperature and the partial pressure of water vapor it is advised to balance the increasing energy intake necessary to allow lower coolant

temperatures with the increase of the driving force. The condenser temperature in VMD should be chosen to allow the condensation of all water vapor at the given feed temperature and permeate pressure in consideration of the theoretical driving force, the distance between the membrane module and the condenser and the design of the condenser.

2.6.2 Absolute Pressure on the Permeate Side

In VMD the gradient between the partial water vapor pressure on the permeate side (defined by the pressure applied to the permeate side) and the partial pressure of the water vapor on the feed side determines the driving force for the process. This means that lowering the absolute pressure on the permeate side at a constant feed temperature should linearly increase the permeate flux. Moreover, lowering permeate pressures lead to the constant removal of inert gases from the membrane pores, thus lowering the mass transfer resistance in VMD. In addition, the vacuum generates a better thermal insulation resulting in reduced temperature polarization effects [168]. This effect is more pronounced for lower pressures. One must keep in mind that lower absolute pressures on the permeate side considerably increase the risk of wetting which would substantially decrease the permeate quality. Furthermore, the lower the absolute pressures on the permeate side the lower must be the condenser temperatures to facilitate condensation of the vapor molecules as well as the higher the increased electrical energy consumption by the vacuum pump.

2.6.3 Feed Composition

The feed composition affects the performance of the MD processes in two ways. Firstly, high salinity levels lead to a significant reduction of the driving force. The partial vapor pressure on the feed side is decreased by a lower water activity due to higher concentrations of salt ions [89,169]. Additionally, high salinities change the hydro-mechanic properties of the feed such as the viscosity and density limiting the heat transfer from the bulk feed to the interface of the membrane which amplifies temperature polarization effects [89,90]. The effect of concentration polarization is considered to be small compared to that of temperature polarization [170–172]. In DCMD, high salt concentrations at a low driving forces can lead to osmotic distillation and the subsequent dilution of the feed solution through water vapor generated at the permeate side [91,142]. Secondly, surfactants such as organic compounds lower the surface tension of the feed which can considerably increase the risk of wetting [129]. The specific feed composition can require a

pretreatment of the feed to reduce the risk of wetting and fouling (fouling is referred to the accumulation of deposits on the surface of a membrane).

2.6.4 Feed and Coolant Flow Velocity

The increase of the flow velocity on the feed side can lead to an increased permeate flux [61,165].This is caused by the reduction of temperature and concentration polarization due to the increased turbulence leading to a higher heat transfer coefficient (better convective heat transfer from the bulk feed to the interface of the membrane) and better solute mixing [50,61]. An increase of the permeate flow velocity increases the heat transfer on the permeate side of the membrane module by limiting temperature polarization which in return results in higher permeate fluxes. It can also be stated that this effect is limited and highly dependent on the process parameters and membrane characteristics [173,174].

3 Material and Methods

To assess the limitations and strength of ceramic membranes in MD processes as well as to facilitate membrane optimization and mass transfer modelling, the impact of relevant membrane properties on the performance in MD processes must be evaluated. To be able to do that, different membrane types (e. g. variation of material, layer design, thickness, pore size) were manufactured and subsequently characterized regarding their specific properties. This chapter will present the membrane types studied in the scope of this work, depict the experimental set-up and describe the characterization methods and test procedures in detail to quantify relevant membrane properties and to assess the membrane performance. The selection of the different membrane types that were manufactured and investigated for this work (e.g. what type of material, hydrophobic agent and pore size) was based on preliminary studies, technical experience at the institute and literature reviews. While common characterization methods (e.g. mercury porosimetry) were used to identify standard properties such as pore size and porosity (also used for quality control on samples) special characterization methods were used to determine membrane characteristics (e.g. thermal conductivity scanning) that particularly affect membrane performance in MD. MD tests were limited to DCMD and VMD tests because they are the most popular MD configurations and due to the fact that VMD offers specific benefits for ceramic membranes (e.g. less affected by the relatively high thermal conductivities of ceramic membranes). The mass transfer modelling was limited to the VMD configuration because of the complex wetting behavior of modified asymmetric ceramic membranes in DCMD (cooling liquid infiltrates the support pores) as well as the assumption that VMD is the more suited configuration for ceramic membranes.

3.1 Membranes and Membrane Preparation

Single channel tubular membranes (SCT) with a variety of different properties (e. g. pore size, layer design, wall thickness and surface modification) were made from the materials Al_2O_3, TiO_2, cordierite (14 % MgO, 35 % Al_2O_3, and 51 % SiO_2) and mixed oxide (80 % Al_2O_3 and 20 % ZrO_2). The support tubes of ceramic membranes were made by extrusion and sintering whereas the intermediate and top layers (if applicable) were made by slurry coating and sintering. At least three membranes per membrane type were manufactured. The membranes were coated inside the channel facilitating an inside-out separation process. Beside the typical asymmetrically structured ceramic membranes, symmetrically structures membranes made from Al_2O_3 and TiO_2 were

manufactured. These membranes have a uniform pore size over their complete cross section and do not require a coating process. All membrane tubes had a length of 250 mm, an outer diameter of 10 mm and a channel diameter between 6.5 mm and 8.5 mm. The end sections of the tubes are sealed up to 1.5 cm on each side with a glass cap (only asymmetrically structed single channel tubes) enabling the inflow of the feed inside the membrane tubes (ensure proper sealing) using custom-build membrane modules made from PVC or stainless steel. Symmetrically structured membranes were manufactured exhibiting one uniform membrane layer (one pore size over the whole cross section of the membrane, Figure 12). The properties of the symmetrical membranes were adjusted by varying the composition of the raw material, particle size and sintering temperature. As symmetrical membranes possess a single layer, they can be fabricated in a single extrusion and sintering step which makes them more cost-efficient. Symmetrical membranes do not need an end sealing due to their homogeneous cross section which prevents any leakage of the feed solution into the membrane structure if their surface is modified.

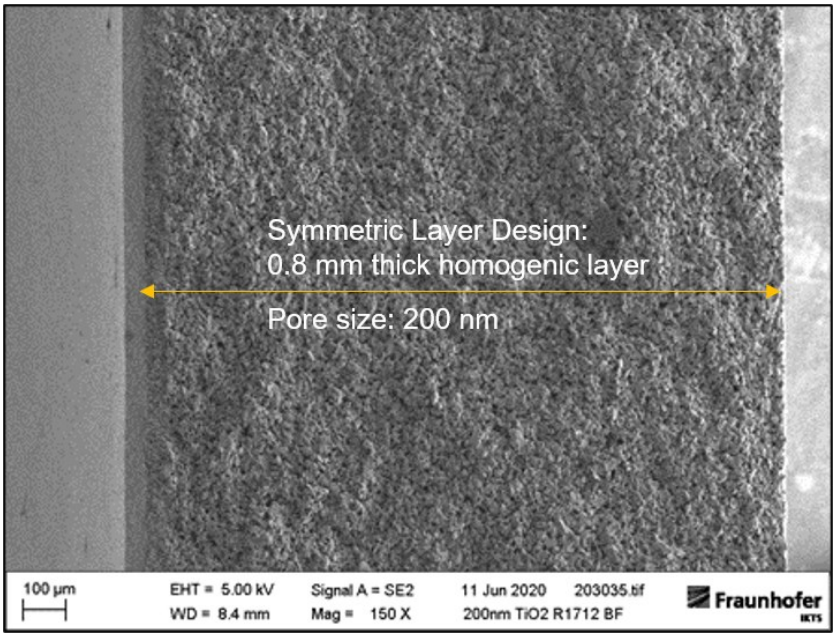

Figure 12: Cross sectional SEM image of a symmetrical TiO_2 membrane with an average pore size of 200 nm and a wall thickness of 0.8 mm (Fraunhofer IKTS 2020)

Throughout this work the pore size that is reported for an asymmetrically structured membrane refers the pore size of the final layer (if not stated otherwise) whereas the pore size reported for a symmetrically structured ceramic membranes represents the pore size of the whole cross section of the membrane.

For the modification of the tubular ceramic membranes described above a solution containing 1 wt.% or 2 wt.% of one of the following hydrophobic agents:

- Fluorinated alkyl triethoxysilane (labelled ‘HOC’)
- Fluorinated alkyl trichlorosilane (labelled ‘HOG’)
- Non-Fluorinated n-Octyltriethoxysilane (labelled ‘HOM’)

and (if applicable) an organic solvent with an acid catalyst was prepared. The modification was done by soaking the membranes in the solution and applying a vacuum. After drying, the membranes were thermally processed to achieve a stable hydrophobic coating. The hydrophobic agents HOC and HOG were chosen because they are commonly used by the Fraunhofer IKTS and have been successfully applied to membranes utilized in MD processes [129]. The hydrophobic agent HOG was chosen as a non-fluorinated alternative that showed promising results in preliminary contact angle measurements (Chapter 4.1.2).
Table 5 at the end of this section displays all single channel membrane types as well as their pore size, porosity, thickness, layer design and modification that were manufactured, characterized, and tested within the scope of this thesis.

3.2 Characterization of Membrane Properties

3.2.1 Standard Characterization Methods

Every batch of ceramic membranes developed and manufactured at the Fraunhofer IKTS undergoes a series of standard characterization methods for quality control. The properties are typically determined on samples and include the pore size distribution, porosity, mechanical stability (pressure resistance) and for new membrane types the crystallographic structure. The characterization methods used to determine those properties are listed in Table 1 and are described in detail elsewhere (Ref. column Table 1). MD performance affecting parameters such as pore size and porosity are listed in respect to the membrane type in Table 5.

Table 1: Overview of standard membrane characterization methods for quality control

Characterization Method	Testing in Accordance	Parameter	Ref.
Mercury Porosimetry	DIN ISO 15901-1	Pore Size Distribution and Porosity	[175]
X-Ray Diffraction Imaging	DIN EN 13925	Crystallographic structure	[176]
Water Absorption	ISO 18754	Density and Open Porosity	[177]
Burst Pressure Test	AAW 274	Internal Pressure Resistance	[178]

3.2.2 Steady State Gas Permeation

Steady state gas permeation tests using nitrogen (also referred to as N_2 permeance tests) were used to determine the N_2 permeance of all tubular membranes. Before the test, the membranes were dried at 120 °C in a drying cabinet for two hours and subsequently cooled to ambient temperature in a desiccator. The membrane tubes were installed into a stainless-steel module and sealed by O-rings made of Viton®. The membrane module was installed in the gas permeation apparatus, equipped with mass flow controllers (MKS Instruments US, model: MF1) and pressure transducers (MKS Instruments US, Model: 722A and 223B). The membrane was then fed with nitrogen (N_2) in dead-end mode (retentate side closed). The tests were conducted at ambient temperatures. The volume flow on the feed side was set to a rate that the differential pressure between the feed side and the permeate side (ambient pressure) could kept constant at 1000 mbar. The feed and permeate pressures were recorded. This procedure was first conducted with the as-received ceramic supports and then repeated for the same supports after each subsequent coating step until the final membrane layer was reached.

3.2.3 Thermal Conductivity

The measurement of the thermal conductivity of the membranes has been performed by thermal conductivity scanning, a technique developed by the Leibniz Institute of Applied Geoscience (LIAG) in Hannover based on the work of Popov et al. 1999 [179]. This non-destructive method is

based on scanning the sample's surface with two movable and focused infrared temperature sensors in combination with a heat source (Na-vapor lamp), which is operated continuously at constant heating power throughout the measurement. By aligning the study sample and the reference sample with a known thermal conductivity (k_{ref}) along the scanning direction, the unknown thermal conductivity of the sample (k_{sample}) can be determined as follows:

$$k_{sample} = k_{ref}\left(\frac{\Theta_{ref}}{\Theta_{sample}}\right) \tag{35}$$

with Θ_{ref} and Θ_{sample} as the maximum increase of temperature along the reference and the sample material, respectively. One set of example results of this measurement is schematically shown in Figure 13. To derive the best possible absorption of the heat, as well as to avoid reflection of the heat at the sample surface (which would lead to significantly falsified data), specimens needed to be prepared with a thin layer (< 100 µm thickness) of black acrylic paint.

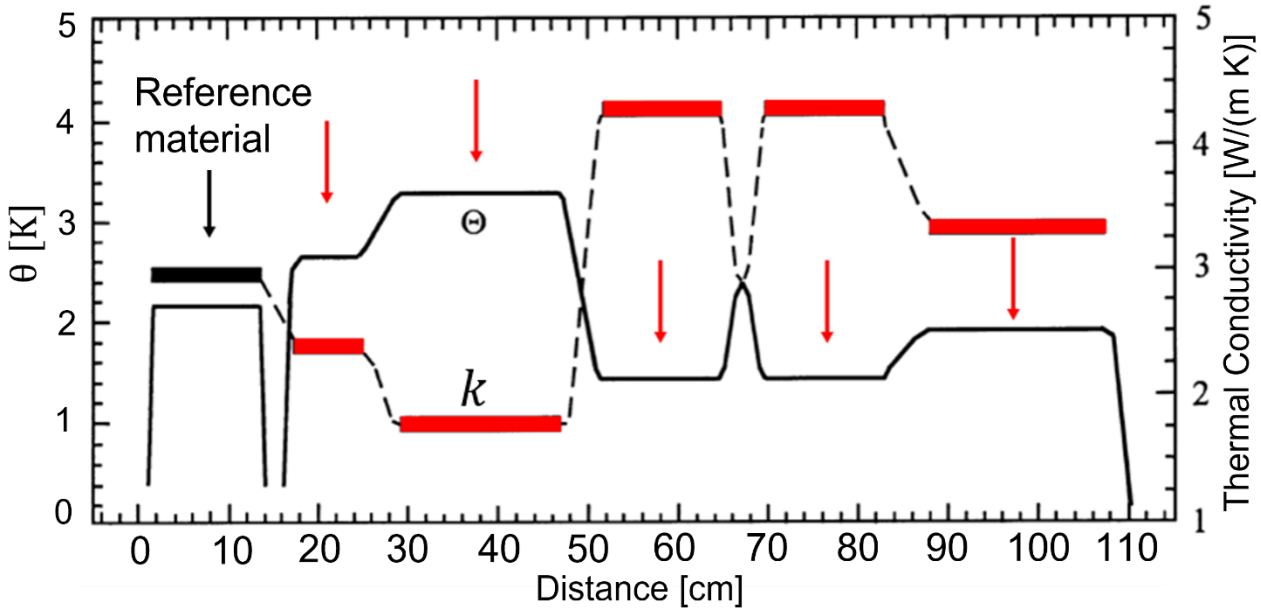

Figure 13: Schematics of a thermal conductivity scan (modified after Popov et al. 1999), the solid line indicates the measured temperature rise (Θ) of the reference (black arrow) and unknown sample material (red arrows). The dashed line presents the calculated thermal conductivity of the samples (k_{sample}) based on the equation 35 [55].

To derive the best possible absorption of the heat, as well as to avoid reflection of the heat at the sample surface (which would lead to significantly falsified data), specimens needed to be prepared with a thin layer (< 100 µm thickness) of black acrylic paint.

3.2.4 Contact Angle

The contact angles (CA) were measured using an optical contact angle measuring and contour analysis systems (OCA 20, Figure 14) from DataPhysics Instruments GmbH (DE) at room temperature. A drop of demineralized water was applied to the surface of a modified Al_2O_3 flat sheet membrane (final pore size: 200 nm) by a dispensing needle. An illuminating screen generates a homogenic background. A camera records the image of the resting drop from the side. This image was then sent to a screen and evaluated regarding the stationary CA using the image processing software of the measuring device. CA measurements on porous membranes are generally only conclusive, if the surface characteristics of the membrane do not lead to the instant filtration of the drop into the pores.

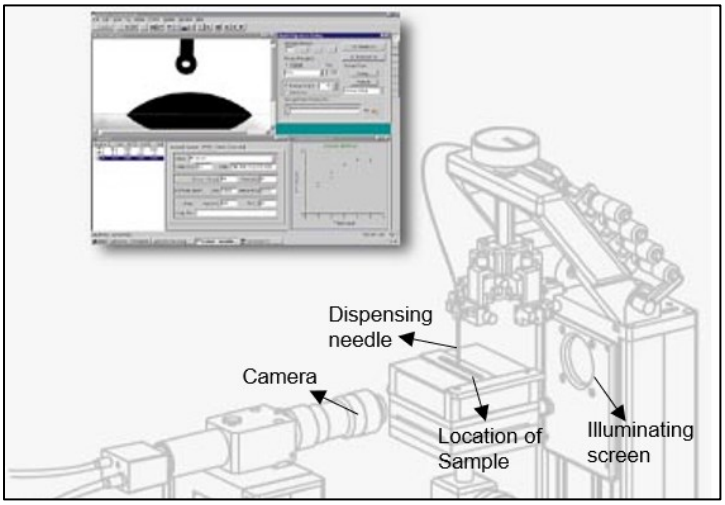

Figure 14: Illustration and components of the optical contact angle measuring and contour analysis systems (OCA 20)

To determine the static, advancing and receding CA (and subsequently the CAH: advancing CA - receding CA) the 'needle method' was used. A fixed volume of 5 µL of demineralized water was pushed out of the needle and attached to the surface by moving the table towards the drop (Figure 15a and Figure 15b). The CA that developed in respect to the physio-chemical properties of the water drop and surface was considered the static CA. The volume on the water drop on the

table is then increased by 50 µL via the dispensing needle so the contact area between the drop and the membrane surface is increased (Figure 15c). The CA that was then measured was considered the advancing CA (Figure 15c). Subsequently the liquid is then sucked back into the needle to decrease the contact area between the drop and the membrane surface while the CA is measured (Figure 15d). This CA was considered the receding CA.

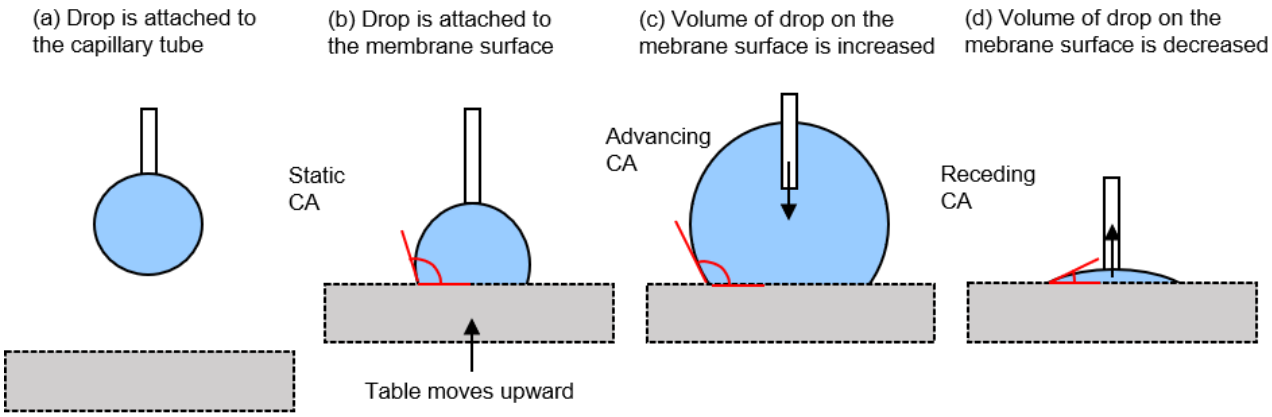

Figure 15: Measurement of the static, advancing and the receding CA

3.2.5 Liquid Entry Pressure

As stated before, the LEP refers to the hydrostatic pressure at which pore wetting takes place. If the feed infiltrates the membrane pores it contaminates the permeate side of the membrane and affects the permeate quality. Thus, the LEP is a practical indicator if a tubular membrane does have the required hydrophobicity to be utilized in MD under a certain set of operational parameters (e. g. feed composition and feed temperature).

Bevor testing the membranes had to be dried at a minimum of 90 °C for 2 hours to remove the moisture from the membrane pores. After cooling down in the desiccator, the membranes were then installed into the LEP test rig (Figure 16).

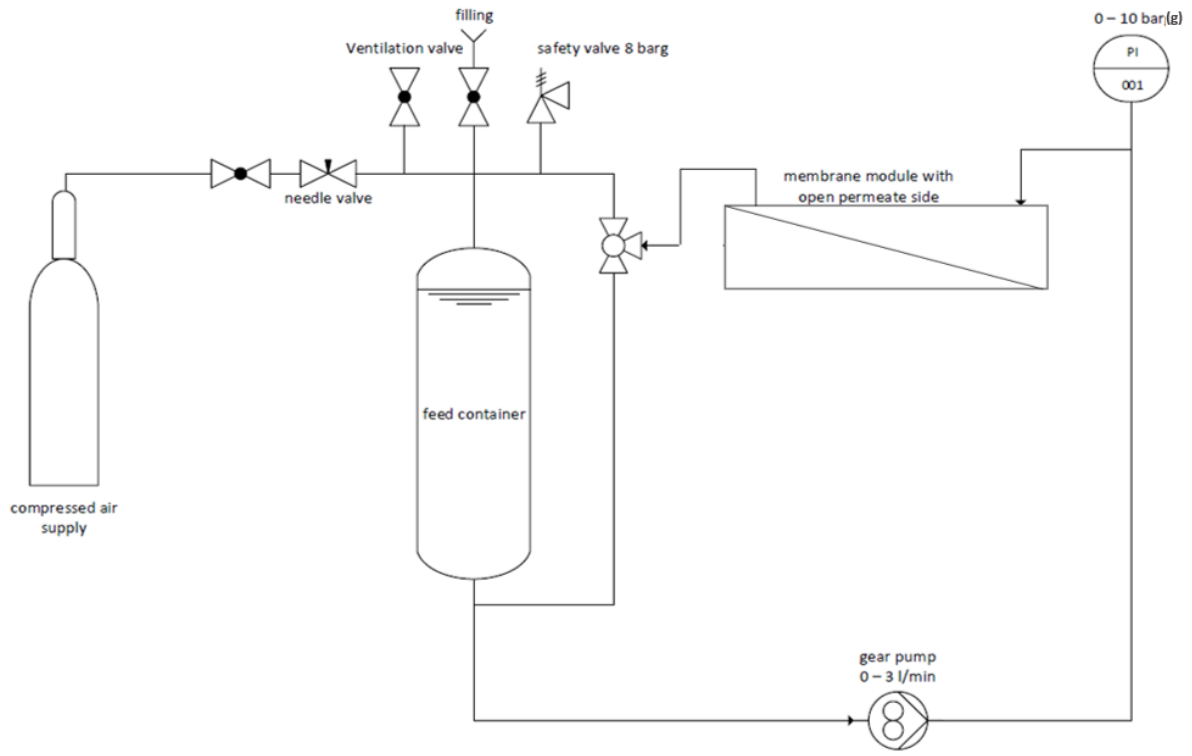

Figure 16: P&I Diagram of the LEP test bed

The membrane tubes were installed using stainless steel connectors in a way that allowed the permeate side of the membrane tube to be visually accessible. This enabled the recognition of wetting by eyesight as well as the identification of the specific wetting area (Figure 17). The test solution was circulated from the stainless-steel feed tank (HPS Handels GmbH DE, 2.25 L) through the membranes using a gear pump (Ismatec DE, model: BVB-Z/Z-120). The heating of the testing solution was realized by two heated metal hoses (Hillesheim GmbH DE, model: H300 DN4 and DN10) and the respective temperature controller (Hillesheim GmbH DE, model: HT43-25F). The hydrostatic pressure was increased in 0.1 bar to 0.5 bar increments using compressed air (in-house system) and a manually adjustable needle valve (Nupro Company US, model: SS-4BK) and monitored via a pressure gauge (Swagelok US, 0 -10 bar(g). Each increment was held for a minimum of two minutes. The minimum hydrostatic pressure that led to the infiltration of the testing solution into the membrane pores and leading to droplets forming on the outside (permeate side) of the membrane was considered the LEP. A safety valve (LORCH Sicherheitsventile GmbH & Co. KG DE, opening pressure: 8 bar) was integrated in the system. A minimum of three tests was conducted for all membrane types.

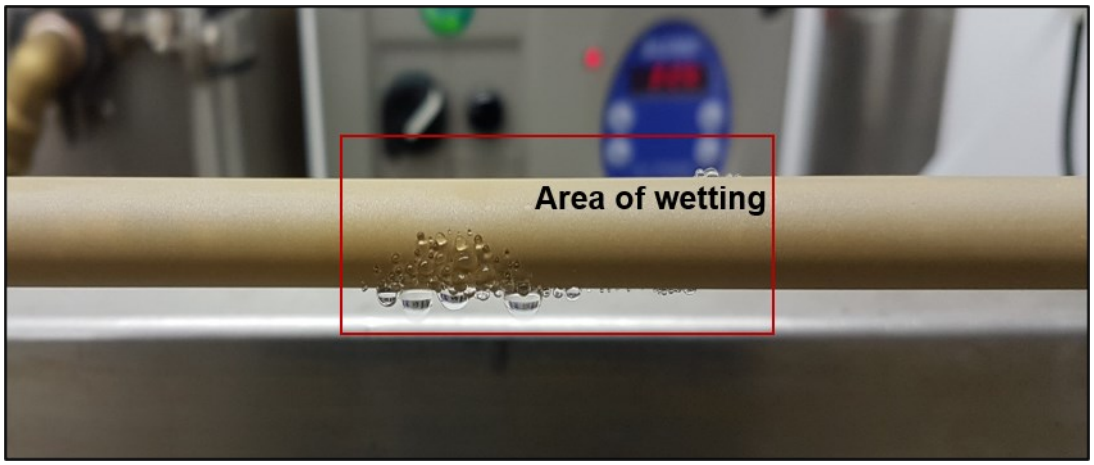

Figure 17: Wetted tubular TiO_2 membrane

The reference testing solution for LEP tests was demineralized water at room temperature. In addition, to evaluate the LEP based on the composition of the feed solution the following alternative solutions have been used:

- Demineralized water at 20 °C, 30 °C, 40 °C, 50 °C, 60 °C, 70 °C, 80 °C
- 1 g, 2 g, 5 g, 10 g, 20 g, 50 g, 100 g, 200 g, 300 g NaCl /kg H_2O
- 250 g sugar / kg H_2O (sugar: 99 wt.% D(+)-sucrose, Fluka US)
- 250 g ethanol / kg H_2O (ethanol: > 99.5 wt.%, Merck DE)

3.3 Direct Contact Membrane Distillation and Vacuum Membrane Distillation Tests

3.3.1 Experimental Set-Up and Testing Procedure

A lab-scale MD test bed containing two separate hydraulic loops made from polyvinyl chloride (PVC-C, plastic materials were required due to high loads of chlorides) was designed and constructed to enable DCMD (Figure 18) and VMD (Figure 19) operation. The feed was circulated by a centrifugal or peristaltic pump (Harton Anlagentechnik GmbH DE, model: Nemp 20/18 and Heidolph Instruments DE, model: Pumpdrive 5206) coming from a 4 L PVDF container. The coolant (only DCMD, demineralized water) was circulated by a centrifugal pump (Harton Anlagentechnik GmbH DE, model: Nemp 20/18) coming from a second 4 L PVDF container. The flow velocity was adjustable through a ball-valve (Thyssenkrupp AG DE, model: 163.543.211) and a by-pass in each loop and was monitored through an analog flow meter (GEMÜ Gebr. Müller

Apparatebau GmbH & Co. KG DE, model: Typ 873) made of PVDF. The feed-side was heated through a tube bundle heat exchanger made of PTFE (Polytetra GmbH DE, 0.14 m²) and through a circulation thermostat (Julabo GmbH DE model: F12) whereas the electric conductivity of the feed and coolant/permeate was monitored by sensors (feed: GHM Messtechnik GmbH DE, model: LF425; coolant/permeate: GHM Messtechnik GmbH DE, model: LF200) that were incorporated into the container and connected to a logging device (GHM Messtechnik GmbH DE, model: GMH 5450). Before and after the membrane module, temperature sensors (Pt100) were integrated into the pipes of the feed- and permeate-side and connected to another logging device (PCE Deutschland GmbH DE, model: PCE-T 390). The feed and permeate samples were collected via an outlet using 3-way ball-valves. The pipe system as well as the heat exchangers and container on the feed-side were thermally insulated (Armacell GmbH DE, model: AF 2 018-A). The membrane housing was made of PVC-C with an in- and outlet for the feed and the permeate/coolant side that could be sealed airtight if necessary.

In DCMD the hot feed was circulated through the membrane channel whereas the coolant was circulated counter flow wise along the outer side (permeate side) of the membrane. The permeate-side was cooled through a self-made stainless steel pipe bundle heat exchanger with an area of 0.066 m² and by a circulation chiller (VWR International US, model: 13271-218). The feed and coolant containers were placed on two laboratory balances (KERN AG DE, model: PBJ 8200-1M) to constantly monitor the respective masses and to determine permeate flux gravimetrically. The change of the mass of the coolant/permeate stream was obtained and recorded every two seconds by the respective balance. The conductivity of the feed and coolant/permeate as well as the temperatures at the inlet and outlet of the membrane module were recorded. Each DCMD test was run for at least 30 minutes. The testing time was extended up to several hours depending on the amount of permeate that was collected.

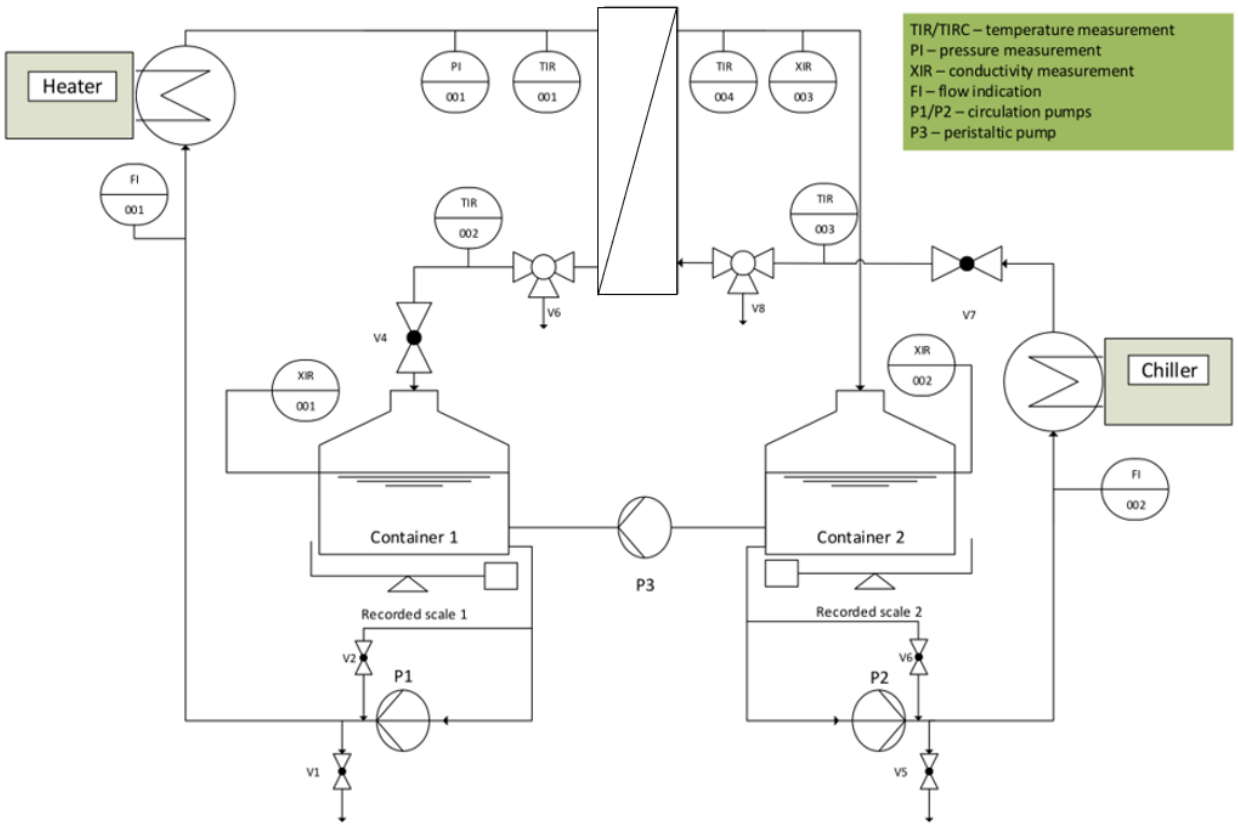

Figure 18: P&I Diagram of the DCMD test bed

In VMD only the temperature of the feed was monitored at the inlet and outlet of the membrane module. The absolute pressure on the permeate side was adjusted through a vacuum pump (KNF Neuberger GmbH, Laboport DE, model: N810.3) and a needle valve. The vapor was condensed in a cold trap outside of the membrane module through a refrigerated bath (VWR International US, model: 1190S). The permeate flux was determined by mass balancing. The permeate quality was determined by conductivity measurements. Each VMD test was run for a minimum of 15 minutes. The testing time was extended up to several hours depending on the amount of permeate that was collected.

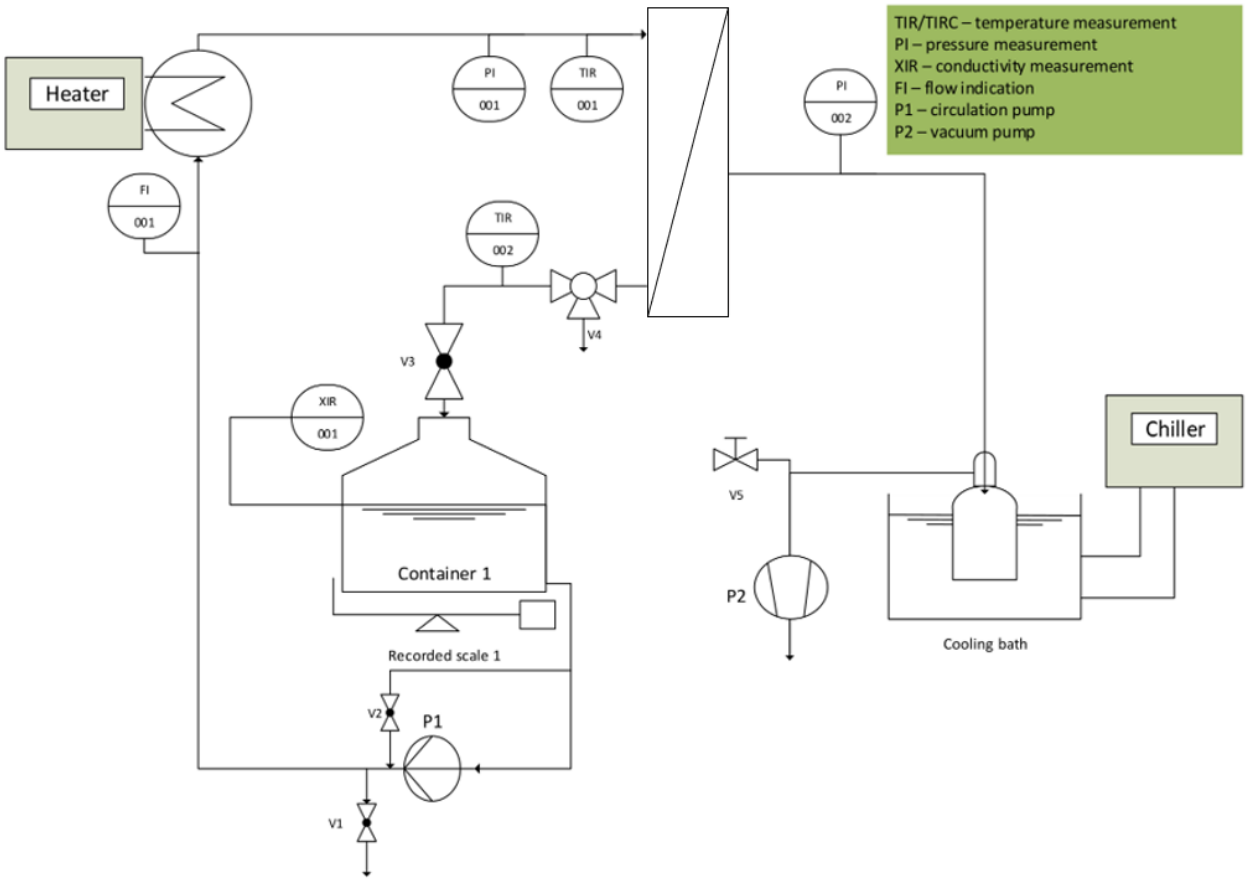

Figure 19: P&I Diagram of the VMD test bed

A minimum of three tests using a minimum of two different membranes of the same type were conducted for all investigations if not stated otherwise. The test results are shown as mean values with their confidence intervals (95 %, two-sided).

The rejection [-] was calculated based on the electric conductivity of the feed and permeate [µS/cm] as follows:

$$Rejection = 100 - \left(\frac{el.Conductivity_{Permeate}}{el.Conductivity_{Feed}}\right) * 100 \qquad (36)$$

The thermal efficiency of a single step VMD process based on the measures permeate fluxes and feed temperatures at the membrane module inlet and outlet was calculated based on Eq. 6 described in the theory section.

3.3.2 Operational Parameters and Feed Composition

To determine the impact of specific membrane properties the following operational parameters were kept constant in DCMD and VMD (Table 2).

Table 2: Standard operational parameters for DCMD and VMD tests

Process Parameters	DCMD	VMD
Feed Concentration	30 g NaCl / kg H_2O	30 g NaCl / kg H_2O
Feed Temperature	60 °C	60 °C
Coolant Temperature	20 °C	0 °C
Feed Flow Velocity	0.72 m/s	0.72 m/s
Coolant Flow Velocity	0.72 m/s	-
Absolute Pressure Permeate Side	-	100 mbar

Beyond the standard operational parameters defined in Table 3 the following range of parameters were investigated to determine the impact of operational parameters on the performance of ceramic membranes in VMD (Table 3).

Table 3: Process parameters investigated in VMD

Process Parameters	
Feed Concentration [g NaCl per kg H_2O]	90, 150, 270, 350
Feed Temperature [°C]	55, 65, 75
Coolant Temperature [°C]	0, 3, 15
Feed Flow Velocity [m/s]	0.14, 0.36, 1.08
Absolute Pressure Permeate Side [mbar]	75, 100, 125

In addition, VMD tests using the following real and recreated solution were conducted:

- **Recreated Salt Mining Wastewater** (provided by the K-UTEC AG Salt Technologies)**:** 38.48 g $MgSO_4$ + 284.50 g $MgCl_2$ + 69.98 g NaCl + 54.13 g KCl per kg H_2O

- **Real Food Processing Wastewater – RO Concentrate:** 3.5 wt.% TDS (containing salts such as: Na^+, Cl^-, K^+, Mg^{2+}, PO_4^{3-}) + 1 wt.% humic substances (not further specified by supplier)

3.4 Membrane Treatment to Determine Membrane Stability and Overview of Membrane Types Investigated

To evaluate the chemical, thermal and mechanical stability of modified ceramic single channel membranes, stability tests using hot saline solutions characterized by extreme pH values (Table 4) were conducted. The membranes were contacted with the aggressive solutions and subsequently characterized in respect of their LEP. The solution that is referred to as 'neutral' is in fact slightly acidic due to the dissolution of carbon dioxide from the atmosphere. This effect can be expected for all standard feed solutions open to the atmosphere. It was referred to as 'neutral' because no pH value affecting substance was added to the solution. The solution was chosen to be saline and hot cause this represents most of the MD environments in which membranes are typically used in.

Table 4: Composition of solutions that were used to test the stability of tubular ceramic membranes

Solutions		Composition	pH
Alkaline	Nr.1	50 g NaCl 50 g Na_2CO_3 per kg H_2O	12
	Nr.2	250 g NaCl + 50 g Na_2CO_3 per kg H_2O	12
Neutral	Nr.1	Demineralized Water	5
	Nr.2	250 g NaCl per kg H_2O	5
Acidic	Nr.1	50 g NaCl + 135 g HCl (37 wt.%) per kg H_2O	0
	Nr.2	250 g NaCl + 1 kg HCl (5 wt.%)	0

Three heat-resistant polypropylen (PP-H) tubes with sealed ends (diameter of 70 mm) were filled with the saline alkaline, (saline) neutral or saline acidic solution to a height of around 300 mm. The tubular membranes (length: 250 mm) were put vertically into the PP-H tube and submerged in the respective solution (Figure 20). The PP-H tubes were immersed into heating oil within a stainless steel pot with a height of 350 mm. Each of stainless-steel pots were placed on a heater (Heidolph

Instruments DE, model: MR Hei-standard). A spiral cold trap was connected to the top of the PVC tube to condense the vapor of the aggressive solutions and return inside the tube. The membranes were submerged in the solution inside the pot. The mixture was then heated up to ~100 °C. The membranes were kept submerged in the hot solution for 96 hours. The temperature of the solution was monitored by a temperature sensor (Heidolph Instruments DE, model: EKT Hei-Com). After the treatment, the membranes were cleaned with pure water and dried at 120 °C for two hours.

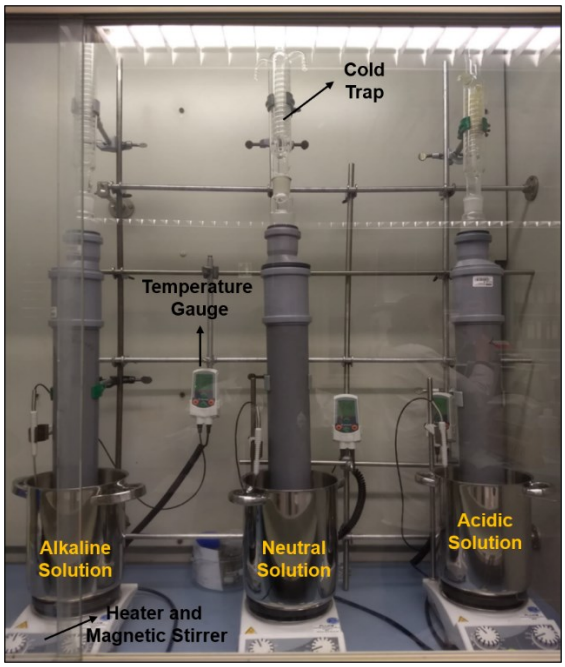

Figure 20: Test Rig to cook modified single channel membranes (length: 250 mm) in either a saline alkaline, neutral or saline acidic solution for 96 hours

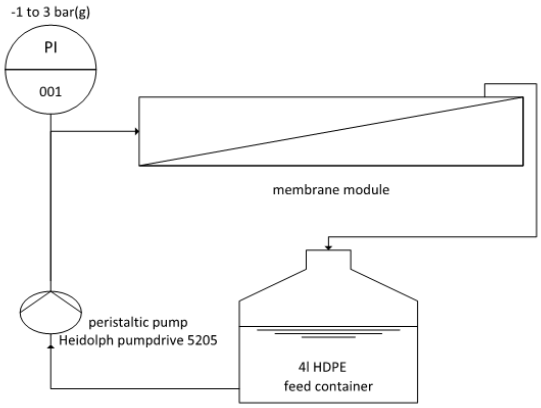

Figure 21: P&I Diagramm of the abrasion test bed

To evaluate the resistance towards highly abrasive solutions a highly saline solution (artificially recreated potassium mining waste water defined in chapter 3.3.2) was circulated (1.2 L) through the lumen of tubular ceramic membranes (pump: Heidolph pumpdrive 520S) at atmospheric pressure and ambient temperature for 7 h and 56 h at a feed flow rate of 0.72 m/s (Figure 21). Based on the composition and the temperature (20 °C to 30 °C) of the saline solution, the solution was at the saturation point (with NaCl crystallizing at first) when utilized for the test.

The subsequent Table 5 lists all membrane types that were investigated for this work as well as the respective tests done on a specific membrane type.

Table 5: Specifications of tubular membrane systems that were studied within the scope of this work (δ is the support wall thickness, ε is the open porosity of the support, d_p is the average pore size, Molecule label is the internal reference to a specific surface modification agent and ω is the mass concentration of the applied modification agent

Support				**Intermediate layer(s)**				**Final layer**				**Modification**		Tests conducted	Min number of membranes available
Material	δ [mm]	d_p [µm]	ε [-]	Material	d_p [µm]	δ [µm]	ε [-]	Material	d_p [nm]	δ [µm]	ε [-]	Molecule-label	ω [wt.%]		
Al_2O_3	1.5	3.6	0.33	Al_2O_3	0.8/0.2	17.5/17	0.38/0.42	Al_2O_3	100	16.5	0.43	HOC	1	A,C,D	3
Al_2O_3	1.0	3.6	0.33	Al_2O_3	0.8/0.2	17.5/17	0.38/0.42	Al_2O_3	100	16.5	0.43	HOC	1	D,E	3
Al_2O_3	1.5	3.6	0.33	Al_2O_3	0.8	17.5	0.38	Al_2O_3	200	16.5	0.42	HOC	1	B,F	3
Al_2O_3	1.5	3.6	0.33	Al_2O_3	0.8	17.5	0.38	Al_2O_3	200	16.5	0.42	HOG	1	B,F	3
Al_2O_3	1.5	3.6	0.33	Al_2O_3	0.8	17.5	0.38	Al_2O_3	400	33	0.44			C	3
Al_2O_3	1.5	3.6	0.33	Al_2O_3	0.8	17.5	0.38	Al_2O_3	400	33	0.44	HOC	1	B,D,F	3
Al_2O_3	1.5	3.6	0.33	Al_2O_3	0.8	17.5	0.38	Al_2O_3	400	33	0.44	HOG	1	B,F	3
Al_2O_3	1.5	3.6	0.33	Al_2O_3	0.8	17.5	0.38	Al_2O_3	400	33	0.44	HOC	2	B,E,F	3
Al_2O_3	1.5	3.6	0.33	Al_2O_3	0.8	17.5	0.38	Al_2O_3	400	33	0.44	HOM	2	B,E,F	3
Al_2O_3	1.6	0.54	0.31	Symmetric Membrane (no intermediate and final layers)										C	3
Al_2O_3	0.8	0.54	0.32	Symmetric Membrane (no intermediate and final layers)										C	3
Al_2O_3	1.6	0.54	0.31	Symmetric Membrane (no intermediate and final layers)								HOC	2	B,E,F	3
Al_2O_3	0.8	0.54	0.32	Symmetric Membrane (no intermediate and final layers)								HOC	2	E,F	3
Al_2O_3	1.6	0.54	0.31	Symmetric Membrane (no intermediate and final layers)								HOM	2	B,E,F	3
Al_2O_3	0.8	0.54	0.32	Symmetric Membrane (no intermediate and final layers)								HOM	2	E,F	3
TiO_2	1.5	4.6	0.33	TiO_2	0.8/0.25	30/20	0.28/0.31	TiO_2	100	15	0.43	HOC	1	A,B,C,D,G	3
TiO_2	1.0	4.6	0.33	TiO_2	0.8/0.25	30/20	0.28/0.31	TiO_2	100	15	0.43	HOC	1	D,E	3
TiO_2	1.5	4.6	0.33	TiO_2	0.8/0.25	30/20	0.28/0.31	TiO_2	250	20	0.31	HOC	1	B,F,G	3
TiO_2	1.5	4.6	0.33	TiO_2	0.8/0.25	30/20	0.28/0.31	TiO_2	250	20	0.31	HOG	1	B,F	3
TiO_2	1.5	4.6	0.33	TiO_2	0.8	30	0.28	TiO_2	400	30	0.37	HOC	1	B,D,F,G	3
TiO_2	1.0	4.6	0.33	TiO_2	0.8	30	0.28	TiO_2	400	30	0.37	HOC	1	D,E	3
TiO_2	1.5	4.6	0.33	TiO_2	0.8	30	0.28	TiO_2	400	30	0.37	HOG	1	B,F	3
TiO_2	1.5	4.6	0.33	TiO_2	0.8	30	0.28	-				HOC	1	B	3
TiO_2	1.5	4.6	0.33	TiO_2	0.8	30	0.28	TiO_2	200	40	0.31			C	3
TiO_2	1.5	4.6	0.33	TiO_2	0.8	30	0.28	TiO_2	200	40	0.31	HOC	2	B,E,F	3
TiO_2	1.5	4.6	0.33	TiO_2	0.8	30	0.28	TiO_2	200	40	0.31	HOM	2	B,E,F	3

Support				Intermediate layer(s)				Final layer				Modification		Tests conducted	Min. number of membranes available
Material	δ [mm]	d_p [µm]	ε [-]	Material	d_p [µm]	δ [µm]	ε [-]	Material	d_p [nm]	δ [µm]	ε [-]	Molecule-label	ω [wt.%]		
TiO_2	1.6	0.33	0.31	Symmetric Membrane (no intermediate and final layers)										C	3
TiO_2	0.8	0.20	0.33	Symmetric Membrane (no intermediate and final layers)										C	3
TiO_2	1.6	0.33	0.31	Symmetric Membrane (no intermediate and final layers)								HOC	2	B,E,F	3
TiO_2	0.8	0.20	0.33	Symmetric Membrane (no intermediate and final layers)								HOC	2	E,F	3
TiO_2	1.6	0.33	0.31	Symmetric Membrane (no intermediate and final layers)								HOM	2	B,E,F	3
TiO_2	0.8	0.20	0.33	Symmetric Membrane (no intermediate and final layers)								HOM	2	E,F	3
Mixed Oxides	1.5	1.0	0.46	Al_2O_3	0.2	33	0.42	Al_2O_3	100	16.5	0.43	HOC	1	C,D	3
Mixed Oxides	1.5	1.0	0.46	-				Al_2O_3	400	49.5	0.44	HOC	1	D	3
Mixed Oxides	1.5	1.0	0.46	-				-				HOC	1	A	3
Mixed Oxides	1.5	1.0	0.46	Al_2O_3	0.2	33	0.42	ZrO_2	110	16.5	0.52	HOC	1	C,D	3
Mixed Oxides	1.5	1.0	0.46	TiO_2	0.8/0.25	30/20	0.28/0.31	TiO_2	100	15	0.43	HOC	1	C,D	3
Mixed Oxides	1.5	1.0	0.46	-				TiO_2	400	45	0.37	HOC	1	D	3
Mixed Oxides	1.5	1.0	0.46	TiO_2	0.4	30	0.37	ZrO_2	110	33	0.52	HOC	1	C,D	3
Cordierite	1.5	0.9	0.36	Al_2O_3	0.2	33	0.42	Al_2O_3	100	16.5	0.43	HOC	1	A,C,D	3
Cordierite	1.5	0.9	0.36	Al_2O_3	0.4	33	0.44	Al_2O_3	400	16.5	0.44	HOC	1	D	3

A = Thermal Conductivity: Experimental procedure: chapter 3.2.3, results: chapter 4.1.1

B = Liquid Entry Pressures: Experimental procedure: chapter 3.2.5, results: chapter 4.1.3

C = Steady State Gas Permeance: Experimental procedure: chapter 3.2.2, results: chapter 4.1.44.1.1

D = DCMD: Experimental procedure: chapter 3.3.1, results: chapter 4.2.1 and 4.2.3

E = VMD: Experimental procedure: chapter 3.3.1, results: chapter 4.2.2, 4.2.3, 4.2.4, 4.3

F = Stability Tests: Experimental procedure: chapter 3.4, results: chapter 4.2.5

G = VMD Modelling: Experimental procedure: chapter 3.5, results: chapter 4.4

3.5 Mass Transfer Modelling

The mass transfer modelling was limited to the VMD configuration. This is because the conditions under which the mass and heat transfer takes place in DCMD could not be specifically defined. For instance, it is not known how strongly different supports infiltrate with coolant liquid during operation affecting the heat transfer and diffusion distances. The mass transfer was calculated using a generally accepted VMD model based on the DGM and semi-empirical relationships that are described in more detail in chapter 2.5. The follow Figure 22 gives an overview of the modelling approach.

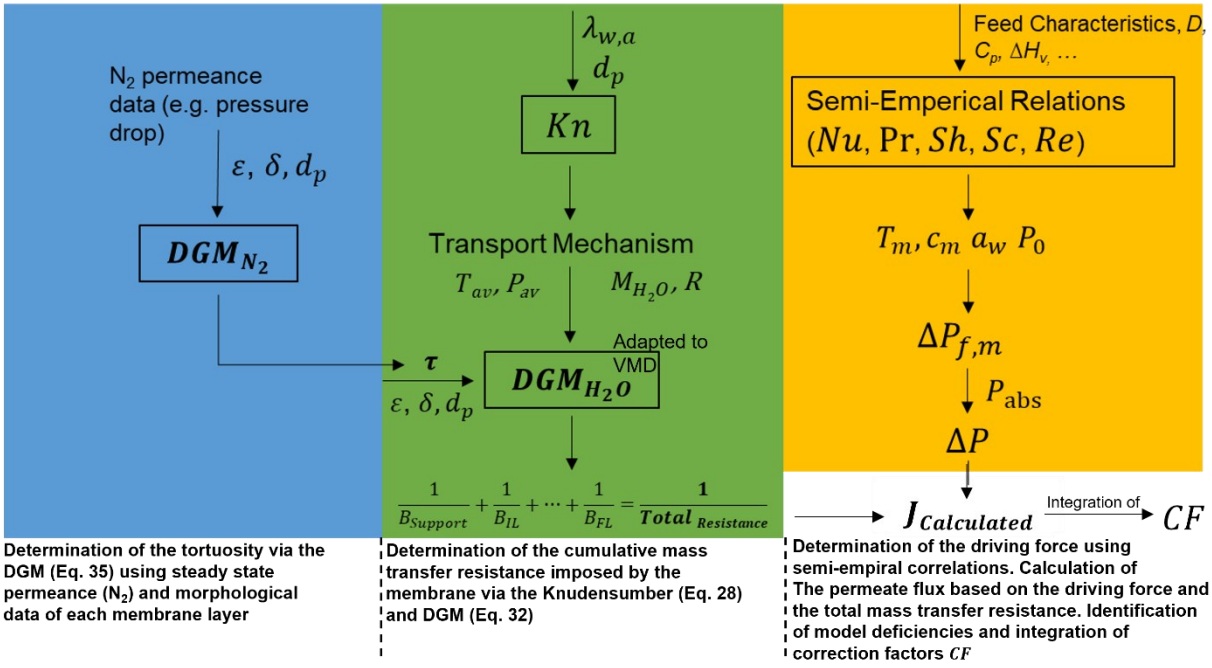

Figure 22: Schematic representation of the modelling approach

N_2 permeance data and known morphological data (e.g. pore size and layer thickness) were used to calculate the tortuosity of each membrane layer using the DGM in the following form [89,146,152,180] (blue background in Figure 22):

$$\tau = \left(\frac{2\varepsilon r}{3} + \frac{\varepsilon r^2 p_{av}}{8\eta_N \bar{v}}\right)\frac{\bar{v}\Delta p}{JRT\delta} \tag{37}$$

With η_N as the dynamic viscosity of nitrogen [Pa s], $\bar{v}$ as the molecular velocity of nitrogen ($\sqrt{\frac{8RT}{\pi M_{N2}}}$) [m/s] and M_N as the molecular weight of nitrogen [kg/mol]. The full set of morphological data was then fed into the modified DGM (Eq. 33, super-position of Knudsen diffusion and viscous flow as determined via the Knudsen number). The average temperature was assumed to be constant across the membrane because the relatively high thermal conductivity of the membrane makes it serve as a heat exchanger compensating for the heat loss of the vapor due to the pressure drop. The average pressure inside the pores for each membrane layer was approximated iteratively using the DGM as well as the following relation:

$$p_{av} = \frac{\Delta p}{2} + p_{Inlet} \tag{38}$$

Semi-empirical relations described in chapter 2.5.1 as well as measured data on the permeate flux were used to approximate temperature and concentration polarization for each data point. The consideration of concentration polarization was limited to the saturation point at the respective feed temperature. This data was then used to determine the partial vapor pressure at the membrane interface and subsequently the actual driving force in consideration of the absolute pressure applied to the permeate side (yellow background in Figure 22). The mass transfer resistance was calculated using the modified DGM for each separate layer and combined in series to determine the overall mass transfer resistance (green background in Figure 22). Using the overall mass transfer resistance and the actual driving force the vapor flux could be calculated. Based on the agreement between calculated and measured permeate fluxes model deficiencies were identified and corrections factors integrated accordingly. This approach was used to calculate the vapor flux in respect to the feed temperature and flow velocity in variation of the pore size and feed concentration. All calculations were based on the mathematical correlations introduced in chapter 2.5.1 and chapter 2.5.2 as well as fitting functions listed in Table 6.

Table 6: Mathematical correlations and fit function used to determine the viscosity of the feed (η_{Feed}), heat capacity of the feed (C_P), thermal conductivity of the feed (k_f) and the permeate flux (J) for the VMD mass transfer modelling (if unspecified the concentration refers to the total mass of the mixture)

Parameter		Model as Function of **Temperature**	**Ref.**
η_{Feed}	[Pa s]	**Feed: 30 g NaCl/kg H_2O:** $(0.1139T^2 - 21.185T + 1351.9) \cdot 10^{-6}$, R^2=0.9996, T in °C, c_{NaCl} = 0.5 mol/kg	[181]
		Feed: 350 g NaCl/kg H_2O: $(0.2119T^2 - 39.473T + 2526.6)10^{-6}$, R^2=0.9996, T in °C, c_{NaCl} = 4.43 mol/kg	
C_P	[J/K]	**Feed: 30 g NaCl/kg H_2O:** $0.0043T^2 - 0.0508T + 4035.9$, R^2=0.9994, T in °C	[182]
		Feed: 350 g NaCl/kg H_2O: $-0.0052T^2 + 0.1352T + 3276.6$, R^2=0.9974, T in °C	
k_f	[W (m K)]	**Feed: 30 g NaCl/kg H_2O:** $(-0.0091T^2 + 7.115T - 708.69)\ 10^{-3}$, R^2=0.9989, T in K, c = 26 g NaCl/kg H_2O	[183]
		Feed: 350 g NaCl/kg H_2O: $(-0.0093\mathrm{T}^2 + 7.2351\mathrm{T} - 751.96) \cdot 10^{-3}$, R^2=0.9975, T in K, c = 312 g NaCl/kg H_2O	
J	[kg/(m² h)]	**100nm, 150 L/h**: $0.0355T^2 - 3.1T + 67.313$, R^2=1, T in °C	
		100nm, 50 L/h: $0.0205T^2 - 12.809T + 1999{,}7$, R^2=1, T in K	
		100nm, 20 L/h: $-0.0078T^2 + 1.63T - 64.197$, R^2=1, T in C	
		400nm, 100 L/h: $0.0128T^2 + 0.2618T - 41.797$, R^2=0.9939, T in C	

4 Results and Discussion

The result section presents and discusses data on membrane characteristics (i.e. pore size, thermal conductivity, layer composition, layer thickness, permeance, hydrophobicity and stability) of ceramic (MD) membranes and evaluates the impact of those properties on the performance in DCMD and VMD configuration. In addition, the VMD performance is evaluated in respect to relevant process parameters such as the feed composition, feed temperature and flow velocity and the absolute pressure on the permeate side using synthetic saline and real solutions. The data presented and discussed on membrane properties as well as the performance data of ceramic membranes in DCMD and VMD is used to validate and improve a VMD model proposed by the literature (based on the DGM) and provide stimulus for membrane adaptation and optimization. Moreover, the performance data is used to assess the strength and limitation of ceramic membranes and to identify suitable areas of application.

4.1 Characterization of Ceramic Membrane Properties

The viability of a MD process is highly dependent on the membranes utilized within the process. The membrane facilitates the selective extraction of volatile components such as water vapor from an aqueous solution via diffusion in respect to its specific characteristics but also defines the extent of the mass transfer resistance towards the transported molecules. Therefore, it is imperative to understand the structure and properties of ceramic membranes in detail. This allows the evaluation of the impact of relevant membrane properties on the MD performance (permeate flux, selectivity, stability and heat transfer) of ceramic membranes. The results presented in this section are based on investigations that provided data that complements data derived via standard characterization methods (e.g. pore size and porosity) but was required to correlate membrane performance with membrane properties beyond pore size and porosity (thermal conductivity, permeance and hydrophobic characteristics). For instance, knowledge on the thermal conductivity of ceramic membranes was needed to understand the permeate flux and energy efficiency of ceramic membranes in respect to temperatures polarization while steady state gas permeation tests were required to evaluate the permeate flux in respect to the layer design of the membranes.

4.1.1 Thermal conductivity

The thermal conductivity of a membrane is governed by the thermal conductivity of the membrane material and the porosity of the membrane due to the void fraction that serves as a thermal insulation. High thermal conductivities lead to an increased heat transfer (and heat loss) via heat conduction which in return cause more pronounced temperature polarization effects resulting in the reduction of the driving force. Therefore, the thermal conductivity is a membrane parameter that strongly affects the energetic efficiency of MD processes. This effect is predominantly observed in DCMD since the permeate side of the membrane system is in direct contact with the cooling liquid. In VMD, the effect of the thermal conductivity is relatively small since there is no fluid on the permeate side to absorb heat from the feed. The heat that is transferred is mainly latent heat transported by the vapor flux. Figure 23 illustrates the measured thermal conductivity of several tubular ceramic supports (different materials) as well as the same support types with added membrane layers and surface modification.

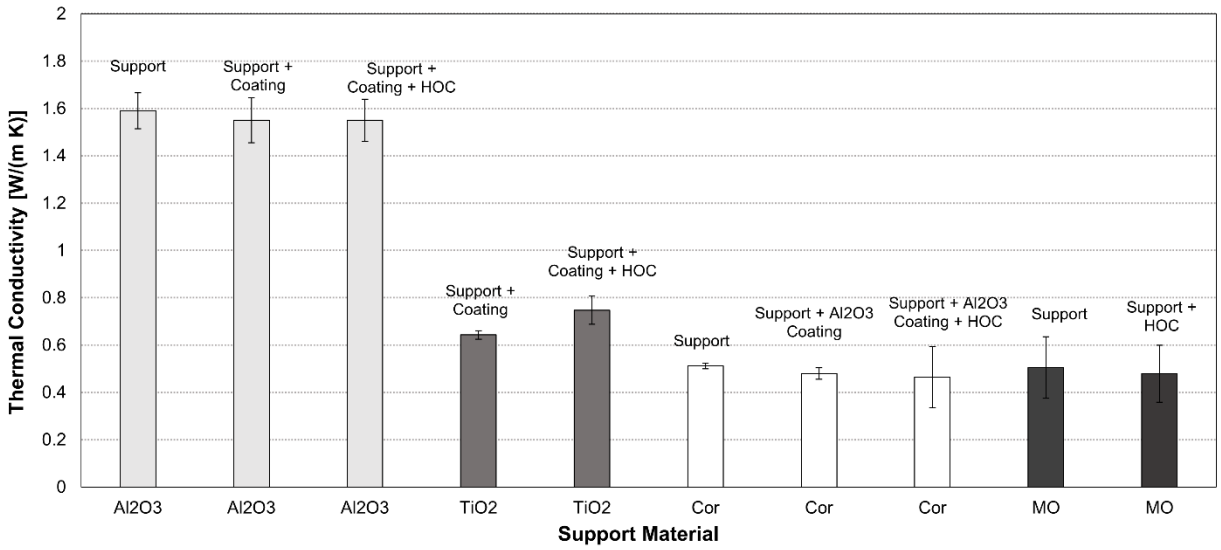

Figure 23: Thermal conductivity of different membranes made of Al_2O_3 (coated with Al_2O_3 layers), TiO_2 (coated with TiO_2), cordierite (Cor) and mixed oxide (MO), In case of Membrane Coating: final pore size = 100 nm, HOC refers to the hydrophobic agent as defined in chapter 3.1, 5 tests, the error bars depict the confidence intervals of the average value

Al_2O_3 membranes exhibited the highest thermal conductivity with values between 1.5 W/(m K) to 1.6 W/(m K) followed by the TiO_2 membranes that showed thermal conductivities in the range of 0.6 W/(m K) to 0.8 W/(m K) The cordierite and mixed oxide membranes showed the lowest thermal conductivities in the range of 0.5 W/(m K). This observation can be attributed to the

different thermal conductivities of the materials (Al_2O_3 15 W/(m k) to 30 W/(m K), TiO_2: 1.5 W/(m k) to 5 W/(m k) and cordierite material: 1.2 W/(m K) to 2.5 W/(m K) [119]) as well as the different porosities of the membrane supports (Table 5, Al_2O_3: 33 %, TiO_2: 33 %, cordierite: 36 % and mixed oxide: 46 %). The coating or grafting process did not impact the thermal conductivity of any membrane types significantly even if the membrane layers were made from a different material than the support (cordierite support vs cordierite support + Al_2O_3 layers). It can be stated that the support properties define the thermal conductivity of ceramic asymmetric single channel membranes. This is because the support thickness is more than 10-times greater than the thickness of all membrane layers combined. The thermal conductivity of a membrane is governed by the thermal conductivity of the ceramic material and the gas phase (usually air) within the membranes pores and can be predicted for polymeric membranes using models in regard to the thermal conductivity of the material and the porosity of the membrane [95]. Unfortunately, these models do not account for the microstructure of ceramic membranes (e.g. grain sintering, grain growth and pore formation) which can vary significantly in dependence on the wall thickness of the membrane and the sinter regime. Therefore, these models do not adequately predict the thermal conductivity of ceramic membranes. This is also the reason why the thermal conductivities of TiO_2 and Al_2O_3 membranes (similar porosities) do not differ as strongly as could be expected if the highly different thermal conductivities of the membrane materials are considered (factor 2.5 vs factor of 3 to 20). Even though the thermal conductivity values reported for cordierite and mixed oxides membranes are significantly lower than the thermal conductivity of Al_2O_3 membranes they are still significantly higher (by a factor > 10) than the thermal conductivity of hydrophobic polymeric membranes such as PTFE, PVDF and PP with values from 0.027 W/(m K) to 0.041 W/(m K) [17].

4.1.2 Contact Angle Measurements

CA measurements on hydrophobized Al_2O_3 flat sheet membranes at ambient conditions were done. Based on the extent of the CA (CA > 90° or CA < 90°) alternative potentially suitable hydrophobic agents for the modification of tubular ceramic membranes were identified. The CA measurements on Al_2O_3 flat sheet membranes modified with HOC and HOG were taken as a reference. The results are displayed in Figure 24.

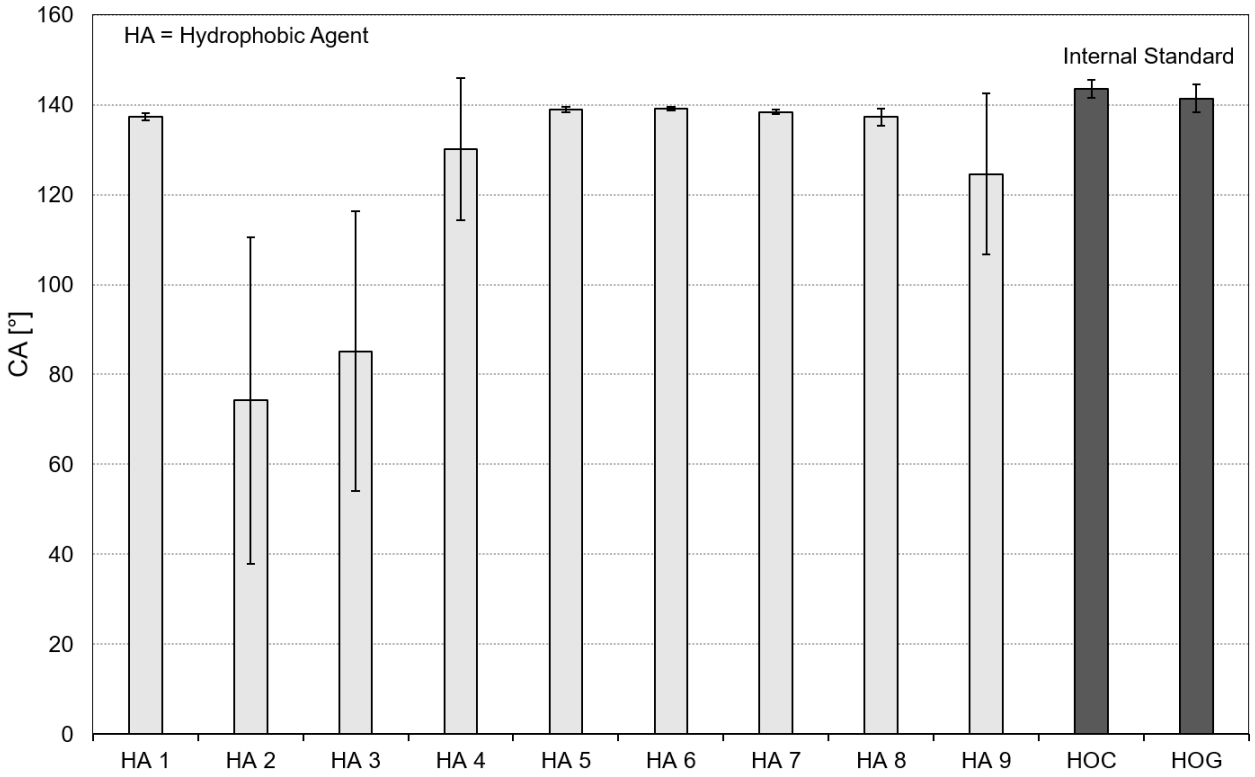

Figure 24: Contact angle measurements of Al_2O_3 flat sheet membranes (final pore size: 200 nm) modified with 11 different hydrophobic agents (HA: Hydrophobic Agent (1 wt.%), HOC/HOG: internal standard, testing solution: pure water at room temperature, minimum of 4 tests, the error bars depict the confidence intervals of the respective average value

As can be seen in Figure 24, all hydrophobic agents but HA 2 and HA 3 (non-conclusive results due to high error margins) resulted in CAs greater than 90°. This indicates that the chemical modification using the hydrophobic agents (H1 and H4 to H9) resulted in a significant lowering of the free surface energy of the Al_2O_3 flat sheet membranes. It can also be stated that the CAs of the Al_2O_3 flat sheet membranes modified with H1 and H5 to H8 show very little error margins and lie in the same range as CAs measured for Al_2O_3 flat sheet membranes modified with the reference agents HOC and HOG (~ 140 °). Because the CA does not consider the heterogeneity of the membrane surfaces it only serves as a first indicator of the extent of the hydrophobicity of modified porous ceramic membrane. Consequently, it could be concluded that samples with a CA below 90° were not hydrophobic (HA 2 and HA 3) and were excluded from further tests. It also means that samples with a CA above 90 °C were not necessarily hydrophobic since the heterogeneity of their surface is not considered. The contact angle hysteresis CAH is an additional CA based indicator (= difference between advancing and receding CA) that is more suited to characterize the hydrophobicity of a heterogeneity membrane surface (e.g. caused by membranes pores). Based on the results illustrated the above, the advancing and receding CA as well as the

respective CAH of those modified Al_2O_3 flat sheet membranes (all but H2 and H3) were determined that exhibited CAs over 90 °C (Figure 25).

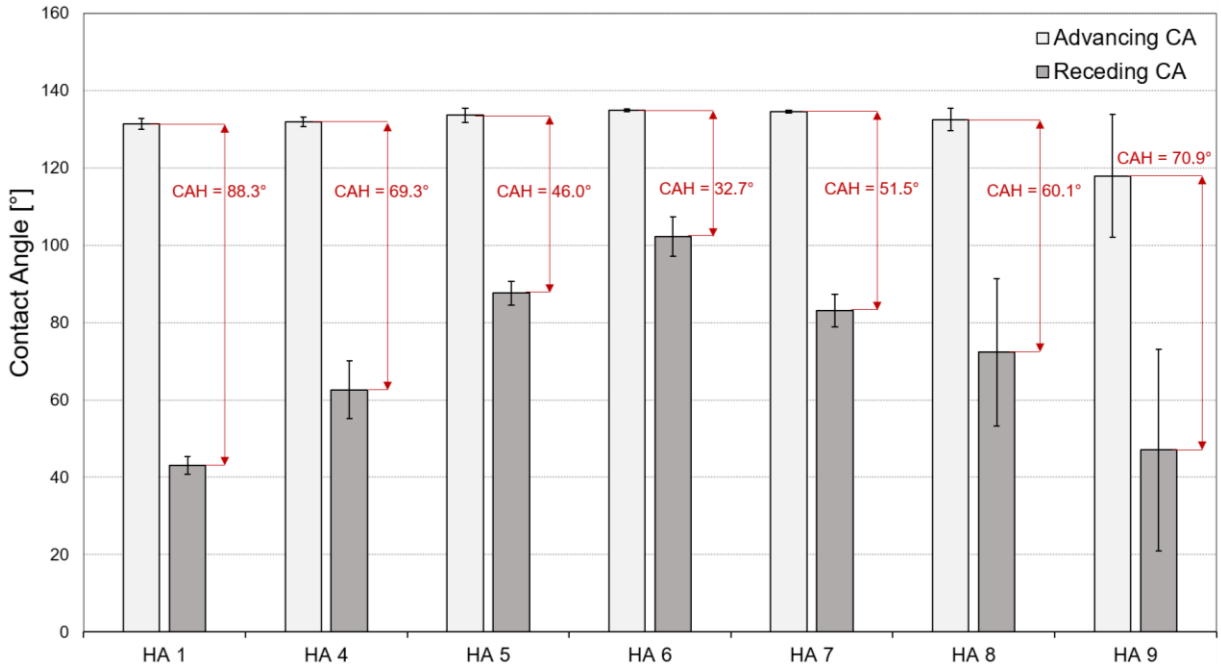

Figure 25: Contact angle hysteresis of Al_2O_3 flat sheet membranes modified with 7 different hydrophobic agents (light grey bars: advancing CA, dark grey bars: receding CA and hysteresis CAH, testing solution: pure water at room temperature, minimum of 4 tests, the error bars depict the confidence intervals of the respective average value

On a heterogenic or rough surface (the surface of a modified ceramic membranes is heterogenic) the receding CA is expected to be smaller than the static or advancing CA. Therefore, the smaller the difference (CAH) between the receding CA and the advancing CA on a modified ceramic membrane surface (if both CA are considerably higher than 90°) the more pronounced the hydrophobic characteristics of the membrane surface. Whereas the advancing CAs were measured in the range of 118 ° and 135 ° the receding CAs were determined to be below 90° (except for HA 6) resulting in high CAHs. Since HA 6 is the only sample that exhibited both advancing and receding CAs above 90° (resulting in a relatively small CAH) it represents the membrane sample modified with the most promising hydrophobic agent. Based on these results, HA 6 (referred to as 'HOM', non-fluorinated, described in chapter 3.1) was then chosen to serve as an additional non-fluorinated hydrophobic agent (beside the standard hydrophobic molecules HOC and HOG) to modify selected ceramic single channel tubes to enable further investigations.

4.1.3 Liquid Entry Pressure – Impact of Pore Size, Feed Characteristics and Surface Modification

The LEP serves as a practical parameter to define the extent of the hydrophobic characteristics of membranes and is more suitable than the CA as an indicator if specific process conditions allow the application of a certain membrane type in MD processes. As mentioned before the literature recommends a LEP of 2.5 bar or higher for membranes to be utilized in MD processes [86]. Besides the feed characteristics and membrane properties (pore size), the modification agent and the grafting methodology (e. g. time, concentration) define the extent of the LEP of functionalized ceramic membranes. The literature suggested that the ideal concentration for the modification of asymmetrically structured single channel ceramic membranes (TiO_2) modified by PFAS is 1 wt.% [129]. For this study, a selection of symmetrically structured and asymmetrically structured ceramic membranes was modified using 1 wt.% of HOC and 1 wt.% of HOG (asymmetric Al_2O_3 and TiO_2 membranes) as well 2 wt.% of HOC and 2 % of HOM (symmetric and asymmetric Al_2O_3 and TiO_2 membranes). Since the modification of the symmetric membranes is not limited to a thin active membrane layer (the whole cross section of the membrane defines the selectivity) the higher concentration of 2 wt.% was chosen. To ensure the comparability between the two membrane types the asymmetrically structured ceramic membranes were modified with 2 wt.% of HOC and 2 wt.% HOM as well. HOC and HOG were chosen as hydrophobic agents because they were used successfully to modify hydrophilic ceramic membranes prior to this work. However, despite being used frequently for the modification of ceramic membranes, the dependency of the hydrophobic extent (induced by HOC and HOG) has not been studied in respect to membrane and feed solution characteristics. HOM was chosen as a non-fluorinated alternative based on promising CA data presented in chapter 4.1.2. In order to obtain a general understanding of the modification efficiency in respect to the selected hydrophobic agents, the LEP was determined in respect to the type and concentration of the hydrophobic agent as well as the membrane pore size (Figure 26).

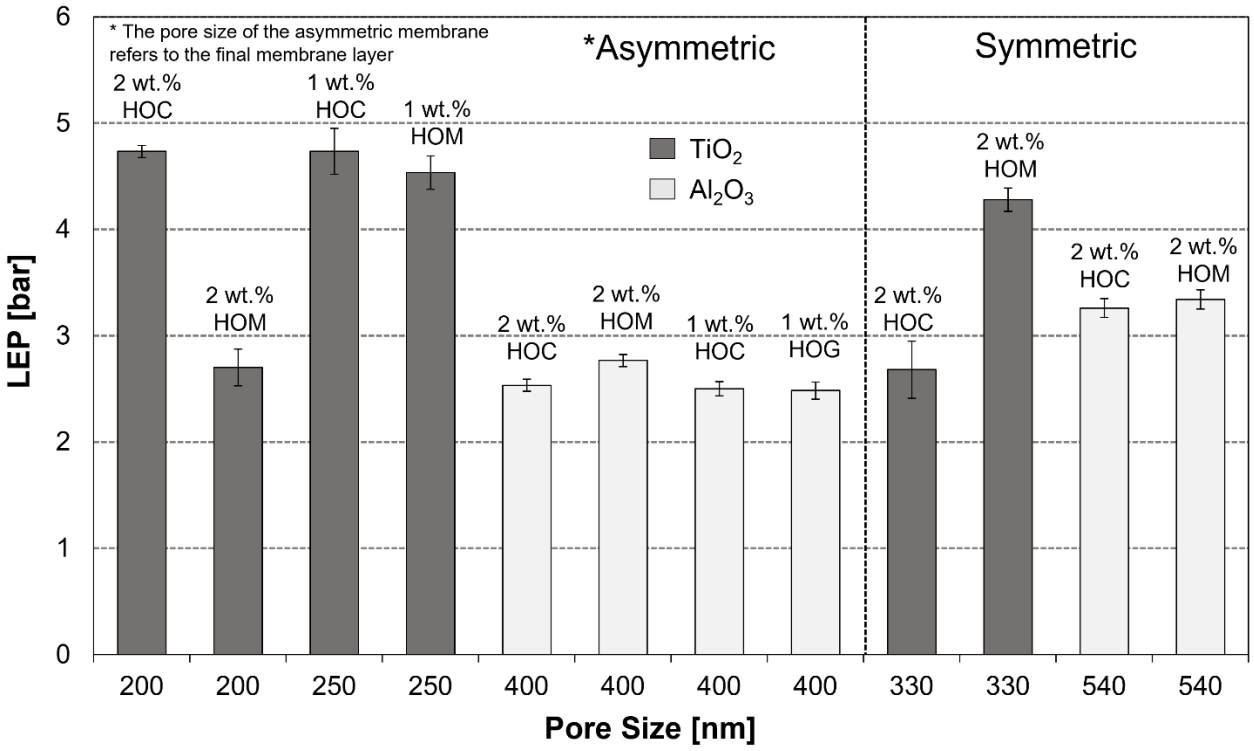

Figure 26: LEP in dependence of the material (light grey: Al_2O_3, dark gray: TiO_2), layer structure (symmetric and asymmetric), pore size (asymmetric membranes: final membrane layer, symmetric membranes: same pore size over the whole cross section of the membrane) and the type and concentration of the hydrophobic agent (HOC and HOM), minimum of 4 tests, the error bars depict the confidence intervals of the respective average value

All modified membranes exhibited LEPs above 2.5 bar fulfilling the minimum requirement (suggested by the literature) to be utilized in MD processes. The symmetric Al_2O_3 membranes showed higher LEPs than the asymmetrical Al_2O_3 membrane modified with the same hydrophobic agents despite their larger pores (0.54 µm vs 0.4 µm). The symmetrical TiO_2 membranes exhibited lower LEP than the asymmetrical TiO_2 membranes if modified with HOC. This behavior is in accordance with the pore size of the asymmetric and symmetric TiO_2 membranes (0.33 µm vs 0.2 µm). In contrast, TiO_2 membranes modified with HOM showed the same effect as the Al_2O_3 membranes exhibiting a considerably higher LEP for symmetric membranes than asymmetric membranes despite the larger pores.

It can be stated that using 2 wt.% instead if 1 wt.% HOC did not increase the LEP of asymmetric Al_2O_3 or TiO_2 membranes significantly. This is in accordance with the study of Schnittger et al. 2019 [129] that showed no significant increase of the LEP with the increase of the PFAS concentration from 1 wt.% to 2 wt.% for asymmetrical TiO_2 membranes with a pore size of 250 nm. The use of 2 wt.% HOM (non-fluorinated) instead of 2 wt.% HOC (fluorinated) resulted in a slightly increased LEP for asymmetrical Al_2O_3 membranes and a strongly reduced LEP (43 %) for

asymmetric TiO_2 membranes. Except for the asymmetric Al_2O_3 membrane modified with 2 wt.% HOM, the type of the hydrophobic agent (non-fluorinated: HOC & HOG vs fluorinated) as well as the concentration did not affect the LEP of asymmetrical Al_2O_3 membranes significantly. The modification of asymmetrical TiO_2 membranes using the hydrophobic agent HOM resulted in a considerably reduced LEP whereas the use of HOC as the hydrophobic agent (fluorinated agents as defined in chapter 3.1) did not lead to significant differences in the LEP.

The LEP of symmetric Al_2O_3 membranes was not significantly affected by choice of modification agent (non-fluorinated vs fluorinated) whereas the use of HOM led to 60 % higher LEP of symmetric TiO_2 membranes in comparison with membranes modified with HOC. As described in chapter 2.2.1 the LEP is highly affected by the feed characteristics such as feed temperature, salinity and the presence of surface-active substances. Although the LEP model (Eq. 2) derived by Franken et al. 1987 [73] does not consider the feed characteristics directly, these parameters affect the liquid-solid contact angle and the liquid surface tension significantly which are an integral part of the model [89]. To determine the impact of the aforementioned factors on the LEP of modified tubular ceramic membranes, single channel TiO_2 tubes exhibiting a pore size between 100 nm and 800 nm were modified using 1 wt.% HOC and characterized regarding the LEP using feed solutions with different properties. Figure 27 shows the LEP in respect to the pore size and the temperature of the testing solution.

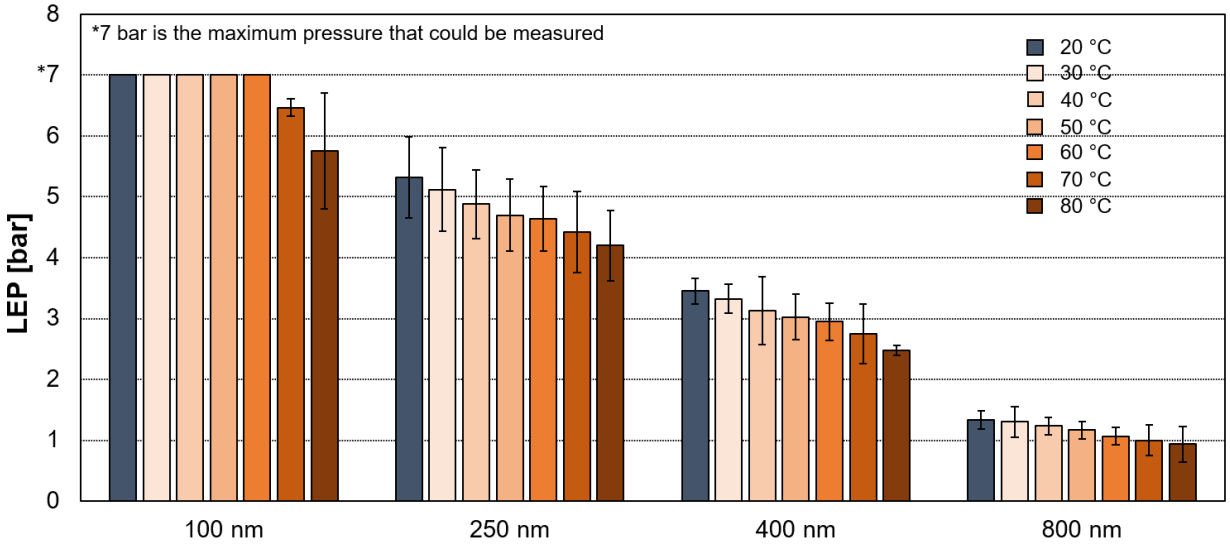

Figure 27: LEP in dependence of the pore size (final membrane layer) and testing solution temperature, the maximum LEP that could be measured was 7 bar (membrane: TiO_2 modified with 1 wt.% HOC, testing solution: pure water, 3 to 6 tests were conducted on separate membranes for each temperature), the error bars depict the confidence intervals of the respective average value

The highest LEP of 7 bar and above (7 bar is the LEP test rig limitation) was determined for membranes with an average pore size of 100 nm and for test solution temperatures ranging from 20 °C to 60 °C. The LEP showed a decline with increasing membrane pore size to around 1 bar for a pore size of 800 nm. This observation is in accordance with the LEP model (Eq. 1) derived by Franken et al. 1987 [73] suggesting an inversely proportional relationship between the maximum membrane pore size and the LEP. Moreover, the LEP decreased with increasing test solution temperatures for all membrane pore sizes. Higher temperatures lead to the water molecules gaining kinetic energy causing a reduction of the intermolecular forces which subsequently lowers the surface tension. This effect is also represented in the LEP model since it considers the liquid surface tension directly and indirectly (via the liquid-solid contact angle). The near linear dependency between the surface tension of pure water and temperature is also reported in the literature [184]. The effect of the pore size on the LEP was considerably stronger than the effect of the solution temperature. For instance, the LEP decreased between 35 % and 41 % with the increase of the pore size from 250 nm to 400 nm (62.5 %) while the increase of the temperature of 100 % (20 °C to 40 °C, 30 °C to 60 °C and 40 °C to 80 °C) lead to an decrease of the LEP between 8.3 % and 24.3 %. The literature recommends a minimum LEP of 2.5 bar for a membrane utilized in MD. Based on this recommendation, TiO_2 membranes with pores sizes of up to 400 nm modified with 1 wt.% of HOC can be used in environments with temperatures up to 80 °C while membranes with a final pore size of 800 nm should not be used. The LEP values obtained for the TiO_2 membranes are competitive to the LEP reported for polymeric membranes reported in the literature (Table 7). Additionally, it can be stated that only the commercial polymeric membrane type listed in Table 7 (with a pore size ≥ 200 nm) that offers LEPs above 2.5 bar is made of PTFE. It should be kept in mind that the minimal LEP of 2.5 bar is a recommendation by the literature but that feed characteristics such as composition and temperature can require a considerable different LEP.

Table 7: LEP values of commercially available hydrophobic polymeric membranes given by the manufactures [83]

Material	Pore size: 200 nm (220 nm for PVDF)	Pore Size: 450 nm
PTFE	2.76 bar to 4.63 bar	1.38 bar to 2.88 bar
PVDF	2.04 bar to 2.29 bar	1.05 bar to 1.10 bar
PP	1.40 bar	-

Beside the temperature, the surface tension of a solution (and subsequently the LEP) is affected by its composition. For instance, due to their opposite charge the interaction of salt molecules with water molecules is stronger than the interaction of water molecules with each other resulting in higher surface tensions of saline solutions in comparison with deionized solutions (pure water). To understand to what extent the above-mentioned effect is several testing solutions containing 1 g NaCl/kg H_2O to 300 g NaCl/kg H_2O were used to determine the LEP of TiO_2 membranes with pore size between 100 nm and 800 nm modified using 1 wt.% HOC (Figure 28). The LEP could not be determined for TiO_2 membranes with a pore size of 100 nm for all NaCl concentrations since it was exceeding the maximum value quantifiable. Therefore, the LEP in regard of the NaCl concentration is not illustrated for TiO_2 membranes with a final pore size of 100 nm.

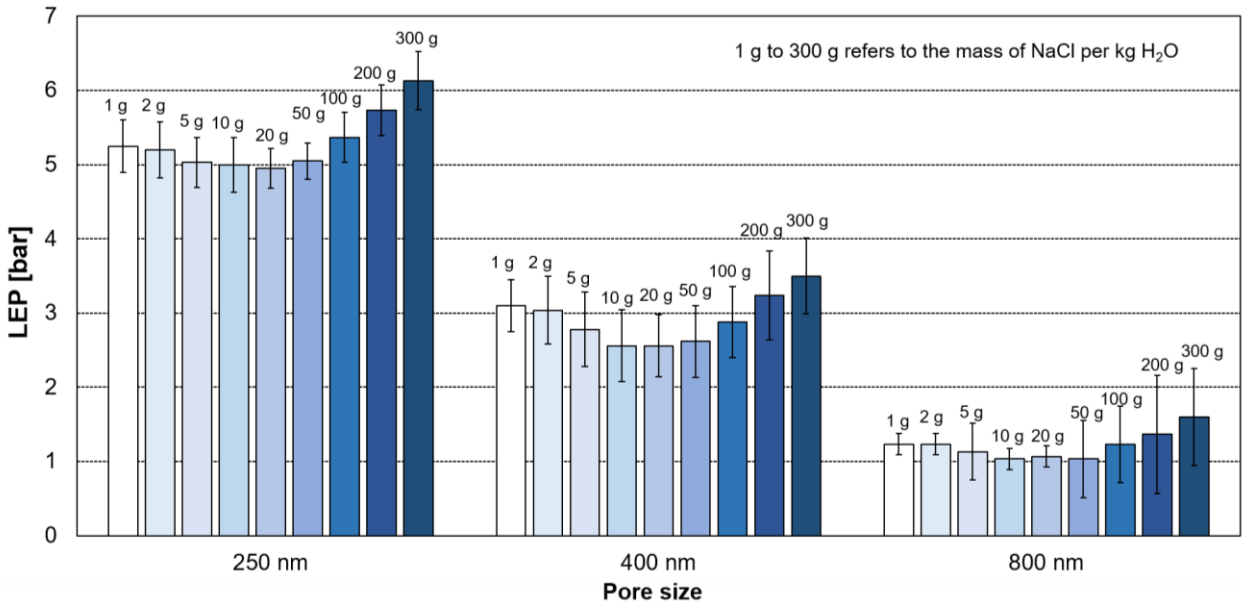

Figure 28: LEP in dependence of the pore size (final membrane layer) and NaCl concentration of the testing solution, the maximum LEP that could be measured was 7 bar (membrane: TiO_2 modified with 1 wt.% HOC, testing solution: 1 g NaCl /kg H_2O to 300 g NaCl /kg H_2O at 20 °C, minimum of 3 tests, the error bars depict the confidence intervals of the respective average value

The literature suggests that the surface tension increases linearly with the salt concentration above 0.01 mol of most inorganic salts [185,186]. However, for this study no trend could be observed for the LEP in respect to increasing NaCl concentrations up to 50 g per kg H_2O for all pore sizes. The reason for this observation could not be conclusively clarified. However, it was suggested that imperfection on the surface of the modified ceramic membranes enable the adsorption of ions present in the solutions enhancing the hydrophilic characteristics at these

locations. At low NaCl concentrations (< 50 g NaCl per kg H_2O) this effect could moderate the increase of the surface tension (and subsequently the LEP) of the testing solution with increasing salt concentrations [187]. The further increase of the NaCl concentration from 50 g per kg H_2O to 300 g per kg H_2O led to a moderate increase of the LEP for all pore sizes. The impact of the salinity is slightly more pronounced for TiO_2 membranes with a pore size of 250 nm than for larger pore sizes. It can be stated that high concentrations of salts (> 100 g NaCl/kg H_2O) could (to some extent) moderate the negative impact of larger membrane pore sizes and higher solution temperatures.

As mentioned before, the presence of organic matter can affect the surface tension of a solution strongly and therefore limit the operational capability of a hydrophobic membrane due to the reduction of the LEP [69,73,87,188]. It is imperative to understand to what extent common organic (surface-active) substances affect the wettability of hydrophobic ceramic membranes and how they limit their usability. It was concluded that the allowable concentration of organic compounds in the feed cannot be calculated but has to be determined experimentally [73]. Therefore, TiO_2 membranes with different pore sizes modified with 1 wt.% HOC were characterized regarding their LEP using a 20 wt.% ethanol and a 20 wt.% sucrose solution.

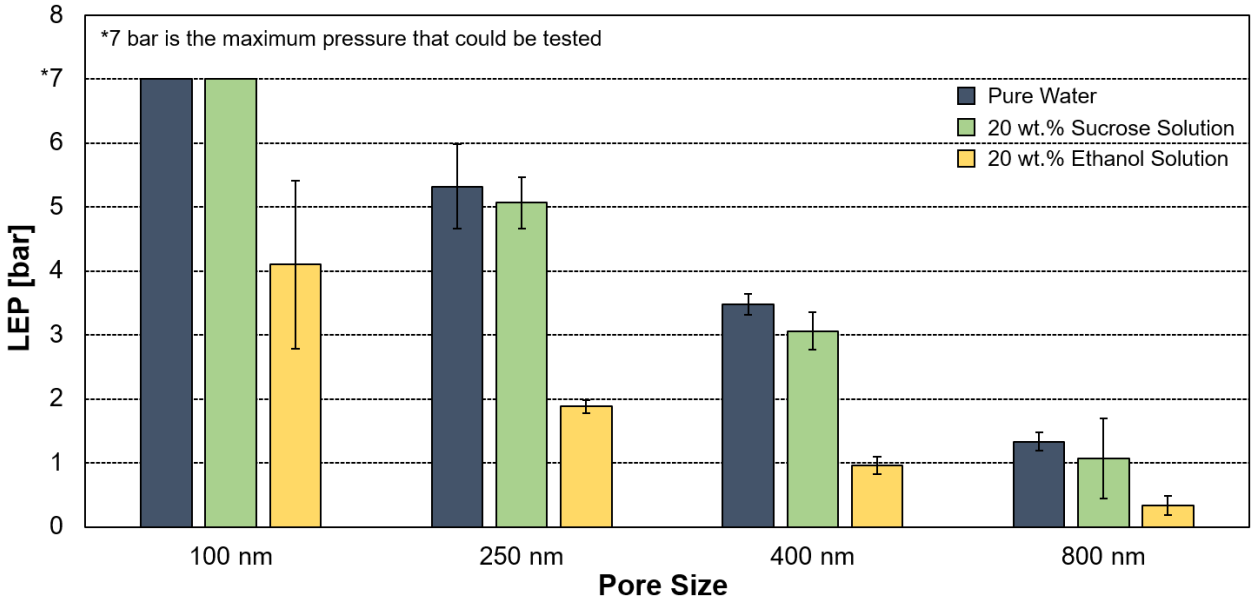

Figure 29: LEP in dependence of the pore size (final membrane layer) and sucrose as and ethanol concentration of the testing solution, the maximum LEP that could be measured was 7 bar (membrane: TiO_2 modified with 1 wt.% HOC, testing solutions: 20 wt.% ethanol and 20 wt.% sucrose at 20 °C, minimum of 3 tests, the error bars depict the confidence intervals of the respective average value

The LEP did not differ significantly when using an aqueous sugar solution as the testing liquid instead of pure water. This observation can be explained with two effects that compensate each other if sugar is added to water. The first effect is the breaking up of the hydrogen bonds in water by the hydration energy generated by the interaction of sugar and water resulting in a lower surface tension. The second effect is the increase of the intermolecular attractions caused by the polarity (charge) of the sugar molecules leading to an increase of the surface tension of the solution. Additionally, this effect is enhanced by the formation of hydrogen bonds between the water molecules and the multitude of hydroxyl groups of the sugar. The second effect is dominant for high concentrated sugar solutions. For all TiO_2 membranes the LEP was significantly lower for tests using the 20 wt.% ethanol solution instead of pure water. This observation can be explained by the reduced surface tension of the ethanol in comparison with the surface tension of pure water. This is because the cohesive forces between ethanol and water molecules (one hydrogen and one carbon atom resulting in a lower partial charge) are not as strong as the attraction forces due to hydrogen bonding (two hydrogen atoms bound to an oxygen atom) between the water molecules. The decline of the LEP caused by the presence of ethanol molecules is more pronounced for larger pore sizes (100 nm: -41 %, 250 nm: -65 %, 400 nm: -72 % and 800 nm: -75 %). It should be noted, that only the TiO_2 membranes with a pore size of 100 nm exhibit LEPs above 2.5 bar (minimum LEP recommended in the literature) when tested with an alcoholic solution containing 20 wt.% ethanol.

It must be considered that the membrane pore sizes given refer to average values determined from the pore size distributions (d50) based on mercury porosimetry tests (chapter 3.2.1). Even though these values depict the actual pore size of a membrane layer to a reasonable degree a stronger deviation of the pore size for individual membranes is possible which would severely affect the LEP. Even though the average pore size and not the pore size distribution was considered it was assumed that tests conducted on several membranes of the same type and the determination of the respective confidence intervals dampen this cause of error. Furthermore, the pore size given in the graphs represents the pore size of the final layer for asymmetric membranes and the pore size of the support for the symmetric membranes (no membrane layers present).

4.1.4 Steady State Gas Permeation – Impact of Coating Process and Layer Design

The N_2 permeance helps to understand how morphological parameters such as the pore size, tortuosity and layer thickness of a single layer (symmetrically structured) or multi-layer

(asymmetrically structured) membrane affect the gas transport through a membrane. To evaluate how the mass transfer is depended on the layer structure of ceramic membranes the N_2 permeance of asymmetrically structured (support + coating towards target pore size) and symmetrically structured (support with target pore size, no coating necessary) Al_2O_3 and TiO_2 membranes with different wall thicknesses was determined Figure 30.

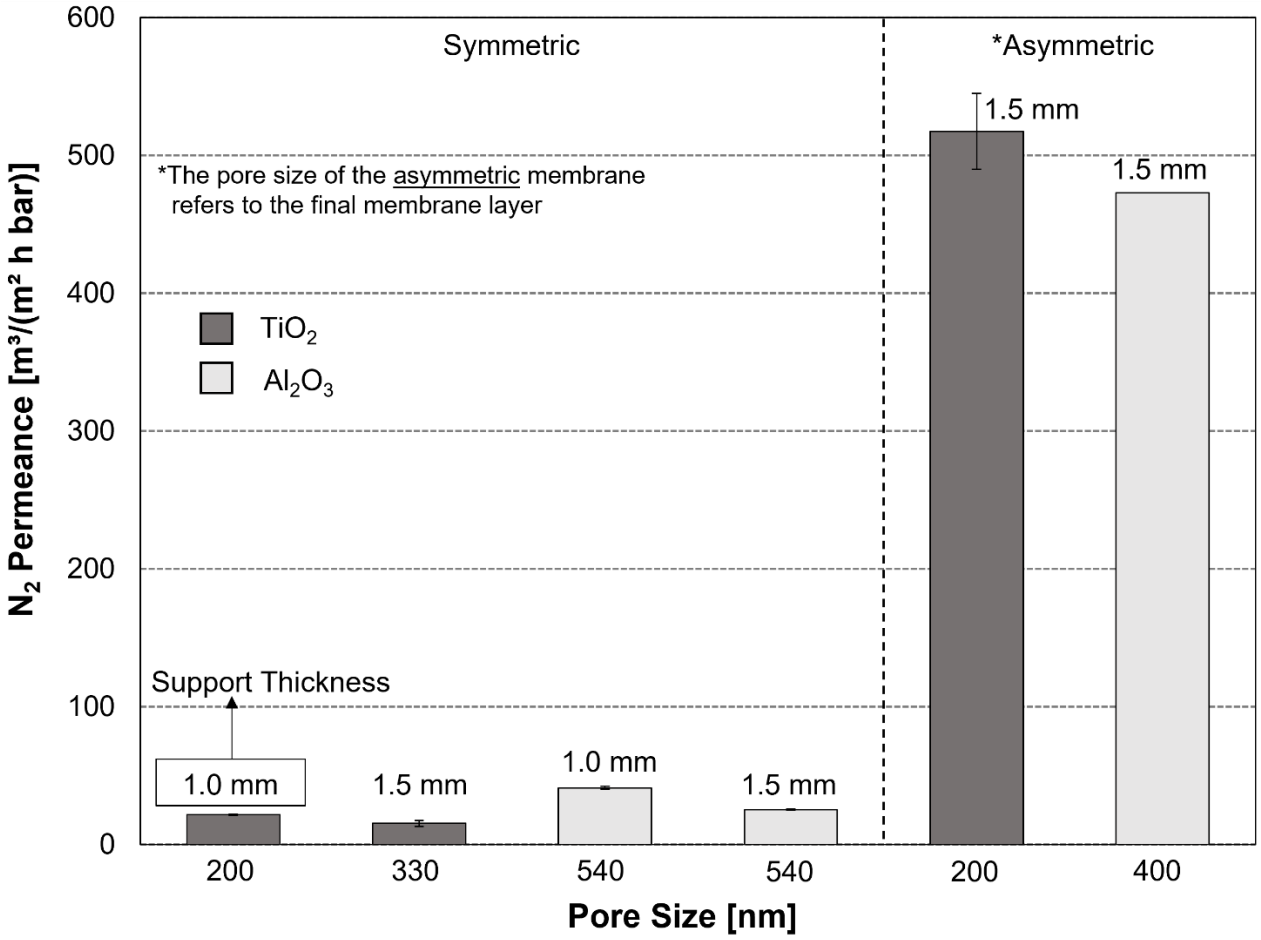

Figure 30: N_2 permeance in dependency of the membrane material, pore size, thickness and layer structure (light grey bars: Al_2O_3 and dark grey bars: TiO_2), exact layer structure is given in (Table 5), minimum of 3 tests, the error bars depict the confidence intervals of the respective average value

The symmetric Al_2O_3 membranes with a 'support' pore size of 540 nm exhibited a N_2 permeance of 25 m³/(m² h bar) and 41 m³/(m² h bar) for a wall thickness of 1.6 mm and 0.8 mm respectively. The N_2 permeance is a factor of 10 to 19 lower than the permeance of the asymmetric Al_2O_3 membrane with a final pore size of 400 nm that was determined at 473 m³/(m² h bar). A similar observation is made for the TiO_2 membranes. While the asymmetric TiO_2 membrane with a final

pore size of 200 nm showed a N_2 permeance of 517 m³/(m² h bar) the symmetric TiO_2 membranes exhibited N_2 permeances of 15 m³/(m² h bar) and 22 m³/(m² h bar) for a wall thickness of 1.6 mm (pore size: 330 nm) and 0.8 mm (pore size: 200 nm) respectively. Therefore, the N_2 permeances differ by a factor of 24 to 34 between the symmetric and asymmetric TiO_2 membranes. The mass transfer rate varies considerably between the symmetrically and asymmetrically structured membranes due to the higher mass transport resistance imposed by a smaller pore size over a greater diffusion distance. Vapor molecules that diffuse through asymmetric ceramic membranes only pass very short distances (layer thickness typically << 100 µm) with pore sizes smaller than 1 µm. The support section with a thickness of 1.0 mm or 1.5 mm (more than 90 % of the cross section of the membrane) typically exhibits large pore sizes (above 3 µm) that impose relatively small resistances. In contrast, using symmetric membranes the vapor molecules must diffuse through small pores for the whole cross-section of the membranes causing significant pressure drops along the way. This is also the reason why the thinner symmetric membranes (0.8 mm) outperform the thicker symmetric membranes (1.6 mm). This is particularly interesting if the TiO_2 membranes are considered because they do not only differ in terms of their thickness but also in respect to their pore size (the same pore size for symmetric TiO_2 membranes could not be achieved at different wall thicknesses). Even though the thicker membrane has the larger pore size (330 nm > 200 nm) it cannot compete with the thinner TiO_2 membrane regarding the N_2 permeance. The N_2 permeance of the asymmetric Al_2O_3 and TiO_2 membranes is strongly affected by the coating process which causes this TiO_2 membrane to show higher N_2 permeances than the Al_2O_3 despite its smaller pore size (Table 5).

The coating process entails the consecutive adding of membrane layers with declining pore sizes onto the ceramic support tube until the target (final) pore size is obtained. This means that each coating step affects the mass transport of the overall membrane system. To understand how each specific membrane layer affects the gas transport through asymmetrically layered ceramic membranes specifically the N_2 permeance of various support types (TiO_2, Al_2O_3, cordierite and mixed oxide) before and after each successive slurry coating step was determined (Figure 31).

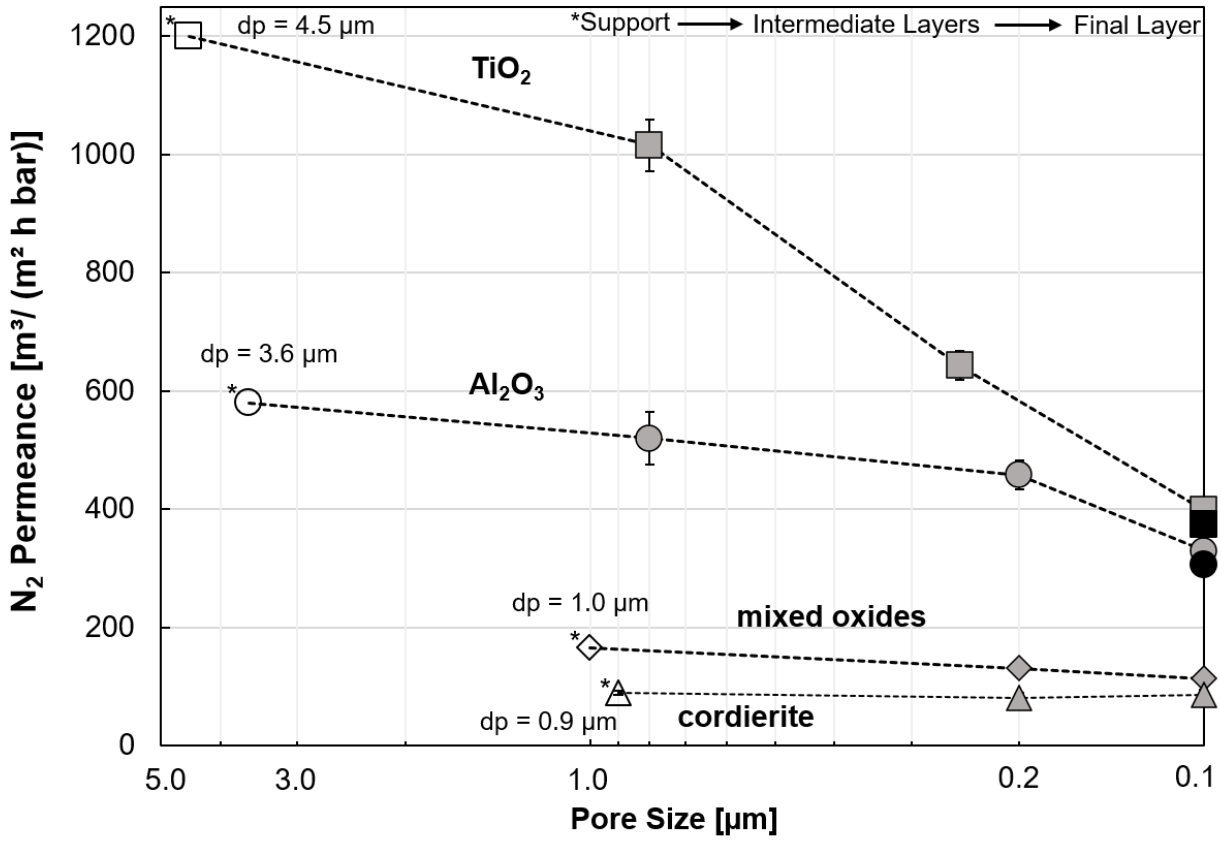

Figure 31: N_2 permeance as a function of pore size of an incrementally coated TiO_2, Al_2O_3, cordierite and mixed oxide supports (white shapes) to the pore size of 100 nm, the black markers symbolize the modification of 100 nm TiO_2 and Al_2O_3 membranes modified with 1 wt.% HOC, test conditions: T: ambient temperature, $p_{permeate}$: ambient pressure, $_{\Delta}p_{,Feed-Permeate}$: 1000 mbar, minimum of 3 tests, the error bars depict the confidence intervals of the respective average value

The maximum N_2 permeance for any overall membrane system was determined for the TiO_2 membrane starting at around 1200 m³/(m² h bar) for the support and declining due to the coating process to a minimum value of 398 m³/(m² h bar) when the final membrane layer with a pore size of 100 nm was added. The second highest permeance was determined for the Al_2O_3 membrane starting at around 580 m³/(m² h bar) for the support and declining up to 330 m³/(m² h bar) at 100 nm. The permeance of the TiO_2 and Al_2O_3 support was considerably higher than the permeance of the cordierite and mixed oxides supports (TiO_2: by a factor of around 7.2 to 13.3, Al_2O_3: by a factor of around 3.5 to 6.4). This can be attributed to the larger pores of the TiO_2 and Al_2O_3 supports in comparison to the mixed oxide and cordierite supports (Table 5) as well as the large share of the support of the overall membrane thickness. The impact of the pore size is in accordance with the viscous flow term of the DGM which considers the average pore size to the exponent of two. The mixed oxide support exhibited a significantly higher N_2 permeance than the

cordierite support (factor of 1.8) which is based on the higher porosity (10 %) and support pore size (10 %). It can be noted that the larger the support pore size (TiO_2 > Al_2O_3 > mixed oxide > cordierite) is, the stronger is the decline of the N_2 permeance in respect to successively added membrane layers towards a pore size of 100 nm. This trend is expected to some extent since the morphological properties of the intermediate and final layer do not differ as much as the supper properties between the different membranes. This causes a stronger decline of the permeance for supports with larger pore sizes. However, the porosity of the intermediate layers of the TiO_2 membrane is around 10 % smaller than the porosity of the intermediate layers of Al_2O_3 which enhances the effect in direct comparison between both membranes. In addition, due to their different support pore sizes, the membranes may also exhibit a different infiltration behavior of the membrane slurry into the support potentially resulting in localized pore blockage. Thereby, the asymmetric membranes exhibiting relatively large support pore sizes (Al_2O_3 and the TiO_2) showed similar N_2 permeances at a final layer pore size of 100 nm despite their significant imbalance regarding their support permeance. In contrast, the coating process of the mixed oxide and cordierite support affected the N_2 permeance of these membrane types only to a small extent. Moreover, it should be noted that the modification process using 1 wt.% of HOC did not lead to a significant decline of the N_2 permeance of the TiO_2 and Al_2O_3 membranes. This finding is supported by the literature that stated that this type of hydrophobic molecule predominantly forms monolayers on the ceramic surfaces [124]. Furthermore, the size of the hydrophobic chains of PFAS molecules was determined to be in the range of 1.5 nm to 2.2 nm and therefore considered do not cause considerable pore blocking [109].

To evaluate how different layer materials affect the gas permeance of the overall membrane system mixed oxides supports were coated with TiO_2, Al_2O_3 and ZrO_2 layers and characterized in respect to their N_2 permeance before and after each coating step Figure 32.

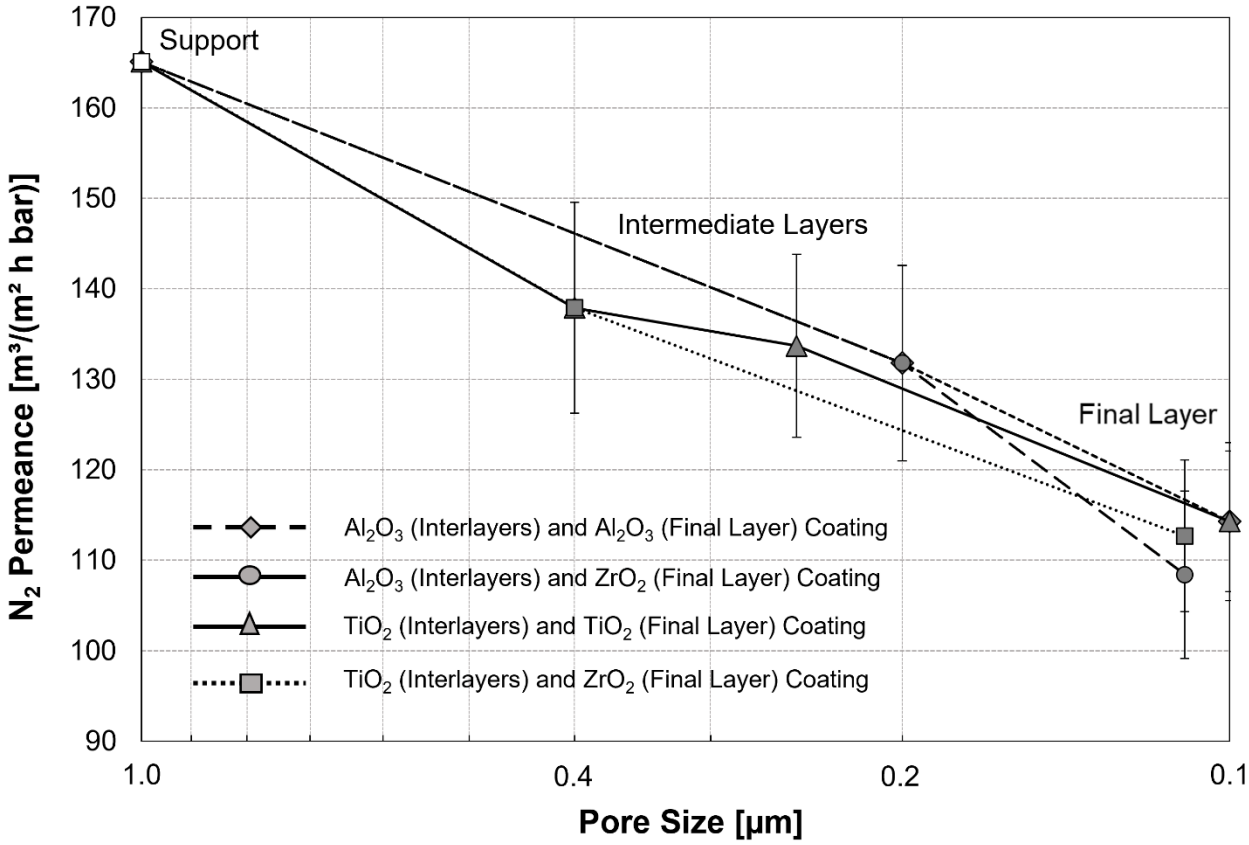

Figure 32: N_2 permeance as a function (x axis: logarithmic) of incrementally coated mixed oxides supports (pore size: 1.0 µm) towards a pore size of an active membrane layer of 100 nm (TiO_2, Al_2O_3) or 110 nm (ZrO_2, test conditions: T: ambient temperature, $p_{permeate}$: ambient pressure, $p_{\Delta,Feed-Permeate}$: 1000 mbar, minimum of 3 tests, the error bars depict the confidence intervals of the respective average value

The material chosen for the coating of the intermediate or final layers with a final pore size of 100 nm (Al_2O_3 or TiO_2) or 110 nm (ZrO_2) did not affect the N_2 permeance of the overall membrane significantly. Furthermore, the N_2 permeance was not depended on the pore size of the intermediate layers (400 nm, 250 nm or 200 nm). The coating of the final membrane layers to achieve the target pore size of 100 nm or 110 nm did cause a moderate reduction of the N_2 permeance. This reduction is not strong enough to recommend the selection of a larger pore size for the final layer due to the higher risk of wetting for larger pores.

Based on the results illustrated in Figure 31 and Figure 32 it can be concluded that the support characteristics (e. g. pore size and porosity) of the tested membranes dominate the extent of the N_2 permeance and thus the mass transfer in VMD. This can be attributed to the thickness of the support that is one magnitude higher than the thickness of the intermediate layers and the final layer combined.

4.2 Impact of Membrane Characteristics on MD Performance and Stability

Ceramic (MD) membranes differ substantially from polymeric membranes that are utilized in MD processes in respect to their layer design, morphological properties, thermal conductivity and surface characteristics. Due to the lack of research and data on ceramic membranes in MD processes the optimization of ceramic membranes specifically for MD processes could not be conducted as goal oriented as required to make them competitive to polymeric membranes. Therefore, this chapter aims to use the data on membrane properties such as pore size, porosity, layer thickness, thermal conductivity, permeance (Table 1 and chapter 4.1) to evaluate the impact of those properties on the performance in DCMD and VMD. It was decided to limit MD tests to the DCMD and VMD configuration because these are the most popular MD configurations and because VMD offers the specific benefits for the performance of ceramic membranes (e.g. less impact of the thermal conductivity of ceramic membranes than in other MD configurations). The consideration of more MD configurations would exceed the scope of this work. This insight presented in this chapter provides impetus on the framework of the utilization of ceramic membranes in MD processes and indicates how to adapt and optimize ceramic (MD) membranes effectively.

4.2.1 Impact of Membrane Properties in DCMD

In MD processes, typically membranes with pore sizes between 100 nm to 500 nm are used to reduce the risk of wetting. In this pore size range, the mass transport is defined by a combination of Knudsen and molecular diffusion [41]. Because the effect of the molecular diffusion is constant for larger pore sizes and large pores are at a higher risk of being wetted than smaller pores there is no incentive to use pore sizes larger than 500 nm [86,91,94]. As discussed before, the mass transfer in MD is affected by polarization effects. For instance, the extent of the driving force reduction due to temperature polarization is highly dependent on the thermal conductivity of the membrane (ceramic membranes > polymeric membranes) and the corresponding heat transfer via conduction. Thus, ceramic membranes typically experience considerably higher heat and driving force loss in DCMD compared to polymeric membranes. The effect of the pore size, material selection, layer design and the thermal conductivity (indirectly) on the performance in DCMD is illustrated in Figure 33.

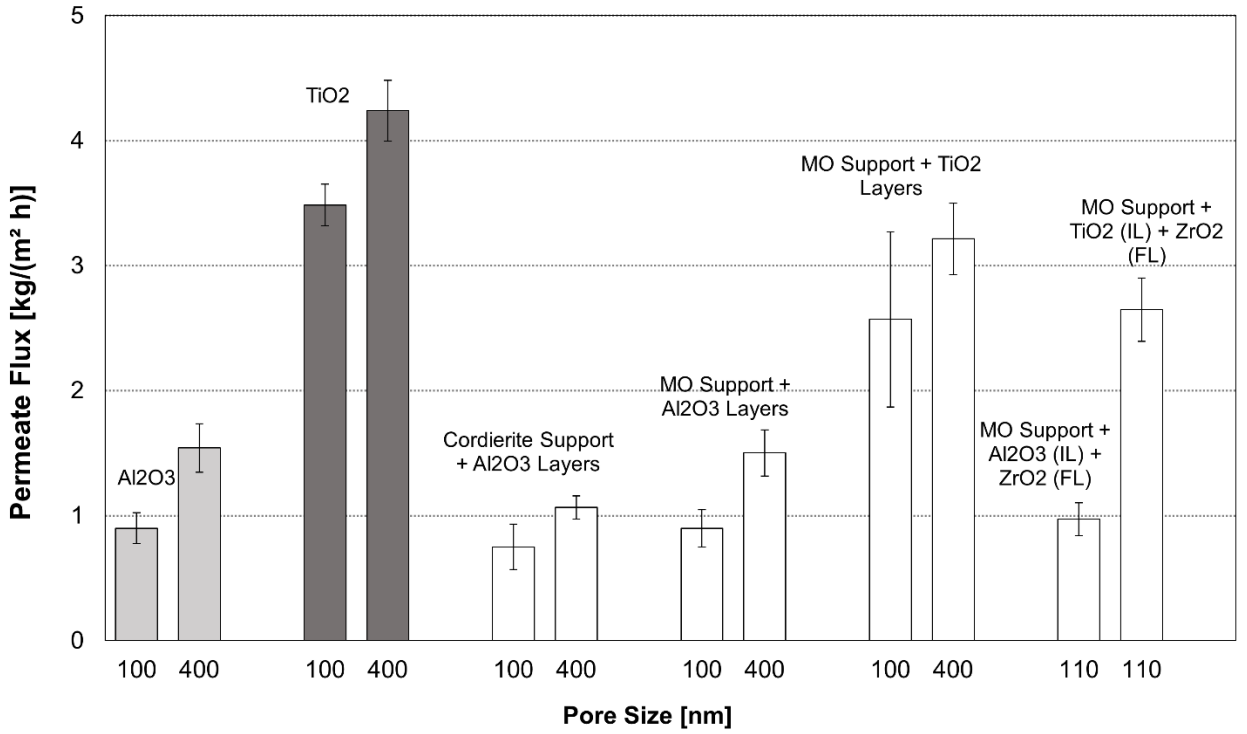

Figure 33: Permeate flux for different membranes (MO = mixed oxide support) in DCMD configuration, test conditions: Feed: 30 g NaCl/ kg H_2O, T_{Feed}: 60 °C, $T_{Coolant}$: 20 °C, v = 0.7 m/s, a minimum of 4 tests, the error bars depict the confidence intervals of the respective average value

None of the permeate fluxes presented in Figure 33 were affected by wetting. This was monitored by the electric conductivity of the coolant/permeate solution (initial value ≤ 10 µS/cm) that remained constant or decreased over the testing period. The highest permeate flux was determined for the TiO_2 membranes with a pore size of 400 nm (4.2 kg/(m² h) and the mixed oxides supports coated with TiO_2 and ZrO_2 layers (2.7 kg /(m² h) to 3.2 kg /(m² h)). The Al_2O_3 membranes, the cordierite and the mixed oxide supports coated with Al_2O_3 membrane layers exhibited significant lower permeate fluxes between around 0.8 kg/(m² h) and 1.5 kg/(m² h). The competitiveness of the TiO_2 membrane is based on the relatively large support pore size and the relatively low thermal conductivity of the material. As illustrated in chapter 4.1.4 the positive effect of larger support pore sizes is due to lower pressure drops over the support thickness. In addition, the partial wetting of the support (due to the large support pores, TiO_2: 4.5 µm and Al_2O_3: 3.6 µm) by the cooling liquid on the permeate side in DCMD affects the mass transport. The wetting of the support leads to a reduction of the effective membrane thickness resulting in a reduction of the diffusion distance for the vapor molecules (and consequently to a decrease of the pressure drop) through the membranes. However, the partial or complete wetting of the support does also lead to a stronger impact of the membrane layer characteristics (pore size and thermal conductivity).

This assumption is supported by the illustrated results above showing that all but the MO supports coated with TiO_2 membrane layers exhibited significantly higher permeate fluxes (by a factor between 1.2 und 1.7) for the larger final membrane layer pore size (100 nm vs 400 nm). The MO support coated with intermediate layers of TiO_2 and a final layer of ZrO_2 demonstrated permeate fluxes that were higher by a factor of 2.7 in comparison to a similar membrane that only differs in respect to the intermediate layers (Al_2O_3 instead of TiO_2) even though these membranes exhibited a similar N_2 permeance (Figure 32). This means that the wetting of the support results in an increased heat transfer via conduction subsequently causing stronger temperature polarization effects leading to significant driving force losses. The extent of this effect is elevated by the reduced mixing of the coolant/permeate liquid inside the wetted support pores and highly depended on the thermal conductivity of the membrane layers. This is the reason why the Al_2O_3 membranes exhibited considerably lower permeate fluxes than the TiO_2 membranes. The high thermal conductivity of the Al_2O_3 membrane layers overcompensate the positive effect of the reduced diffusion distance. It can also be stated that the effect of the thermal conductivity is stronger on the permeate flux than the support pore size. Therefore, those supports with relatively small pore sizes but with membrane layers exhibiting low thermal conductivities (MO + TiO_2/ZrO_2) showed considerably higher permeate fluxes than membrane systems with layers having higher thermal conductivities (MO + Al_2O_3, cordierite + Al_2O_3). In general, the support characteristics do not affect the permeance in DCMD significantly as can be seen by comparing membrane systems exhibiting different support properties (pore size and thermal conductivity) but similar permeate fluxes (Al_2O_3 vs cordierite + Al_2O_3, MO + Al_2O_3). It can be concluded that in DCMD, the asymmetric layer composition of ceramic membranes with large support pore sizes is only advantageous if the low thermal conductivities of the membrane layers prevent stronger temperature polarization effects caused by the reduced ‘effective’ membrane thickness. Those membranes that either exhibit low thermal conductivities at large support pore sizes (TiO_2) or low thermal conductivities and high porosities (mixed oxide support + TiO_2 and ZrO_2 layers) performed relatively well in comparison with membranes with less favorable characteristics (e. g. Al_2O_3, Cordierite + Al_2O_3). However, the extent of each phenomenon and how they mitigate each other was not studied in this work and was not quantified for any of the tested membranes.

4.2.2 Impact of Membrane Properties in VMD

As illustrated before, in VMD strong temperature polarization effects are averted by the low absolute pressure applied to the permeate side acting as a thermal insulation. This effect is particularly advantageous for ceramic membranes and partly mitigates their relatively high thermal

conductivities. Furthermore, the low absolute pressure also leads to the removal of inert gases from the pores which act as an additional barrier to the vapor molecules transported through the pores, making Knudsen diffusion and viscous flow the dominant mass transport mechanisms. In order to gain insight on how the characteristics of ceramic membranes affect the mass transport in VMD membranes made from Al_2O_3, TiO_2, cordierite and mixed oxides with different layer compositions and pore sizes have been tested in VMD (Figure 34).

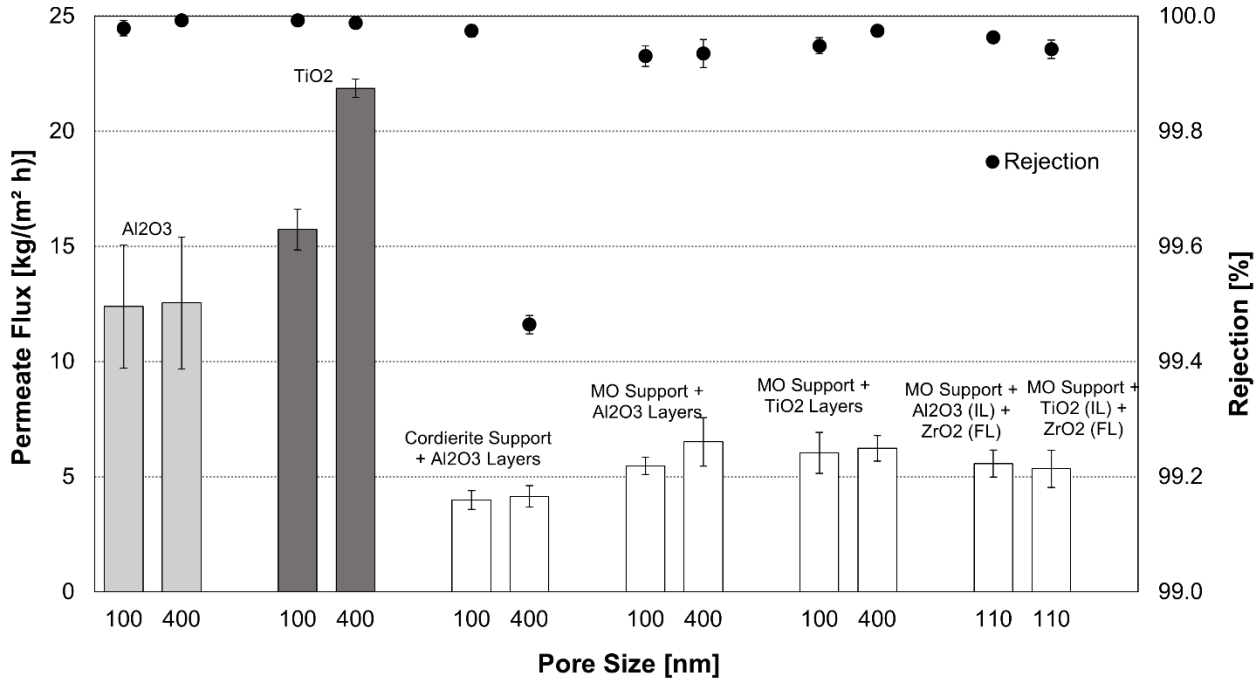

Figure 34: Permeate fluxes (bars) for different membranes (MO = mixed oxide support) in VMD configuration and the corresponding salt rejection (dots), test conditions: Feed: 30 g NaCl/kg H_2O, T_{Feed}: 60 °C, $T_{Coolant}$: 3 °C, v = 0.7 m/s, p_{abs}: 100 mbar, minimum of 3 test, the error bars depict the confidence intervals of the respective average value

The highest permeate flux was determined for the TiO_2 membranes (15.7 kg/(m² h)) and 21.7 kg/(m² h)), followed by the Al_2O_3 membranes at around 12.5 kg/(m² h), the mixed oxides and cordierite membranes respectively. This is in accordance with the N_2 permeance results discussed in chapter 4.1.4 and in conformity with the corresponding support pore size (Table 5). In contrast to the results obtained in DCMD, the permeate fluxes obtained in VMD indicate that the characteristics of the intermediate and final membrane layers (e. g. pore size and thermal conductivity) only affect the mass transport of ceramic membranes in VMD significantly if the permeance of the support is high. The performance in VMD is mainly defined by the support properties. For instance, the material selection of the interlayers and final layers (Al_2O_3, TiO_2 and

ZrO_2) as well as the variation of the final pore size of the Al_2O_3 and cordierite membranes did not affect the extent of permeate flux significantly. Only the results obtained for the TiO_2 membranes indicate a dependency on the pore size of the final layer. The decrease of the pore size from 400 nm to 100 nm led to a significant decrease in permeate flux of the TiO_2 membranes which is in accordance with the determined N_2 permeances (Figure 31). As mentioned before, this possibly caused by combination of localized pore blockage due to the slurry coating process as well as the stronger impact fine membrane layers have on the mass transport of high permeance membrane types. For the other membrane types the decrease of the pore size of the final membrane layer from 400 nm to 100 nm did not cause a significant decrease of the permeate flux. Therefore, the selection of the final layers with a pore size of 100 nm instead of 400 nm is recommended (except for TiO_2 membranes) to ensure pronounced hydrophobic surface characteristics and reduced risk of wetting. The salt rejection of the tested membranes was excellent (> 99.9 %) for all but the cordierite support with the 400 nm Al_2O_3 membrane layers (~99.5 %). This slightly reduced rejection can be explained by minimal infiltration of the feed into defect pores (= imperfections within the membrane layer) caused by the specific interaction of the 400 nm membrane coating and the cordierite support. In consideration of the discussed findings and the results illustrated in chapter 4.1.4 it can be stated that the asymmetric layer design of ceramic membranes is advantageous to the extent of the mass transport in VMD if the pore size of the support is considerably larger than 1 µm and substantial pore blockage due to the slurry coating process is avoided.

4.2.3 The Effect of the Support Thickness in VMD and DCMD

As shown in chapter 4.1.4 the support characteristics of ceramic membranes affect the mass transfer of the overall membrane considerably. This is because the support is typically by orders of a magnitude thicker than the membrane layers. It can be stated that the thicker the support the higher the mass transfer resistance, because of the longer diffusion distance the vapor molecules must cover to permeate the membrane. A thicker support leads to better thermal insulation between the feed and the permeate side of the membrane reducing the heat transfer via conduction and preventing significant driving force losses. But as stated before this effect is less pronounced in VMD. Furthermore, a thinner support leads to a steeper salinity gradient over the membrane in DCMD which enhances the mass transfer caused by osmotic distillation resulting in a dilution of the feed by pure water from the permeate side [189]. Below is the effect of the support thickness for TiO_2 and Al_2O_3 membranes (pore size of the final membrane layer: 100 nm) in DCMD and VMD configuration depicted (Figure 35).

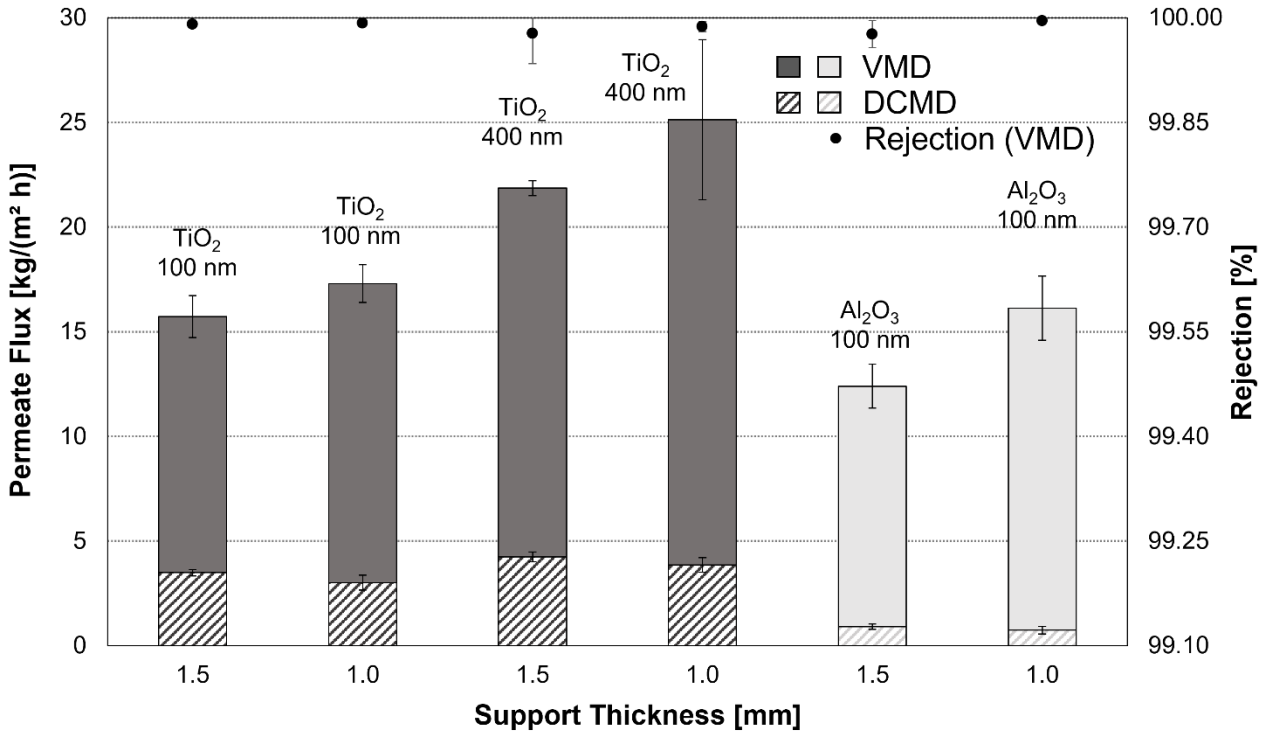

Figure 35: Permeate flux (columns) and salt rejection (dots, only VMD) for TiO_2 (final pore size: 100 nm or 400 nm) and Al_2O_3 (final pore size: 100 nm) membranes with a support wall thickness of 1.5 mm and 1.0 mm in DCMD and VMD configuration, DCMD test conditions: Feed: 30 g NaCl/ kg H_2O, T_{Feed}: 60 °C, $T_{Coolant}$: 20 °C, v = 0.7 m/s, VMD test conditions: Feed: 30 g NaCl/ kg H_2O, T_{Feed}: 60 °C, $T_{Coolant\ (VMD)}$: 3 °C, v = 0.7 m/s, $p_{abs\ (VMD)}$: 100 mbar, minimum of 3 tests, the error bars depict the confidence intervals of the respective average value

Based on the decrease of the electric conductivity of the coolant/permeate liquid (initial value ≤ 10 µS/cm) it can be stated that none of the DCMD results illustrated in Figure 35 were affected by wetting. The permeate flux of TiO_2 and Al_2O_3 membranes with a final pore size of 100 nm and 400 nm was not considerably affected by the reduction of the support thickness from 1.5 mm to 1.0 mm in DCMD. As explained in chapter 4.2.1, it can be assumed that the positive effect of the lower diffusion distance (the result of thinner supports) was compensated by an increased heat transfer via conduction that subsequently led to a higher driving force loss. The 100 nm TiO_2 membranes exhibited permeate fluxes that were, by a factor from 3.7 to 4.1, higher than the permeate flux of the Al_2O_3 membranes with the same pore size. This is due to stronger temperature polarization effects caused by the higher thermal conductivity of Al_2O_3 membranes (by a factor of 2.3, Figure 23) and the more pronounced pressure drop due to the smaller support pore size of these membranes. The results clearly indicate that the negative effect caused by thinner support walls is stronger for membranes with relatively high thermal conductivities such as Al_2O_3 membranes. In VMD, superb rejections above 99.9 % were achieved for all membrane types. The reduction of the support wall thickness led to a significant increase of the permeate flux

for the thinner TiO_2 membranes (7 % to 15 %) with a pore size of 400 nm and the thinner Al_2O_3 membranes (22 %) with a pore size of 100 nm. It is apparent that the positive effect of a shorter diffusion distance reducing the mass transfer resistance for the vapor molecules is not entirely compensated for by an increased heat transfer through conduction in VMD. It is apparent, that thin TiO_2 and Al_2O_3 membranes achieve similar permeate fluxes for a pore size of 100 nm. This is because, TiO_2 membranes are stronger affected by the coating process to achieve a pore size of 100 nm than Al_2O_3 membranes but also because Al_2O_3 membranes benefit more from the good thermal insulation in VMD compensating their higher thermal conductivity.

4.2.4 Impact of Layer Structure and Modification in VMD

It was shown in chapter 4.1.4 and chapter 4.2.2 that ceramic membranes shower considerably higher fluxes in VMD than in DCMD and that the asymmetric layer structure is beneficial for the mass transport in VMD. As mentioned before, the competitiveness of VMD is based on the lower mass transfer resistance due to the removal of inert gases from the pores as well as the averting of strong temperature polarization effects due to the low permeate pressure. Therefore, the following MD tests were limited the VMD configuration. In order to gain further insight on the performance of symmetrically structured ceramic membranes in VMD (in comparison with asymmetrically structured ceramic membranes), Al_2O_3 and TiO_2 membranes with different layer designs, pore sizes, and surface modifications were tested in VMD (Figure 36).

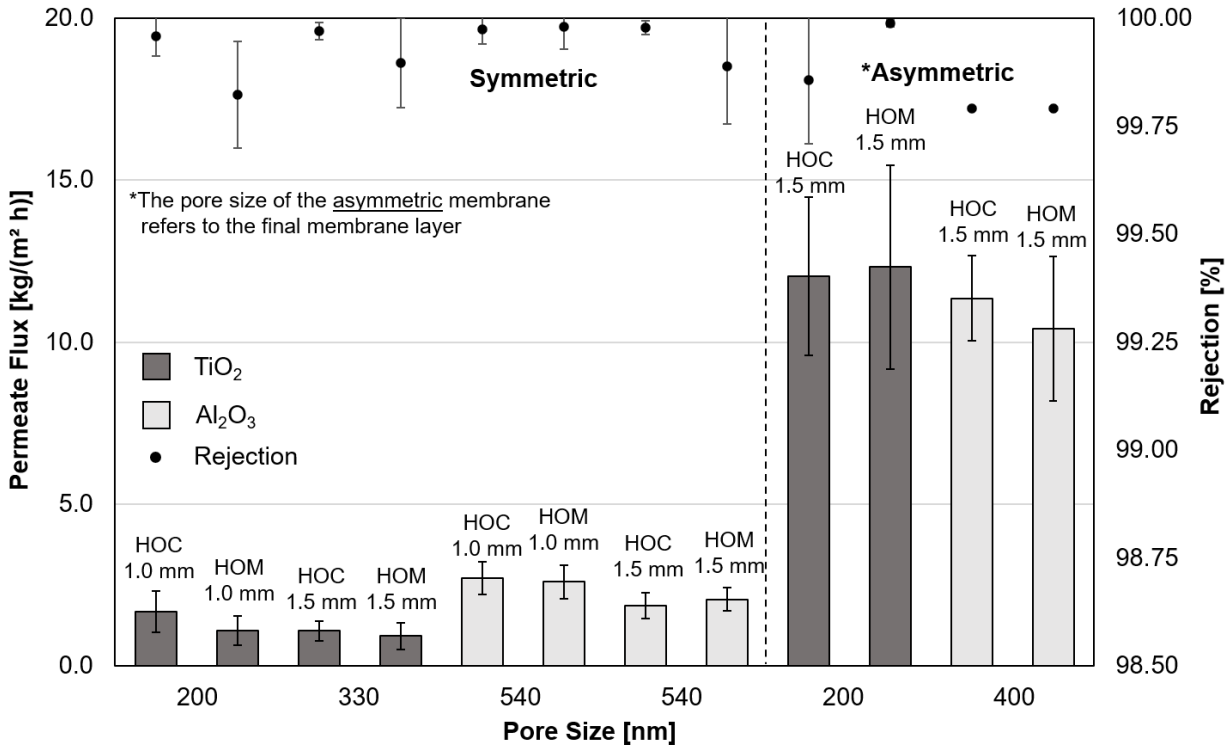

Figure 36: Permeate flux (bars) and salt rejection (dots) for Al_2O_3 (light gray bars) and TiO_2 (dark gray bars) membranes in dependence to the layer design, pore size, thickness (1.0 mm and 1.5 mm) and surface modification (2 wt.% HOC and 2 wt.% HOM) in VMD, test conditions: Feed: 30 g NaCl/ kg H_2O, T_{Feed}: 60 °C, $T_{Coolant\ (VMD)}$: 3 °C, v = 0.7 m/s, p_{abs}: 100 mbar, minimum of 3 tests, the error bars depict the confidence intervals of the respective average value

The permeate fluxes of symmetric and asymmetric membranes are in accordance with the N_2 permeances shown in chapter 4.1.4. The asymmetric membranes outperformed the symmetric membranes by a factor of around 5 for Al_2O_3 membranes and by a factor of around 7 for TiO_2 membranes. Due to their larger pore size the symmetric Al_2O_3 membranes show slightly higher permeate fluxes than the symmetric TiO_2 membranes. Once again, these findings demonstrate how strongly the layer design of ceramic membranes affects the mass transfer in MD. Regarding the permeate flux the symmetric ceramic membranes are simply not competitive with asymmetric ceramic membranes in VMD. The comparatively long diffusion distances through the relatively small pores lead to considerably higher pressure drops and driving force losses. The decrease of the wall thickness for the symmetric membranes led to a slight but not significant increase in permeate flux for the Al_2O_3 membranes (same pore size). For the symmetric TiO_2 membranes the effect of the reduction of the wall thickness was not significant and was likely offset by the decrease of the pore size. Furthermore, the variation of the modification agent did not lead to a significant change of permeate flux or rejection for any membrane type. All membrane types achieved good rejections above 99.75 %.

4.2.5 Stability of Asymmetric and Symmetric Ceramic Membranes

Ceramic membranes are considerably more robust than most polymeric membranes. However, the selectivity of asymmetrically structured ceramic membranes utilized in MD processes is defined by the hydrophobic layer present on the surface of the final membrane layer of asymmetric ceramic membranes. The overall robustness of the hydrophobic surface characteristics in respect to the type of hydrophobic molecules bonded to the hydroxyl rich surfaces of the membrane is not fully known. It is possible that the hydrophobic coating constitutes a fundamental vulnerability limiting the usability of hydrophobic ceramic membranes to specific environments. Therefore, asymmetric TiO_2 and Al_2O_3 single channel membranes with different pore sizes were modified using 1 wt.% of HOC or 1 wt.% HOG and characterized regarding their initial LEP. Subsequently, these modified membranes were either cooked in a moderate-saline and alkaline (50 g Na_2CO_3 + 50 g NaCl per kg H_2O), in a neutral (pure water) or in a moderate-saline and acidic (135 g HCl (37 wt.%) + 50 g NaCl per kg H_2O) solution for 96 hours and subsequently reevaluated regarding their LEP (Figure 37 and Figure 38). As stated before, HOC and HOG were chosen as hydrophobic agents because they were used successfully to modify hydrophilic ceramic membranes prior to this work but have not been characterized in respect to the stability of the hydrophobic coating.

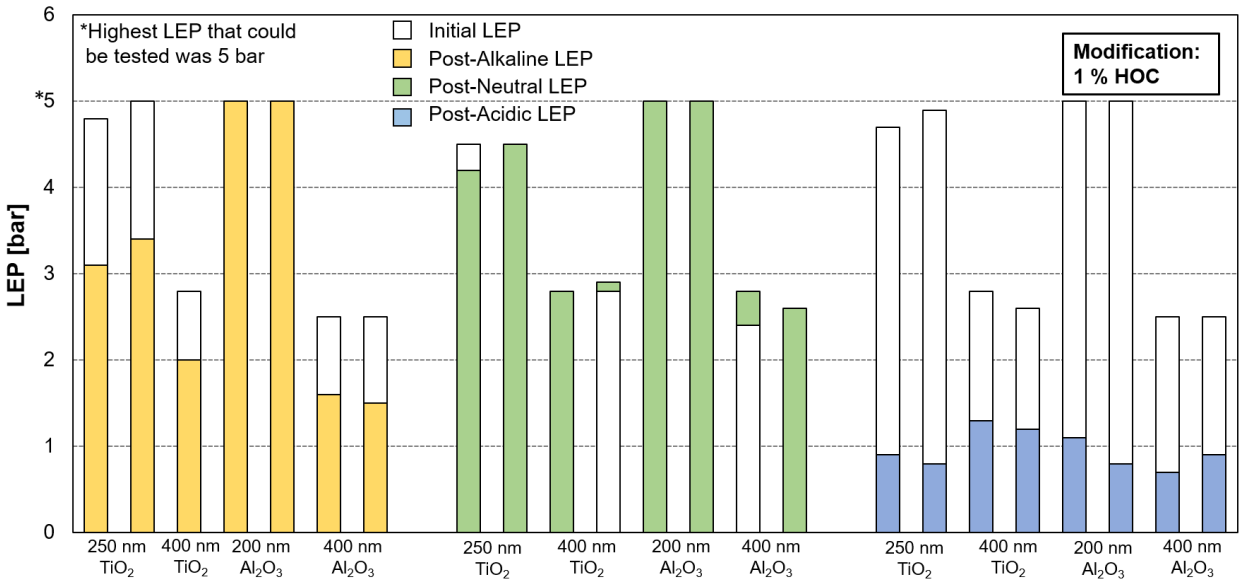

Figure 37: LEP in regard to membrane material and pore size before and after stress tests with an alkaline (50 g Na_2CO_3 + 50 g NaCl per kg H_2O), neutral (pure water) and acidic solution (135 g HCl (37 wt.%) + 50 g NaCl per kg H_2O) for 96 hours at around 100 °C, modification: 1 wt.% HOC, 2 tests per membrane type (exception: 400 nm TiO_2: one test), the results depicted above are based on individual tests (2x per solution and membrane type)

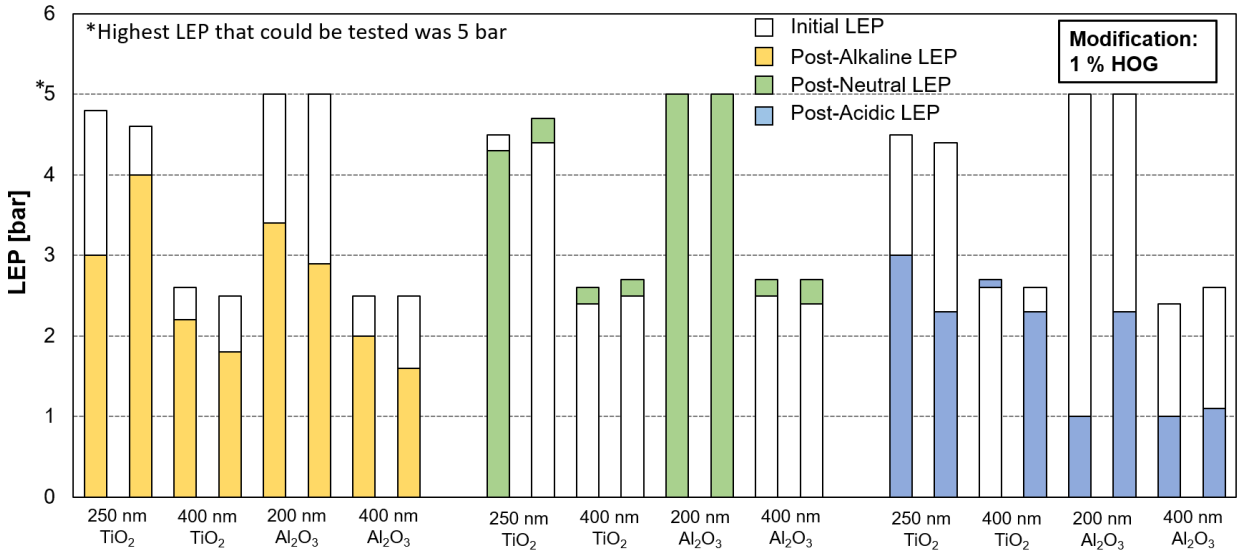

Figure 38: LEP in regard to membrane material and pore size before and after stress tests with an alkaline (50 g Na_2CO_3 + 50 g NaCl per kg H_2O), neutral (pure water) and acidic solution (135 g HCl (37 wt.%) + 50 g NaCl per kg H_2O) for 96 hours at around 100 °C, modification: 1 wt.% HOG, 2 tests per membrane type,), the results depicted above are based on individual tests (2x per solutions and membrane type)

The initial LEPs of TiO_2 and Al_2O_3 membranes with a pore size of 400 nm modified with HOC or HOG were determined at around 2.5 bar. The initial LEP for of TiO_2 and Al_2O_3 membranes with a pore size of 250 nm (TiO_2) or 200 nm (Al_2O_3) modified with HOC or HOG were determined in the range of 4 bar to 5+ bar (maximum LEP that could be determined was 5 bar). Both hydrophobic agents achieved LEPs in the same range technically enabling asymmetric Al_2O_3 and TiO_2 with pore sizes between 200 nm and 400 nm to be utilized in MD processes (2.5 bar is recommended as the minimal LEP by the literature). The LEP of most of the membranes that were cooked using pure water (neutral solution) was not considerably affected (white and green bars). Some membranes showed a moderate incline in LEP after the treatment with the hot neutral solution (bars with a green top). The incline of the LEP after the treatment with the neutral solution is related to the way the silane agent is bonded with the membrane surface. Some of the silane molecules are chemically bonded to the ceramic surface via metal-siloxane bonds (Ti-O-Si or Al-O-Si) while the others are physiosorbed to the surface. The chemically bonded silanes have the ideal orientation as the hydrophobic alkyl chains are perpendicular to the surface while the physiosorbed silanes can exhibit different orientations. After the cooking of the membranes in the neutral solution the physiosorbed layer was possibly removed leading to the uncovering of the chemisorbed layer resulting in a slightly increased LEP.

The treatment with the hot saline and alkaline solution led to a moderate decline of the LEP (up to 40 % for HOC modified membranes and up to 42 % for HOG modified membranes) of all

membrane types except for the Al_2O_3 membrane (pore size of 200 nm) modified with HOC. This indicates a similarly pronounced stability of HOC and HOG modified surfaces against hot saline and alkaline solutions. The degeneration of the LEP is caused by the break-up of the Si-O-M bonds due to high availability of hydroxyl groups.

None of the asymmetric membranes modified with HOC could withstand the contact with the hot saline and acidic solution resulting in the decline of the LEP below 1.3 bar (decline of 64 % and 84 %) making them unsuitable for the use in MD processes. The Al_2O_3 membranes modified with HOG showed a similar vulnerability (decline of the LEP between 58 % and 80 %) towards the hot saline and acidic environment as the Al_2O_3 membranes modified with HOC. The degeneration of the LEP is caused by the break-up of the Si-O-M bonds due to high availability of hydronium groups at the pH of 0. Unexpectedly, the LEP of the TiO_2 membranes modified with HOG was affected by the treatment with the hot saline and acidic solution indicating that TiO_2 membranes modified with HOG could potentially be successfully utilized in acidic environments. One possible explanation of this observation is that the type of hydrophobic layer formed on the TiO_2 surface using HOG instead of HOC is more effective in shielding the membrane surface from the reactive groups despite similar CA and LEP values.

Even though the homogenic layer structure of symmetric ceramic membranes is not beneficial to the mass transport in MD (as was shown in chapter 4.1.4 and chapter 4.2.4) it could enable the treatment of highly aggressive environments that are too extreme for asymmetric ceramic membranes. This is because, the selectivity of symmetrically structured ceramic membranes is not depended on the integrity of a thin ‘final’ membrane layer coated on a support structure (as is the case for asymmetric membranes) but is prevalent over the whole cross-sectional area of the membrane. To study the potential benefits of modified symmetric ceramic membranes in respect to their stability towards extreme environments a variety of symmetric and asymmetric TiO_2 and Al_2O_3 membranes modified with 2 wt.% of HOC and 2 wt. of HOM were cooked in a highly saline and alkaline, highly saline (neutral) and highly saline and acidic solution for 96 hours. The LEP of the tested membranes before and after the treatment with the saline and alkaline solution is illustrated in Figure 39.

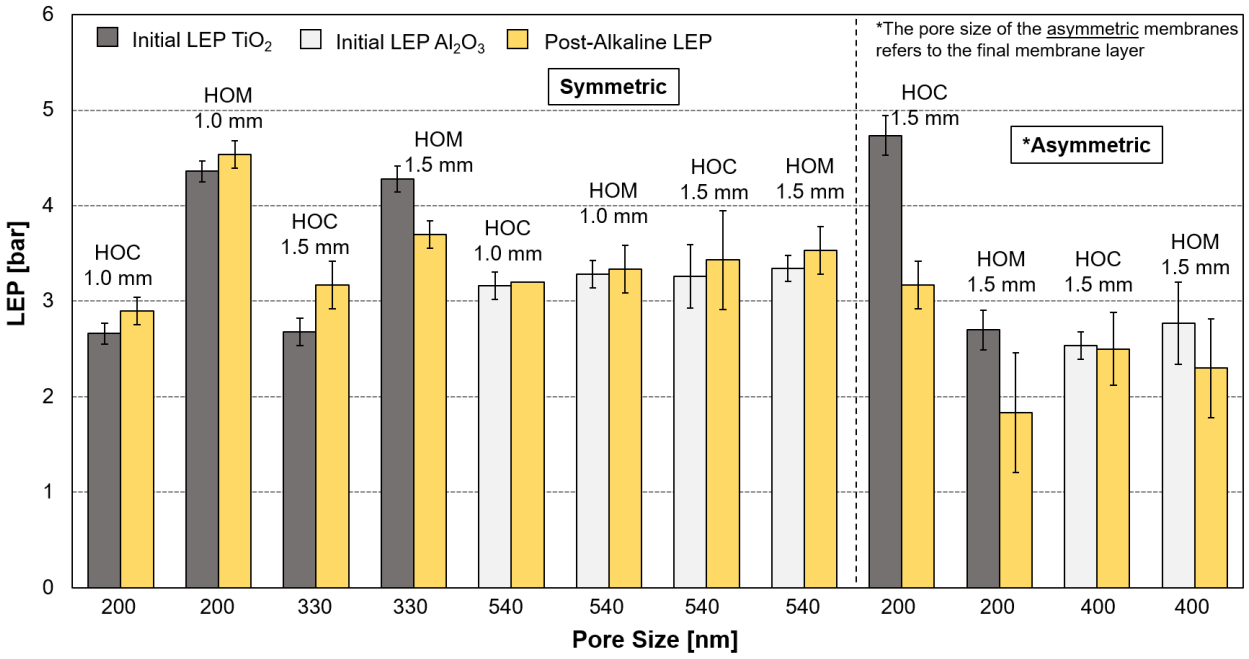

Figure 39: LEP in regard to membrane material (Al_2O_3: light gray bars and TiO_2: dark gray bars), layer design, pore size, thickness (1.0 ,mm and 1.5 mm) and surface modification (2 wt.% HOC and 2 wt.% HOM) before and after stress tests using an alkaline and saline solution (96 hours, 100 °C, 250 g NaCl + 50 g Na_2CO_3 per kg H_2O), minimum of 3 tests, the error bars depict the confidence intervals of the respective average value

The treatment using the alkaline solution containing high concentrations of NaCl did not significantly affect the LEP of the symmetric Al_2O_3 membranes and the asymmetric Al_2O_3 membrane modified with 2 wt.% HOC. The asymmetric Al_2O_3 membrane modified with 2 wt.% showed a slight decline of LEP (15 %) in comparison of the initial LEP. Except for the symmetric TiO_2 membrane with a thickness of 1.5 mm modified by the non-fluorinated agent (2 wt.% HOM) and the asymmetric TiO_2 modified with 2 wt.% HOC the LEP did not change significantly for any membrane after the treatment with the hot alkaline and saline solution. The strongest decline in LEP was determined for the asymmetric TiO_2 membrane modified with HOC (~ 30 %) which also exhibited the highest initial LEP at around 4.7 bar. It can be concluded that the symmetric TiO_2 and Al_2O_3 membranes are stable towards the hot alkaline and hypersaline solution. The stability of the asymmetric Al_2O_3 membranes is sufficient as well but the final pore size should be chosen to be smaller than 0.4 µm to ensure a high enough initial LEP. The stability of the asymmetric TiO_2 membranes is not sufficient for an application in environments characterized by extreme low pH, hot temperatures and high concentrations of NaCl values. The effect of a hot and highly saline solution (250 g NaCl per kg H_2O, pH = 7) on the LEP of symmetric and asymmetric ceramic membranes is shown in Figure 40.

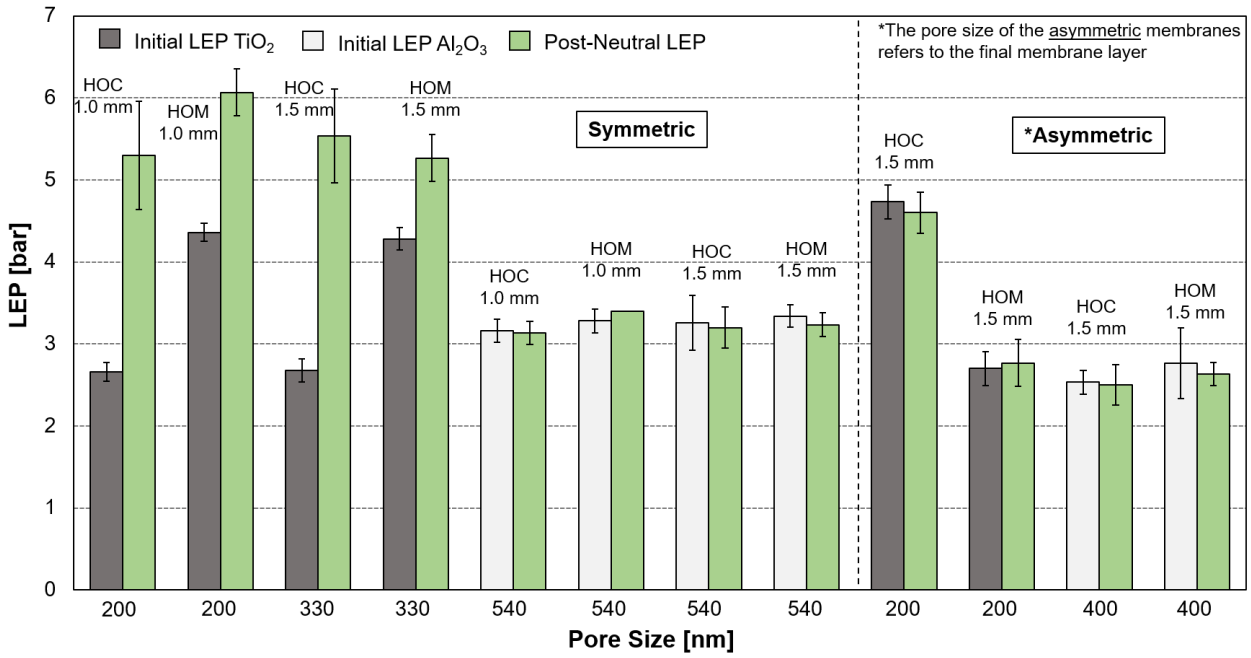

Figure 40: LEP in regard to membrane material (Al_2O_3: light gray bars and TiO_2: dark gray bars), layer design, pore size, thickness (1.0 mm and 1.5 mm) and surface modification (2 wt.% HOC and 2 wt.% HOM) before and after stress tests using a hot saline solution (96 hours, 100 °C, 250 g NaCl per kg H_2O), minimum of 3 tests, the error bars depict the confidence intervals of the respective average value

The LEP of the symmetric and asymmetric Al_2O_3 membranes was not significantly affected by the treatment with the hot saline solution at a neutral pH value. The same applies to the asymmetric TiO_2 membranes that did not exhibit significantly different LEP after the stability test. The non-fluorinated and the fluorinated modification showed the same stability towards the hot saline solution. However, after the treatment with the hot solution all symmetric TiO_2 membranes exhibited a LEP higher than 5 bar regardless of the modification agent. This indicates a better exposure of the well bonded and favorably oriented chemisorbed layer of the hydrophobic chains of the silanes due of the treatment with the hot and saline solution. The LEP of symmetrically and asymmetrically structured ceramic membranes modified with 2 wt.% HOC and 2 wt.% HOM before and after the treatment with the hot saline and acidic solution is shown in Figure 41.

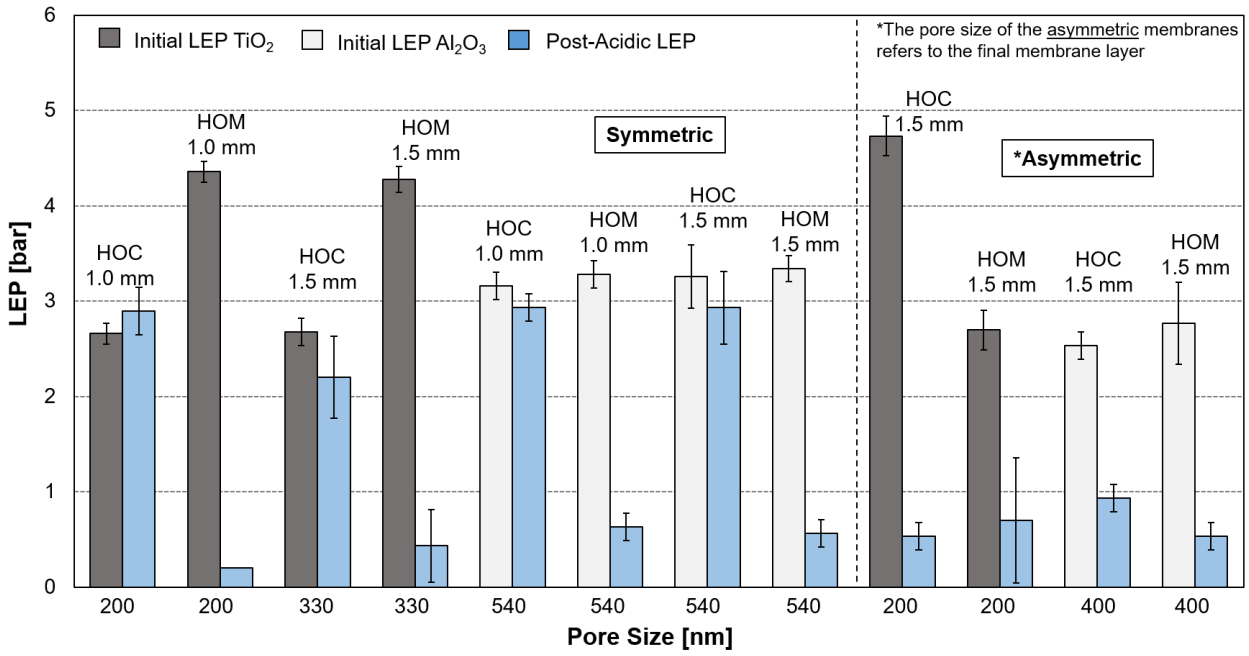

Figure 41: LEP in regard to membrane material (Al_2O_3: light gray bars and TiO_2: dark gray bars), layer design, pore size, thickness (1.0 mm and 1.5 mm) and surface modification (2 wt.% HOC and 2 wt.% HOM) before and after stress tests using an acidic and saline solution (96 hours, 100 °C, 250 g NaCl + 1 kg HCl (5 wt.%) minimum of 3 tests, the error bars depict the confidence intervals of the respective average value

Except for the symmetric Al_2O_3 and TiO_2 membranes (1.5 mm and 1.0 mm) modified with 2 wt.% HOC no other membrane type has shown sufficient stability towards the hot saline and acidic environment. All other membrane types exhibited a LEP of ≤ 1 bar after the treatment with the acidic solution accounting for a reduction of the LEP of up to 80 %. As mentioned before, one reason for the good stability of HOC modified TiO_2 membranes is the effective shielding of the membrane surface from aggressive components in aqueous solutions due to the well pronounced hydrophobicity because of the low dipole of the fluorinated agent. However, the stability of the symmetric ceramic membranes is not just based on the modification with fluorinated hydrophobic agent (HOC) since the asymmetric ceramic membranes modified with HOC show a considerable reduction in LEP for both material groups. Symmetric Al_2O_3 membranes modified with HOC exhibited a higher initial LEP than the symmetric TiO_2 membranes despite considerably larger pores. Therefore, the surface modification using the fluorinated agent is more effective for symmetric Al_2O_3 membranes than for their TiO_2 counterparts. This could be the result of the higher number of hydroxyl groups present on the Al_2O_3 surface in comparison with the TiO_2 surface. Beside chemically or thermally aggressive media, abrasive solutions can damage the integrity of membranes permanently. Mechanical damage caused by abrasion or scaling due to forming crystals in highly saline solutions can lead to the rapid degradation of membranes. So far only the

mechanical degeneration of polymeric membranes due to high salt concentrations has been studied [32,33]. Due the low thickness the final layer of any asymmetric ceramic membranes could also be vulnerable to mechanical damages that could potentially compromise the selectivity of the whole membrane. Therefore, the sensitivity of symmetric and asymmetric ceramic membranes towards mechanically aggressive solutions was studied in the scope of this work. A highly concentrated suspension with the composition of a synthetic potassium mining wastewater (38.48 g $MgSO_4$ + 284.50 g $MgCl_2$ + 69.98 g NaCl + 54.13 g KCl per kg H_2O, supplied by K-UTEC AG Salt Technologies) at the saturation limit was flown through modified symmetric and asymmetric Al_2O_3 and TiO_2 membranes for up to 56 hours (discontinuous, 7 days x 8 h). The effect on the initial LEP of Al_2O_3 and TiO_2 membranes can be seen in Figure 42.

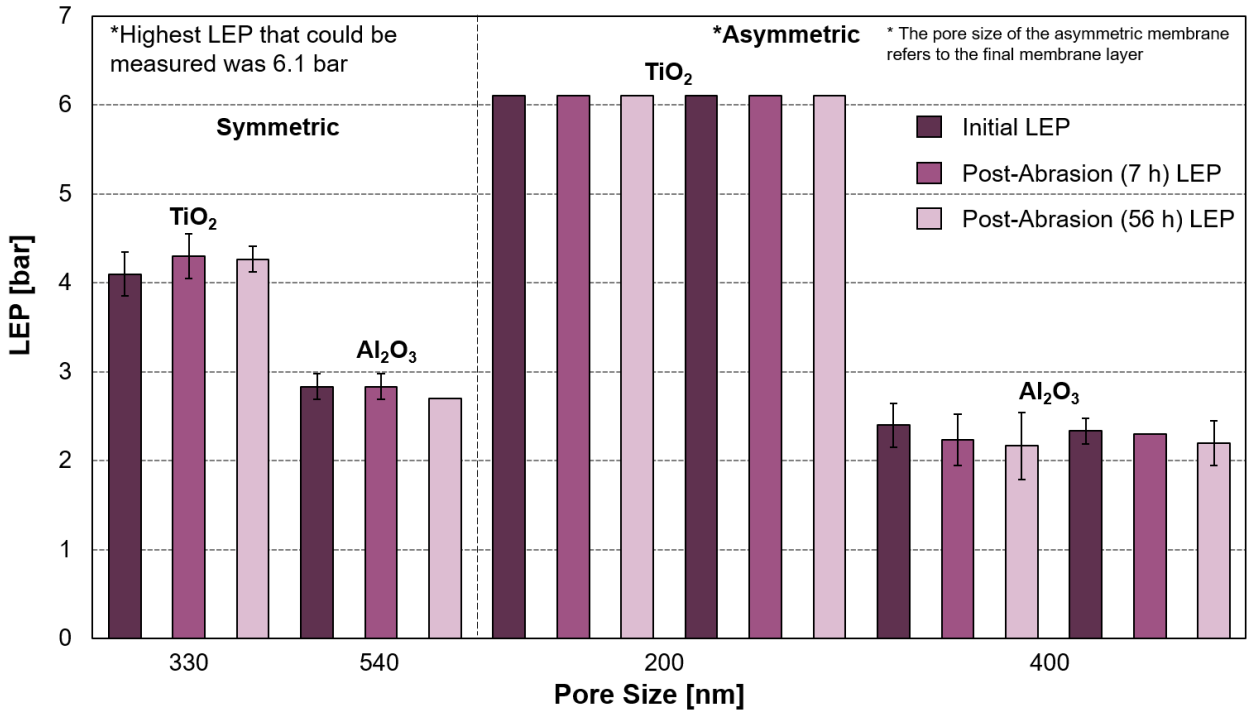

Figure 42: LEP of symmetric and asymmetric Al_2O_3 and TiO_2 membranes modified with 2 wt.% HOC in regard to the pore size before and after a abrasion test for 7 hours and 56 hours (discontinuously: 7 days x 8 h), test conditions: Feed: 38.48 g $MgSO_4$ + 284.50 $MgCl_2$ + 69.98 g NaCl + 54.13 g KCl per kg H_2O, T_{Feed}: ambient temperature, p: ambient pressure, v = 0.73 m/s (the LEP of the same membrane determined before and after the abrasion tests, minimum of 3 tests, the error bars depict the confidence intervals of the respective average value

The mechanical strain caused by the highly saline and abrasive solution did not lead to the detection of significantly reduced post-abrasion LEP for any membrane type. This observation applies to a contact time of 7 hours and 56 hours. Since the maximum LEP that could be

determined via the LEP test rig was 6.1 bar and the initial and post abrasion LEPs were all either 6.1 bar or above no unambiguous statement for the asymmetric TiO_2 membranes can be made. While symmetric TiO_2 membranes exhibited a slight increase or constant LEP subsequently to the abrasion tests the symmetric and asymmetric Al_2O_3 membranes showed the trend of a slightly declining LEP with increasing testing time. The observation made for the Al_2O_3 membranes indicates that the time frame of the test was simply too short and should be extended considerably to study the impact of abrasive solution in respect to the layer structure and integrity of modified asymmetric ceramic membranes.

4.3 Impact of Process Parameters in VMD Using Ceramic Membranes to Treat Synthetic and Real Solutions

Beside the characteristics of the membranes utilized in MD, the operational parameters define the efficiency of the process. Therefore, it is highly recommended to adjust the process parameters in accordance with the membrane characteristics, the feed properties and application targets. This includes the feed temperature, feed flow velocity and the absolute pressure on the permeate side in order to adjust the driving force and to moderate polarization effects. This chapter illustrates and discusses data on the impact of operational parameters on the performance of tubular Al_2O_3 and TiO_2 membranes in VMD treating high salinity NaCl solutions. Additionally, a synthetic leachate from the potassium mining industry (chapter 4.3.4) as well as a real RO concentrate from the dairy industry (chapter 4.3.5) was treated in VMD in consideration of process parameters such as the flow velocity and the permeate pressure. Exclusively VMD tests were conducted to research the impact of process parameters. This is because ceramic membranes benefit from the low absolute pressure on the permeate side in VMD (moderating the relatively high thermal conductivities) and the smaller mass transfer resistance due to the removal of inert gases from the membrane pores (chapter 4.2.1 to chapter 4.2.3). The VMD tests were limited to asymmetrically structured membranes because their characteristics are favorable in respect to the mass transport due to the large support pores (chapter 4.2.4).

4.3.1 Impact of the Feed Temperature and Permeate Pressure in VMD

The driving force in VMD is proportional to the feed temperature and absolute pressure on the permeate side. Temperature polarization effects that dampen the driving force are considered to be moderate due to the good thermal insulation imposed by the low absolute pressure on the

permeate side and are dependent on the membrane characteristics and other operational parameters such as the feed flow velocity and the feed salinity. The feed temperature is one of the most important process parameters due its exponential relationship between the partial water vapor pressure. To understand the relationship between the feed temperature, permeate pressure and permeate flux using ceramic membranes, asymmetric Al_2O_3 and TiO_2 membranes were tested in VMD in respect to feed the temperature ranging from 55 °C to 75 °C in dependency of the permeate pressure (range from 125 mbar to 75 mbar) using a highly concentrated feed (Figure 43).

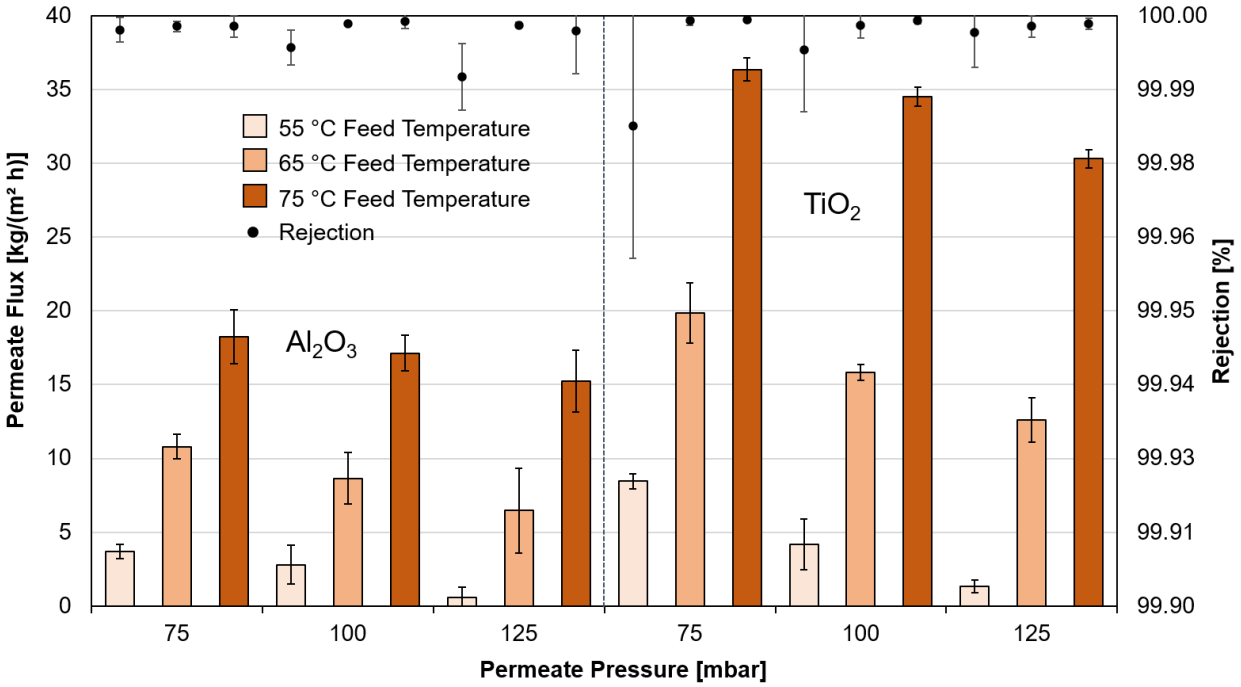

Figure 43: Permeate flux (bars) and rejection (dots) of Al_2O_3 and TiO_2 membranes (final pore size: 100 nm) in dependency of the feed temperature and permeate pressure, test conditions: Feed: 350 g NaCl/kg H_2O, $T_{Coolant}$: 0 °C, v = 1.08 m/s; minimum of 3 tests, the error bars depict the confidence intervals of the respective average value

Both membrane types showed an excellent selectivity by facilitating salt rejections greater than 99.9 %. This is remarkable since the salt concentration of the feed was close to the saturation point with 350 g NaCl per kg H_2O. The permeate fluxes determined for the TiO_2 membranes were about 50 % to 120 % higher (maximum permeate flux: 36.3 kg/(m² h)) than the permeate fluxes measured for the Al_2O_3 membrane (maximum permeate flux: 18.3 kg/(m² h)). This was not expected since the N_2 permeance for both membrane types (final pore size of 100 nm) only varied by around 20 % (Figure 31). Since the TiO_2 membrane became more competitive with the Al_2O_3

membrane (in respect to the permeate flux) with increasing feed temperatures it can be argued that the thermal conductivity of the membranes is not neglectable (differs by a factor of 2.5, chapter 4.1.1) in VMD. While the latent heat transfer is limited by the mass of the vapor transported, the heat transferred through conduction is not limited and highly dependent on the thermal conductivity of the membrane. It can be assumed that temperature polarization effects are more pronounced for Al_2O_3 membranes than for TiO_2 membranes resulting in reduced driving forces. For each membrane type a moderate and near linear increase of permeate flux with decreasing permeate pressures from 125 mbar to 75 mbar was determined. The increase of the feed temperatures from 55 °C to 65 °C led to a stronger incline in permeate flux (factor: 2.9 to 10.6) of the Al_2O_3 membrane than the further increase of the feed temperature to 75 °C (factor 1.7 to 2.4). Although the same behavior can be observed for TiO_2 membranes the effect is less pronounced. This can be explained with the lower thermal conductivity of the TiO_2 membranes that moderates stronger temperature polarization more effectively at higher feed temperatures.

4.3.2 Impact of the Feed Flow Velocity in VMD

In general, polarization effects are the major limiting factor of MD processes and are an obstacle for the use of ceramic membranes in MD due to their relatively high thermal conductivities. As mentioned before, the interfaces of a membrane utilized in MD is characterized by increased salinities due to the extraction of pure water as well as by reduced temperatures on the feed side and elevated temperatures on the permeate side due to the overall heat transported. This affects the actual driving force of the process considerably. The moderation of polarization effects and their limiting impact on the driving force can be achieved by adapting the feed flow in respect to the MD configuration, operational parameters such as feed salinity and temperature as well as to the membrane type has been widely proposed. Therefore, the effect of the flow velocity on the performance of Al_2O_3 and TiO_2 membranes, treating a highly concentrated feed with different temperatures in VMD, was studied (Figure 44 and Figure 45).

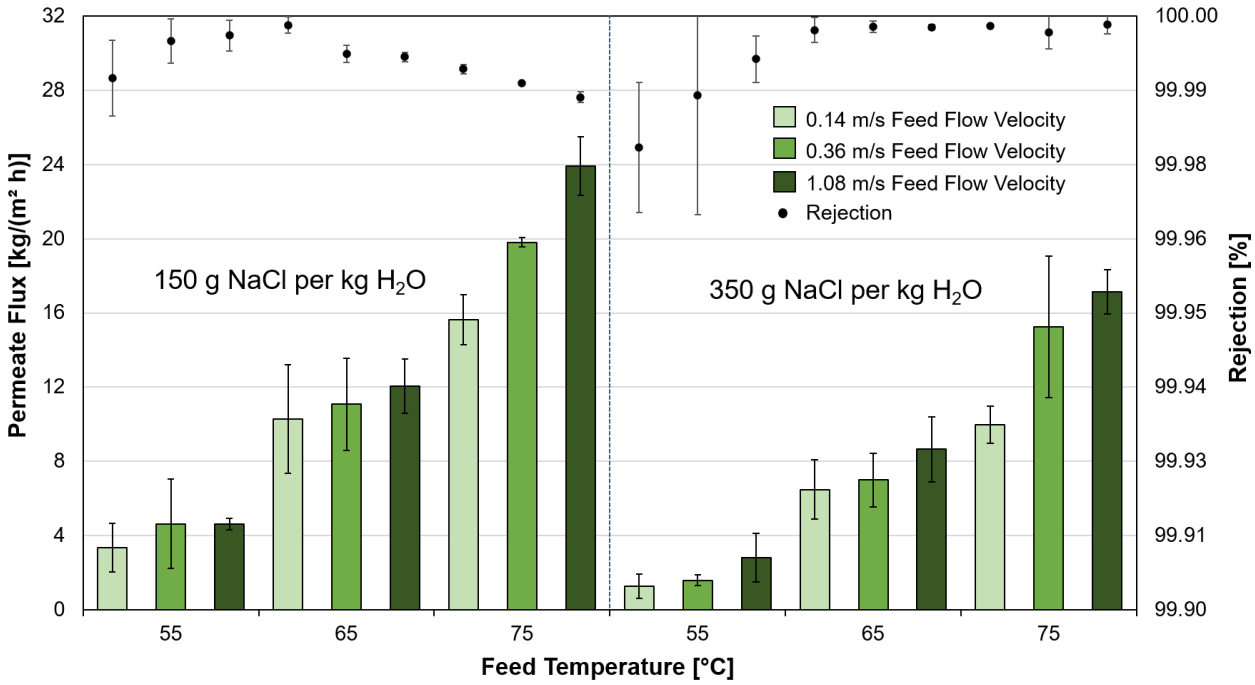

Figure 44: Permeate flux (bars) and rejection (dots) of an Al_2O_3 membrane (final pore size: 100 nm) in dependency of the flow velocity, feed temperature and NaCl concentration, test conditions: p_{abs}: 100 mbar, $T_{Coolant}$: 0 °C; minimum of 3 tests, the error bars depict the confidence intervals of the respective average value

The permeate flux decreased by a factor between 1.2 and 2.9 with the increase of the NaCl concentration from 150 g NaCl per kg H_2O to 350 g NaCl per kg H_2O. The increase of the salt concentration led to a decline of the water activity resulting in lower partial vapor pressure and reduced driving forces. Moreover, the changing of hydrodynamic conditions such as the viscosity, density and heat capacity led to a significant decline in heat transfer from the bulk stream of the feed to the interface of the membrane. This explains why the reduction of the permeate flux was stronger for lower feed temperatures (55 °C: factor from 1.6 to 2.9) than for higher feed temperatures (75 °C: factor from 1.3 to 1.6). The increase of the feed flow velocity led to an increase in permeate flux for all feed temperatures and feed concentrations but was slightly more pronounced for higher temperatures. The increase of the feed flow velocity causes increased turbulence at the membrane interface reducing the boundary layer characterized by temperature and concentration polarization. The relationship between the flow velocity, feed temperature and permeate flux is the same for both feed concentrations. The positive impact of the increased flow velocity is stronger for higher temperatures. This is because temperature polarization becomes more pronounced at higher feed temperatures increasing the positive effect of stronger turbulence at the membrane interface. It can be concluded that the adaptation of the feed flow velocity towards turbulent flow conditions using Al_2O_3 membranes in VMD, becomes more important at

higher feed temperatures whereas lower feed temperature may allow laminar flow conditions (< 0.3 m/s). For all tests excellent rejections above 99.9 % were determined.

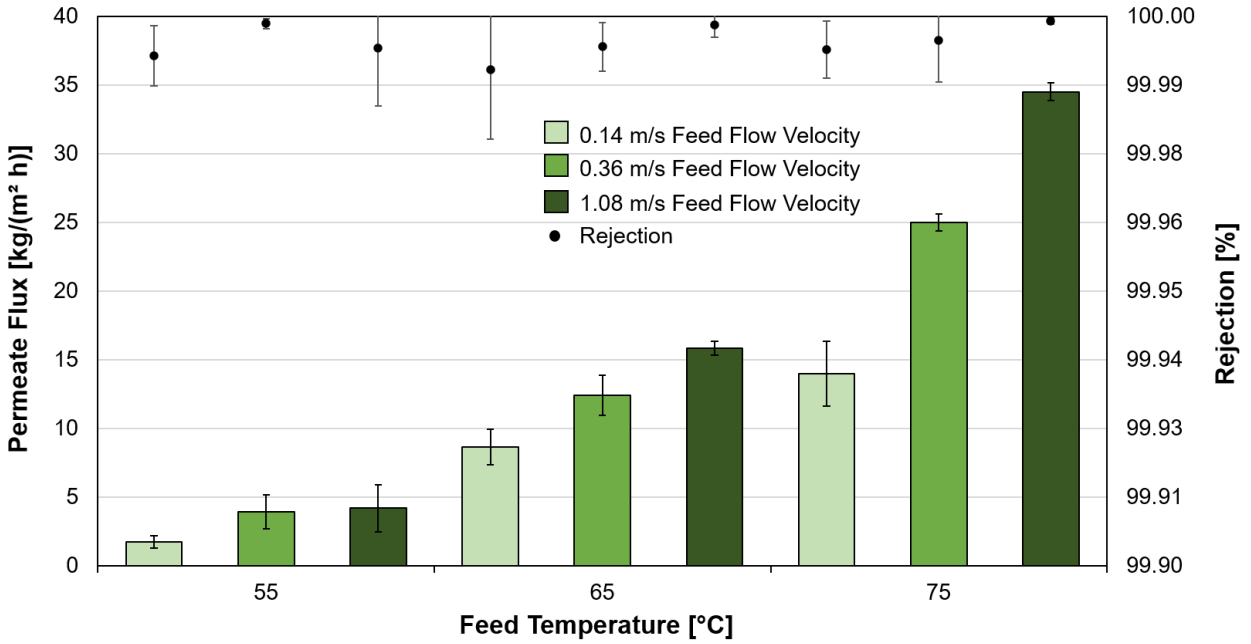

Figure 45: Permeate flux (bars) and rejection (dots) of an TiO_2 membrane (final pore size: 100 nm) in dependency of the flow velocity and feed temperature test conditions: Feed: 350 g NaCl per kg H_2O, p_{abs}: 100 mbar, $T_{Coolant}$: 0 °C; minimum of 3 tests, the error bars depict the confidence intervals of the respective average value

The TiO_2 membrane showed excellent rejections above 99.99 % for all tests conducted. The permeate fluxes were by a factor between 1.4 and 2.5 higher than the permeate fluxes of the Al_2O_3 membrane for the respective set of operational parameters using a feed concentration of 350 g NaCl per kg H_2O. The competitiveness of the TiO_2 membrane is based on the lower thermal conductivity and the slightly larger pore size of the support. However, the support pore size is by comparison of subordinate importance since it was shown that the N_2 flux for the two membrane types only differed by a factor of around 1.2 (chapter 4.1.4). Just like the Al_2O_3 membrane, the TiO_2 membrane demonstrated increasing permeate fluxes for increasing flow velocities. The incline of permeate flux over the flow velocity is significant for a feed temperature of 65 °C and 75 °C and was similarly pronounced for all feed temperatures. This observation is different to what was observed using Al_2O_3 membranes that showed a stronger dependency between feed temperature and flow velocity at higher temperatures because of the higher thermal conductivity. However, despite the considerably lower thermal conductivity of the TiO_2 membrane, the facilitation of a highly turbulent flow regime (v > 1 m/s) at high feed temperatures and high feed

concentrations is imperative. For lower feed temperatures (55 °C) the increase of the flow velocity from 0.36 m/s to 1.08 m/s did not affect the permeate flux indicating that a turbulent flow regime in the lower spectrum (~ 0.3 m/s) is sufficient for low feed temperatures. Beside the permeate flux the energy (thermal) efficiency is a relevant performance indicator for membranes applied to thermally driven lab-scale processes such as MD processes. As illustrated by Eq. 6 this parameter reflects how much of the heat that is transferred during the process is latent heat due to the vapor flux in relation to the heat transported through conduction. The energy efficiency is dependent on membrane characteristics such as the thermal conductivity, the MD configuration and process parameters. An ideal energy efficiency would result in a value of unity leading to the use of around 750 kWh_{th} of energy to vaporize 1 m³ of water (single stage process). To determine the energy efficiency in accordance with the respective tests illustrated in Figure 43 the heat loss of the feed between the module inlet and outlet was recorded. Based on the data presented in Figure 44 and Figure 45 the overall heat transfer, latent heat, heat transport via conduction and subsequently the energy efficiency was calculated for the Al_2O_3 and TiO_2 membrane in respect to the flow velocity and feed temperature (Figure 46).

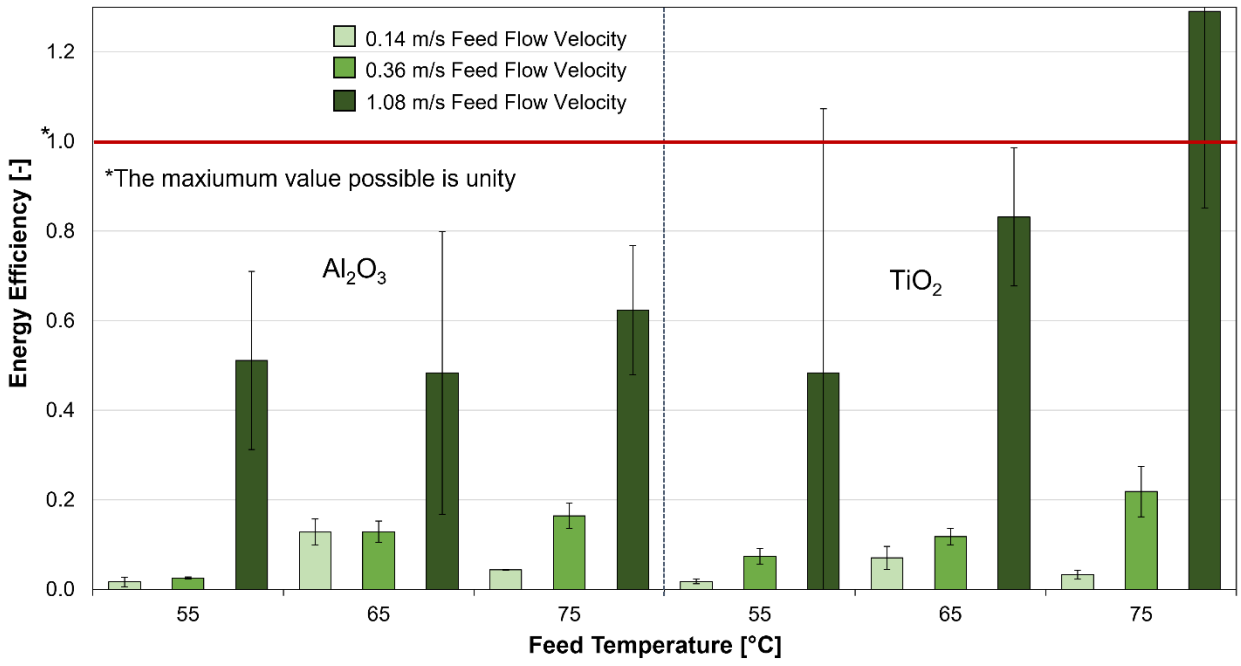

Figure 46: Energy (thermal) efficiency (unity is the maximum value possible) of Al_2O_3 and TiO_2 membranes (final pore size: 100 nm) in dependency of the flow velocity and feed temperature, test conditions: Feed: 350 g NaCl/kg H_2O, $T_{Coolant}$: 0 °C, p_{abs}: 100 mbar; minimum of 3 tests, the error bars depict the confidence intervals of the respective average value

For a single stage process the maximum (best) value that can be achieved for the energy efficiency is unity. This would indicate that all the heat that was removed from the feed was heat related to the vapor transport. The strongly pulsating peristaltic feed pump used for the test led to considerable variations in feed flow volume over the testing period resulting in strong variations of the measured temperatures of the feed before and after the membrane module. This resulted in wide error margins and in a possible over- or underestimation of the determined energy efficiencies. Therefore, the illustrated energy efficiencies must be considered with caution. Keeping that in mind, it can be stated that the energy efficiency for both membranes is very low (< 0.2) for feed temperatures of 65 °C and below at for feed flow velocities of 0.36 m/s and lower. While both membrane types showed increasing energy efficiencies with increasing feed temperatures at a low feed flow velocity (0.14 m/s) due to the increased impact of heat conduction, both membrane types showed improved energy efficiencies at higher feed temperatures at turbulent feed flow rates (0.36 m/s and 1.08 m/s). This means that the permeate flux of both membrane types increased disproportionally in comparison with the heat transferred via conduction in turbulent feed flow regimes. This trend was more pronounced for the TiO_2 membrane. The TiO_2 membrane moderated the heat transfer processes due to conduction at high feed temperatures (moderating temperature polarization) more effectively than the Al_2O_3 membrane due to its lower thermal conductivity (Figure 23). Therefore, in respect to the energy efficiency it does not make a difference whether a Al_2O_3 or TiO_2 membrane is utilized in low to medium hot environments, but it is highly recommended to use a TiO_2 membrane for feed solution that are hotter than 60 °C. In addition, the facilitation of a turbulent feed flow regime is beneficial for all feed temperatures and both membrane types.

4.3.3 Impact of the Salt Concentration in VMD

As mentioned before, conventional desalination processes are not suitable for the treatment of highly concentrated salt solutions due to limitations imposed by the osmotic pressure and corrosion effects. Membrane Distillation is believed to be able to overcome these limitations and enable the water extraction from saline solutions up to the saturation point. However, state of the art polymeric membranes utilized in MD (for instance thin PTFE foil on PP backing structure) may be too fragile to cope with abrasive solutions. Due to their mechanical stability, ceramic membranes could pose an attractive alternative for the further concentration of highly saline solutions up to the saturation point and enable zero-liquid-discharge applications. TiO_2 membranes with a final pore size from 100 nm to 400 nm were applied in VMD for the treatment

of moderate and highly saline solutions to study their performance in respect to increasing salt concentrations (Figure 47).

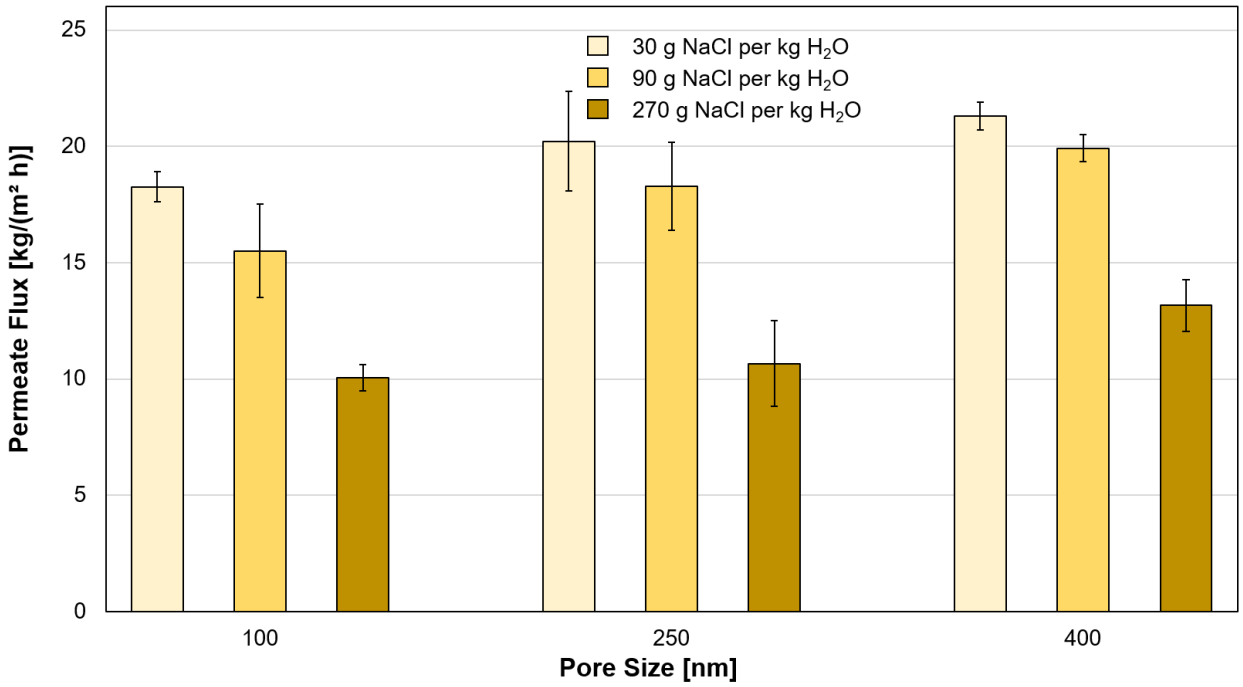

Figure 47: Permeate flux (bars) of TiO_2 membranes in dependency of the membrane pore size (final pore size: 100 nm, 250 nm and 400 nm) and feed concentration; test conditions: T_{Feed}: 60 °C, p_{abs}: 100 mbar, $T_{Coolant}$: 0 °C; v = 0.72 m/s, minimum of 4 tests, the error bars depict the confidence intervals of the respective average value

The permeate quality was excellent with salt rejections determined above 99.99 % for all feed concentrations and all membrane pore sizes. The TiO_2 membranes exhibited permeate fluxes between 18 kg/(m² h) at a pore size of 100 nm and 21 kg/(m² h) at a pore size of 400 nm for a salt concentration of 30 g NaCl per kg H_2O (~seawater salt concentration). When the NaCl concentration of the feed solutions was increased by a factor of three to 90 g NaCl per kg H_2O (only viable for high pressure reverse osmosis) the permeate flux declined between 7 % and 15 %. By further increasing the salinity to 270 g NaCl per kg H_2O the permeate flux decreased by another 33 % to 41 % leading to a minimum permeate flux of 10 kg/(m² h) for a membrane pore size of 100 nm and 13.2 kg/(m² h) at membrane pore size of 400 nm. As mentioned before, the impact of the final pore size of asymmetric ceramic membranes that are used in VMD processes is limited. It is highly recommended to choose the smaller pore size for the treatment of saline solutions in VMD. The increasing salt concentration in the feed affects the driving force in two ways. Firstly, the dissolved salts in the feed lowers the water activity which causes a reduction of the partial

vapor pressure. The impact of this effect on the permeate flux is moderate. This becomes apparent if the water activity is calculated (Eq. 23 [153] (chapter 2.5.1)) for the tested NaCl solutions. The increase of the salinity from 30 g NaCl per kg H_2O to 90 g NaCl per kg H_2O leads to a decrease of the water activity by 3.5 % whereas the further increase of the salinity from 90 g NaCl per kg H_2O to 270 g NaCl per kg H_2O causes an additional reduction of water activity of 13 %. Therefore, the reduction of the permeate flux is more than twice as sharp as could be expected from the change of water activity. The second factor that led to a reduction of the driving force is the change of the hydrodynamic conditions of the feed solutions with increasing salinities. This results in a reduced heat transfer from the bulk solution of the feed to the membrane interface causing more pronounced temperature polarization effects. For instance, the increase of the salinity from 30 g per kg H_2O to 90 g NaCl per kg H_2O causes a reduction of the thermal conductivity of the feed by ~10 % [190]. However, this effect can be moderated by adjusting the feed flow velocity (increase of turbulence results in a better mixing of the feed) in respect to the salinity levels of the feed. The results shown in Figure 47 and chapter 4.3.2 illustrate that despite high feed salinities relatively high permeate fluxes can be achieved if the feed flow velocity is adjusted accordingly. To study the performance of asymmetrically structured ceramic membranes in respect to increasing salinities a highly concentrated feed solution (200 g NaCl per kg H_2O) was further concentrated approaching the saturation point using a Al_2O_3 membrane (pore size: 100 nm) in VMD (Figure 48).

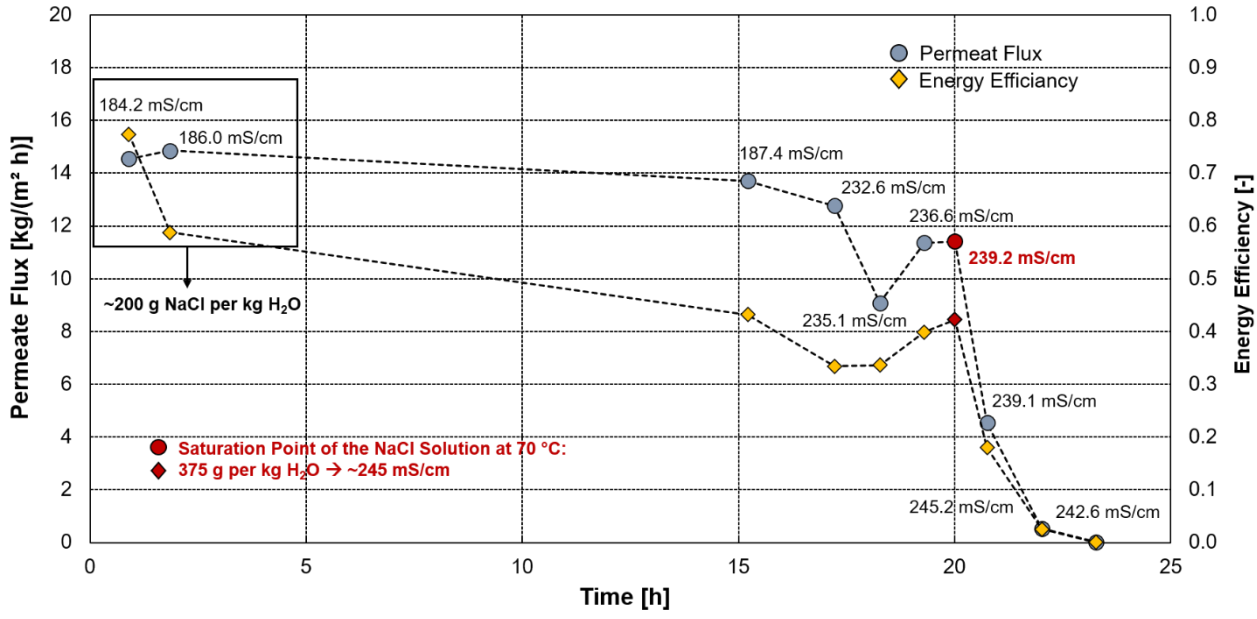

Figure 48: Permeate flux (blue dots) and energy efficiency (yellow) of an Al_2O_3 membrane (final pore size: 100 nm) in dependency to the salt concentration (initial: 200 g NaCl per kg H_2O, end: saturation point: ~375 g NaCl per kg H_2O at the given feed temperature); p_{abs}: 100 mbar, $T_{Coolant}$: 2 °C; v = 0.72 m/s, T_{Feed}: 70 °C, continuous testing over 24 hours

The permeate quality was excellent with rejections determined above 99.99 % for all feed concentrations. The rejection for the last point of measurement could not be quantified due to the small amount of permeate produced at that feed concentration. At the initial feed salinity of around 200 g NaCl per kg H_2O a maximum permeate flux of 14.8 kg/(m² h) was determined. With increasing feed salinity (the permeate was discarded) approaching the saturation point of NaCl solutions at 70 °C (marked by the red dot) the permeate flux decreased by around 23 %. Up to this point the moderate reduction of permeate flux can be attributed to the lower water activity and the impaired heat transfer with increasing salinities. Even at high concentrations with feed salinities nearing the saturation point permeate fluxes of 10 kg/(m² h) and above were determined. Near the saturation point (~240 mS/cm / 375 g NaCl per kg H_2O) crystallization at the membrane interface occurred which led to a rapid but reversible decline of the permeate flux (at the given feed flow velocity of 0.72 m/s) to near zero within 4 hours. This leads to the conclusion that ceramic membranes are suited for the treatment of highly saline solutions (even close to the saturation point) if crystallization is avoided. The initial energy efficiency of the Al_2O_3 was determined at 78 % for an initial feed concentration of 200 g NaCl per kg H_2O. The energy efficiency displays a similar dependency in respect to the increasing salinity as the permeate flux. This does not come as a surprise since the latent heat is proportional to the vapor flux which in return is highly dependent on the salinity of the feed. The more vapor is being transported, the better the energy efficiency provided that the heat transfer through conduction is not affected proportionally.

4.3.4 Treatment of a Highly Saline Leachate Using Ceramic Membranes in VMD

Leachates from the mining industry can severely affect the quality of the receiving water bodies. A prominent example is the contamination of the River Werra in Germany with highly saline leachates from the potassium mining industry [191]. Ceramic membranes utilized in VMD could enable the treatment of highly saline leachates and contribute to prevent the pollution of natural water bodies caused by insufficiently treated mining waste waters. To evaluate the performance of ceramic membranes in this environment, a synthetic saline solution close to saturation point was created with the same composition as a real leachate from the potassium mining industry and further concentrated using a single channel asymmetric Al_2O_3 membrane (Figure 49).

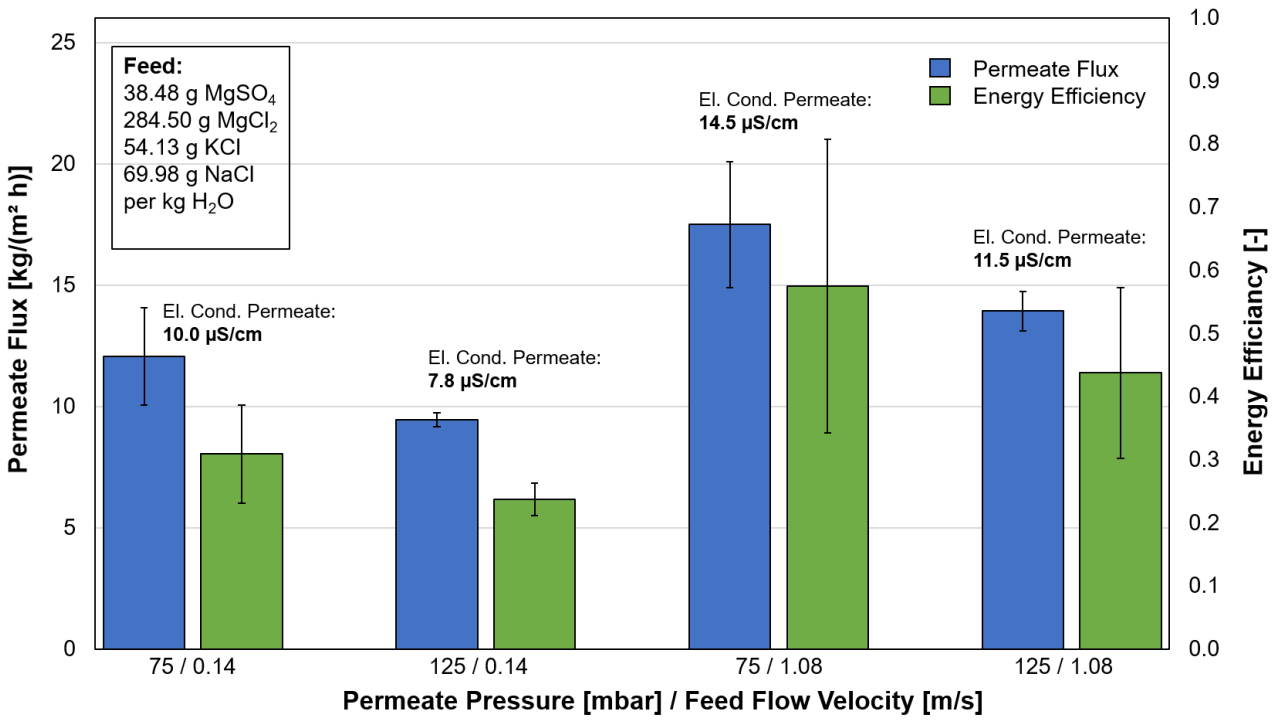

Figure 49: Permeate flux (light grey bars) and energy efficiency (dark grey bars) of an Al_2O_3 membrane (final pore size: 100 nm) in dependency of the flow velocity and permeate pressure; test conditions: Feed: 38.48 g $MgSO_4$ + 284.50 g $MgCl_2$ + 69.98 g NaCl + 54.13 g KCl per kg H_2O, T_{Feed}: 75 °C, $T_{Coolant}$: 15 °C; minimum of 3 tests, the error bars depict the confidence intervals of the respective average value, fresh water extracted was poured back into the feed container after each test

Based on the composition and temperature of the feed (75 °C), 0.055 kg H_2O per kg mixtures can theoretically be extracted from the feed until the saturation point is reached and crystallization can occur. The permeate extracted from the highly saline leachate using a Al_2O_3 membrane in VMD showed excellent permeate qualities with electric conductivities below 15 µS/cm in all tests. Despite using a near saturated saline feed, permeate fluxes of up to 17.5 kg/(m² h) were determined. The minimum permeate flux determined was around 10 kg/(m² h) for a permeate pressure of 125 mbar and feed flow velocity of 0.14 m/s (laminar region). This means that even at relatively high permeate pressures and low feed flow velocities adequate permeate quantities can be produced if high feed temperatures (in the case of this study: 75 °C) can be applied to the process. The permeate flux significantly declined (~25 %) when the permeate pressure was increased from 75 mbar to 125 mbar for both feed flow velocities. The decline in permeate flux was not as pronounced as could be expected from the theoretical reduction of the driving force in respect to the increase of the permeate pressure. The increase of the feed flow velocity from laminar to turbulent flow conditions led to a significant increase in permeate flux (~45 %) due to the partly compensation of polarization effects. The extent of this effect was the same for both

permeate pressures. The best energy efficiency was determined for a flow velocity of 1.08 m/s and a permeate pressure of 75 mbar at 60.1 %. This was achieved by moderating the polarization effects with an increased turbulence at the membrane interface and the improved thermal insulation imposed by the low pressure. However, in consideration of this value, more than 1000 kWh of energy would still be required to produce 1 m³ of permeate (ideal value is ~750 kWh per m³ for a single stage process). The energy efficiency showed the same behavior as the permeate flux in respect to the flow velocity and permeate pressure and was determined to be as low as 25 % for a feed flow velocity of 0.14 m/s and a permeate pressure of 125 mbar. If high feed temperatures are applied in VMD, the adaptation of the feed flow velocity and permeate pressure should be adjusted accordingly. Additionally, the use of ceramic materials with relatively low thermal conductivity is recommended.

4.3.5 Treatment of a RO Concentrate from the Dairy Industry Using Ceramic Membranes in VMD

Despite the decline of the number of publications on MD processes treating food processing waste waters as illustrated in the introduction section the industry offers an interesting spectrum of saline waste waters that could be further concentrated via MD processes maximizing freshwater extraction and enabling resource recovery. The potential utilization of waste heat accruing during food processing could render any MD process even more attractive. To evaluate the suitability of ceramic membranes applied to MD processes to treat food processing waste waters, a regional producer of dairy products has provided a real mixture generated during his manufacturing process for this study. This real solution is a RO concentrate composed of around 35 g salts (containing the following ions: Na^+, Cl^-, K^+, Mg^{2+}, PO_4^{3-}, detailed composition was not further specified by producer) and 10 g organic substances (mainly humic substances, detailed composition was not further specified by producer) with an electric conductivity of 43.8 mS/cm. The solution was treated using a Al_2O_3 and TiO_2 membrane with a final pore size of 100 nm in VMD (Figure 50).

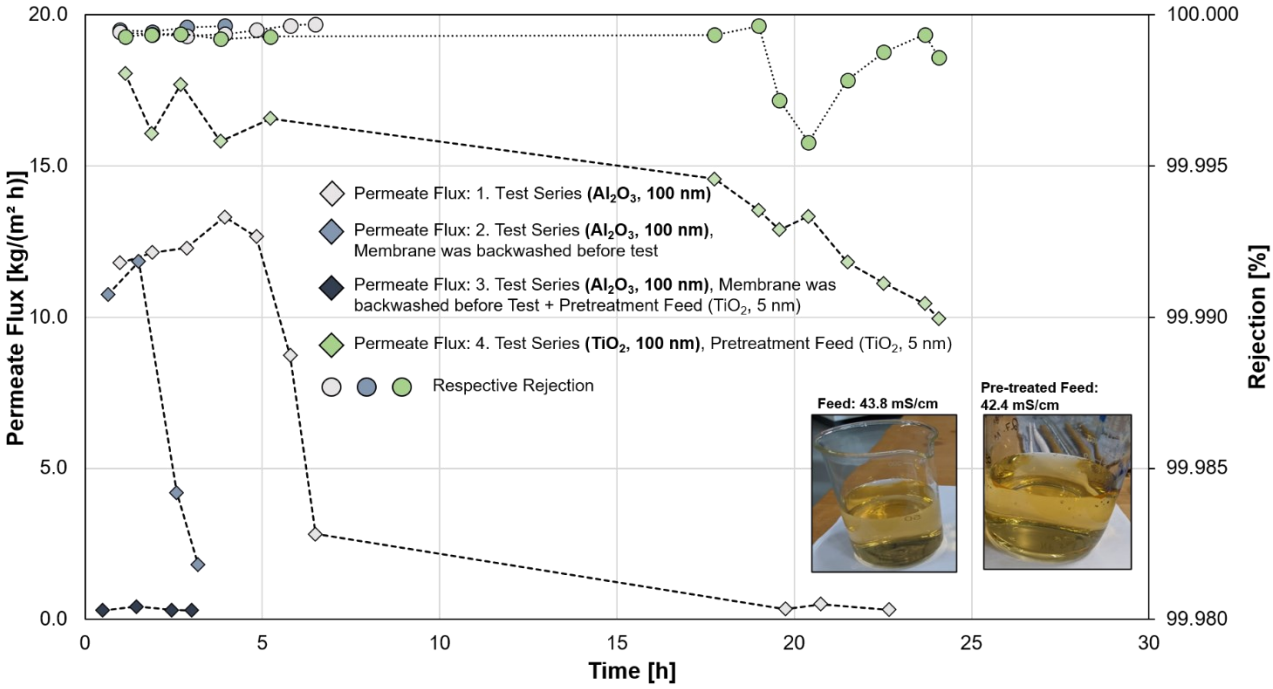

Figure 50: Permeate flux (diamond shapes) and salt rejection (circles) in respect to the testing time (cumulative testing period, permeate was poured back into the feed container) test conditions: Feed: ~35 g salts (NaCl, K, Mg_2 and P) + ~10 g humic substances per kg H_2O, T_{Feed}: 60 °C, p_{abs}: 100 mbar, $T_{Coolant}$: 0 °C; v = 0.72 m/s, the permeate was poured back into the feed container

The first test series was conducted using a Al_2O_3 membrane without pretreating the saline feed containing organic matter (responsible for the yellow coloration of the feed). The rejection determined from permeate samples was excellent (> 99.99 %) with permeate qualities between 10 µS/cm and 50 µS/cm. The permeate flux was in the range between 11.8 kg/(m² h) and 13.2 kg/(m² h) for the first 5 hours of the testing period and declined over a period of 18 hours to almost zero indicating severe pore blocking. At this point, the little amount of permeate produced did not allow the measurement of the electric conductivity of the permeate anymore. The strong decline of the permeate flux can be attributed to fouling processes. Fouling can affect membrane performance in different ways, for instance, through increase of temperature polarization due to an increased thermal resistance, decrease of the active membrane area as well as increased diffusion distances [192]. The exact composition of the feed mixture is not known but considered to be diverse allowing different mechanisms of fouling to occur that cannot be determined in the scope of this study. Each component of a highly complex dairy product solution uniquely interacts with the membrane surface and unique interactions with other components of the feed solution including absorbed solutes are to be expected as well [193–196]. Because humic substances can exhibit different properties the binding to the hydrophobic surface as well as complex formation

can also not be disqualified. After the first test series the Al_2O_3 membrane was backwashed at a pressure above the LEP for about 30 min and then dried in an oven at 120 °C for approximately 16 hours. This membrane was used for the second test series (light blue diamond shapes) which showed a good initial permeate around the same values as the initial flux determined for the first test series. After 90 minutes testing time the permeate flux declined rapidly and the test was aborted. It can be concluded that the cleaning of the membrane did free the pores from the blockage caused by the fouling but did not remove the fouling layer from the rest of the membrane surface. Guillen et al. 2014 [197] stated that backwashing is the most popular fouling mitigation method but may not be as effective as required. This caused the pore blockage to arise relatively quickly again after starting the VMD test. The third test series (dark blue diamond shapes) was done with the same membrane (after backwashing) on a pretreated feed solution using a TiO_2 UF membrane with a pore size of 5 nm. The backwash and the pretreatment did not increase the performance and only strongly reduced permeate fluxes could be determined indicating that the membrane properties were not sufficiently restored by the backwashing and drying procedure. Another test series was conducted using a TiO_2 membrane with a pore size of 100 nm (green diamond shapes). For this test series the feed was also pretreated using a 5 nm TiO_2 membrane. The UF filtration did not change the coloration of the feed and resulted in a decline of electric conductivity of around 3 %. Considering this and the size range of humic substances (4.7 nm to 33 nm [198]) it is very likely that most humic molecules are still present in the feed solution. As can be seen in Figure 50 the initial permeate flux of the TiO_2 membrane was determined to be around 16 kg/(m² h) and remained relatively stable around that value for five hours. As stated before, the higher permeate flux (in comparison with the Al_2O_3 membrane) is mostly based on the larger support pore size and lower thermal conductivity of the TiO_2 membrane. After five hours the permeate flux started to decline over a period of nearly 20 hours to around 10 kg/(m^2 h) indicating a slower fouling processes as present for the Al_2O_3 membrane. Either the humic substances react differently with the material of the TiO_2 membrane resulting in lower fouling processes or the Al_2O_3 membrane used for the test series one to three was already too affected by the fouling process that the potential positive impact of the pretreatment of the feed was not shown by the third test series.

4.4 Mass Transfer Modelling Through Asymmetric Ceramic Membranes

In this chapter, experimentally determined permeate fluxes of TiO_2 membranes were used to assess the validation of the generally accepted VMD mass transfer model (based on the DGM described in chapter 2.5) for asymmetric ceramic membranes. Furthermore, deficiencies of the model in respect to the predicted mass transfer of ceramic membranes were identified and the model adapted accordingly using correction factors validated for the local scope (the scope of process parameters and membrane properties that were investigated experimentally). This was done to establish a modelling basis in respect to the mass transfer through ceramic membranes that can be extended in future works and eventually facilitate the investigation of the impact of membrane properties and process parameters that cannot easily be manufactured or realized in practice. For instance, this could guide the membrane optimization and process development without extensive prototype production or test rig construction that enable extreme parameter spectra. As stated before, the mass transfer modelling was limited to the VMD configuration due to the complex wetting behavior of modified asymmetric ceramic membranes in DCMD mode (cooling liquid infiltrates the support pores to a various extent for different membranes) as well as the fact that VMD is more suited than DCMD for ceramic membranes. N_2 permeance data allowed the calculation of the tortuosity of each membrane layer of asymmetrically structured TiO_2 single channel membranes based on Eq. 37 (Table 8).

Table 8: Tortuosity values derived using the DGM for the specific TiO_2 layers obtained using N_2 permeance data as well as data on the thickness, porosity and pore size of the membrane layer

Membrane	Layer, Pore Size	Tortuosity [-]
TiO_2 (final pore size: 100 nm)	Support, 4.6 µm	**2.87**
	Intermediate Layer, 0.8 µm	**2.62**
	Intermediate Layer, 0.25 µm	**1.56**
	Final Layer, 0.1 µm	**2.16**
TiO_2 (final pore size: 250 nm)	Support, 4.6 µm	**2.87**
	Intermediate Layer, 0.8 µm	**2.62**
	Final Layer, 0.25 µm	**1.25**
TiO_2 (final pore size: 400 nm)	Support, 4.6 µm	**2.87**
	Intermediate Layer, 0.8 µm	**2.62**
	Final Layer, 0.4 µm	**1.70**

In doing so, the asymmetric TiO_2 single channel membranes were fully characterized in respect to their morphological parameters. A superposition of Knudsen diffusion and viscous flow was considered for all mass transfer calculations based on the Knudsen number calculated in respect to the membrane pore size and operational conditions and the low absolute pressure applied to the permeate side.

The following illustration (Figure 51) shows the calculated (based on the VMD model in its natural form) and the experimentally determined permeate fluxes in respect to the feed temperatures and feed flow velocity for TiO_2 membranes with a final pore size of either 100 nm or 400 nm.

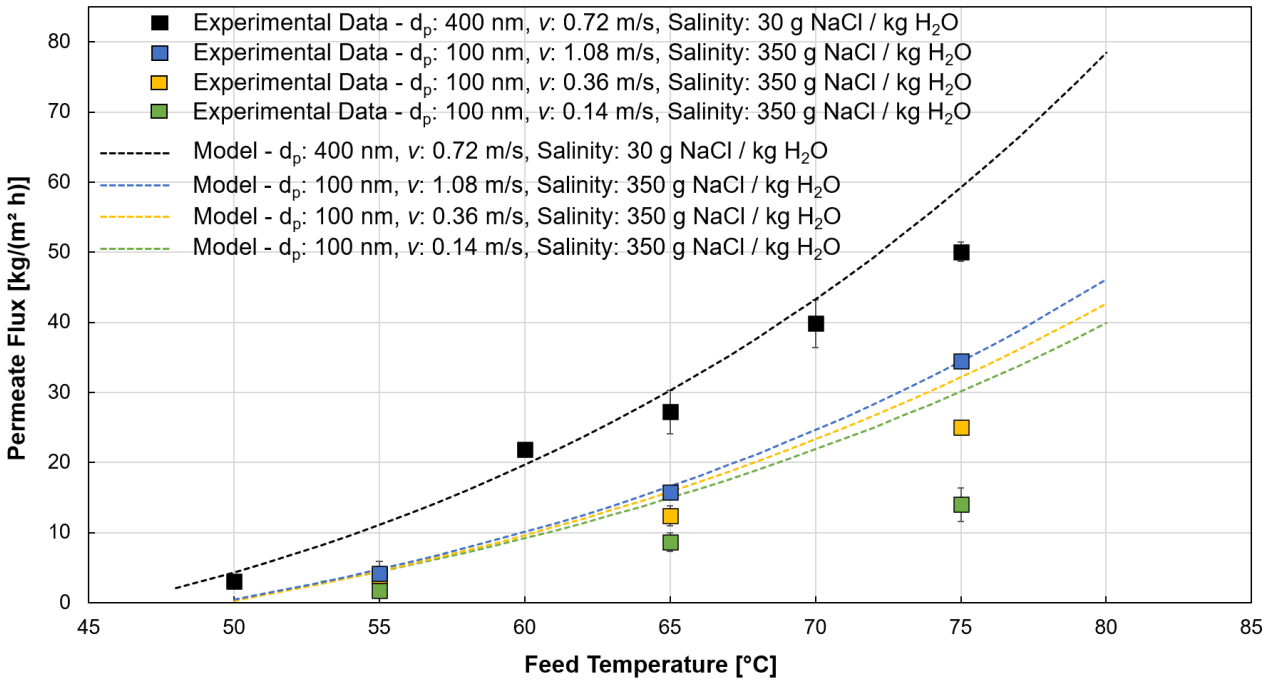

Figure 51: Simulated (dotted lines) and measured (squares) fluxes of different asymmetric TiO_2 membranes in respect to the feed temperature under variation of the flow velocity, test conditions: p_{abs}: 100 mbar, $T_{Coolant}$: 0 °C; minimum of 3 tests, the error bars depict the confidence intervals of the respective average value

It can be stated, that the modelled permeate fluxes were in good agreement with the measured flux values at a high feed flow velocity of 1.08 m/s (blue dotted line and squares). The lower the feed flow velocity and the higher the feed temperature the more pronounced are the deviations between calculated and measured fluxes (max. deviation of 51 %). The experimentally obtained permeate fluxes showed a near linear dependency to the feed temperature at low feed flow velocities (yellow and green data set) while the modelled data demonstrates a non-linear relationship as suggested by the Antoine equation (Eq. 21) and considered by the VMD model.

This observation led to the conclusion that the VMD model in its natural form underestimates polarization effects leading to an overestimation of the partial water vapor pressure (= overestimation of the driving force) at the membrane interface on the feed side. The impact of polarization effects is getting more pronounced with increasing feed temperatures and decreasing feed flow velocities leading to gradually increasing deviations between the model and the measured permeate fluxes. While the VMD model considers temperature and concentration polarization effects (caused by the vapor transport) using experimentally obtained data and the specific semi-empirical relationships directly, the heat transport via conduction is only considered indirectly and inadequately while crystallization effects are not considered at all. One possible reason for the underestimation of temperature polarization effects by the VMD model (heat transport through conduction is not considered) is the fact that polymeric membranes are less affected by the heat transfer through conduction due to their low thermal conductivities (more than a magnitude lower than the thermal conductivities of ceramic membranes, Figure 23) and the fact that the VMD model is typically used to model the mass transfer through polymeric membranes. As described by the Equation 3 ($J = B_m \Delta p_m$) the permeate fluxes modelled were based on a term that describes the resistance to the mass transfer imposed by the membrane (B_m, Eq. 33) multiplied with the partial pressure difference across the membrane acting as the driving force (Δp_m). While the underestimation of polarization effects did not require the adjustment of the resistance term B_m, the driving force term Δp_m had to be adapted. This was done by lowering the temperature at the membrane interface on the feed side (serves as an input parameter for the calculation of the partial vapor pressure at the membrane interface, Eq. 21) using correction factors CF [-] that are gradually more pronounced for increasing feed temperatures and decreasing feed flow velocities:

$$T_{m,f,\,corrected,i} = T_{m,f,i} \cdot CF_i \tag{39}$$

with $T_{m,f,\,corrected,i}$ as the corrected feed temperature at the membrane interface at the index (i) [K], $T_{m,f,i}$ as the initial temperature at the membrane interface on the feed side at the index (i) [K]. CF_i can be calculated as follows:

$$CF_i = \frac{T_{m,f,0}}{T_{m,f,0} + ((i-1) \ * 0.0319 v^{-1.413})} \tag{40}$$

$$i = (T_{m,f,i} - T_{m,f,0})(\frac{1}{K}) \quad (41)$$

With $T_{m,f,0}$ as the lowest feed temperature at the interface at the membrane considered for the calculations [K] and v as the feed flow velocity [m/s]. ΔT was chosen to be 1 K. The term $0.0319v^{-1.413}$ has the dimension of the unit Kelvin and defines how strongly the correction factor increases with increasing feed temperatures. This function was derived via an iterative approach and curve fitting representing the exponential relationship between the flow velocity and the temperature increments ($\Delta T = 0.0319v^{-1.413}$) that were used to calculate the correction factor for a specific feed temperature. The following illustration (Figure 52) shows the calculated flux values (based on the integration of the correction factor as described above) and the experimentally determined permeate fluxes in respect to the feed temperatures and feed flow velocities for TiO_2 membranes with a final pore size of either 100 nm or 400 nm.

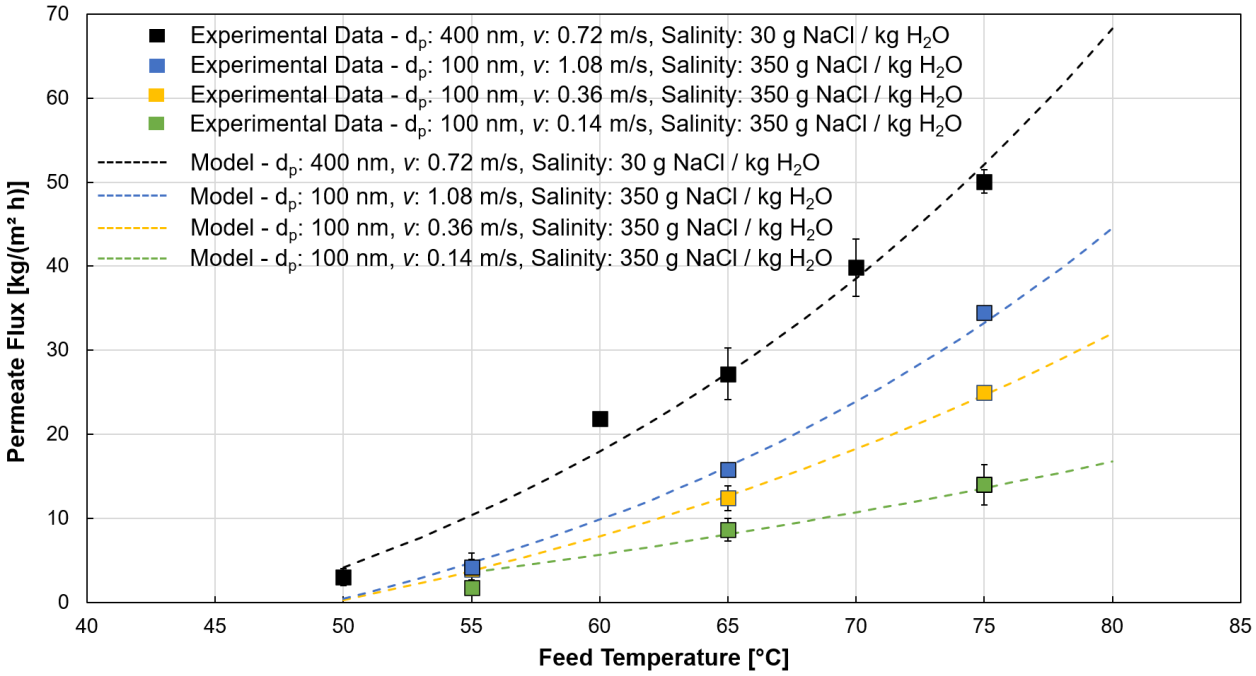

Figure 52: Simulated (dotted lines) and measured (squares) permeate fluxes of asymmetric TiO_2 membranes in respect to the feed temperature under variation of the flow velocity and in consideration of a correction factor (Eq. 40), test conditions: p_{abs}: 100 mbar, $T_{Coolant}$: 0 °C; minimum of 3 tests, the error bars depict the confidence intervals of the respective average value of the experimentally determined permeate flux

The inclusion of a correction factor that gains influence with increasing feed temperatures as well as decreasing flow velocities (accounting for increasingly stronger polarization effects) resulted in

the dampening of the modelled curves leading to excellent agreements with all the measured values. The dampening of the modelled data with increasing feed temperatures in respect to the feed flow velocity led to the modelled curves showing the same near linear trend as the measured values at relatively low flow velocities (0.36 m/s and 0.14 m/s). Although the integration of a correction factor based on the methodology described above showed excellent results for different feed concentrations (30 g NaCl per kg H_2O vs 350 g NaCl per kg H_2O) and membrane pore sizes (100 nm vs 400 nm) the validity of this approach is limited to the local scope (e.g. flow velocities in the range of 0.14 m/s to 1.08 m/s and feed temperatures from 50 °C to 80 °C). No reliable statement can be made on the validity of this approach beyond the local scope. In conclusion, the accepted VMD model based in the DGM predicts the mass transfer through asymmetric ceramic membranes in good accuracy for relatively low feed temperatures and high feed flow velocities even at high feed concentrations. This was achieved by calculating the mass transport resistance for each layer separately (up to four layers) and by subsequently combining the layer resistances in series to an overall membrane resistance. Prerequisite for this approach was the accurate characterization of the morphology of each membrane layer using several characterization methods which made the use of the tortuosity as a calibration parameter no longer necessary. However, it can be stated that the VMD model does not sufficiently consider polarization and crystallization effects and must be extended using a correction factor that is gradually more pronounced for higher feed temperatures and dependent on the flow velocity. To achieve the adaptation of the VMD model with a universal validity the unique form of ceramic pores (slot-shaped) as well as the pore size distribution should be considered. The consideration of large confidence intervals for the simulation could possibly further improve the model. The average values of experimentally obtained data such as permeate flux and N_2 flux served as an input for model critical semi-empirical equations. By considering the confidence intervals of specific average values (especially if large confidence intervals are present) the simulated data could be derived as a range instead of single values. Additionally, in-depth information on the boundary layer formation (polarization effects) in respect to a wide variety of membrane properties and process parameters is required to accurately determine the driving force for the process. This exceeds the scope of this work but should be considered for subsequent research activities.

4.5 Performance Evaluation of Ceramic Membranes in MD Processes and an Approach to Membrane Optimization

The results presented in this study indicate that ceramic membranes are competitive with polymeric membranes in VMD but underperform in respect to polymeric membranes in DCMD. For instance, Safavi et al. 2009 [199] reported permeate fluxes (11 kg/(m² h)) using PP membranes in VMD (lab-scale) that were in the same range as the permeate flux achieved with TiO_2 membranes (~ 9 kg/(m² h)) tested at similar feed concentrations and lower driving forces (T_{Feed}: 55 °C, $P_{Permeate}$: 75 mbar) for this study. In contrast permeate fluxes reported for PTFE membranes in DCMD (Feed: 35 g salts per L H_2O, T_{Feed}: 60 °C, $T_{Coolant}$: 20 °C, turbulent flow regime) were by a factor 5.5 to 6.5 higher than the permeate fluxes achieved with TiO_2 membranes in DCMD at similar process conditions (chapter 4.2.1) reported in this work [200]. These findings are partly supported by the literature stating that hollow fiber membranes made of Al_2O_3 and β-Sialon outperform state of the art hollow fiber and flat sheet polymeric membranes in DCMD and VMD under similar test conditions (lab-scale) and that ceramic membranes showed higher normalized permeate fluxes (by a factor of 1.6 to 21.4) than the polymeric counterparts made of PP, PTFE, PVDF or PVC [36].

Generally, it is argued that ceramic membranes are not competitive compared to polymeric membranes in MD due to several reasons such as the lower porosity, higher thermal conductivity, hydrophilic surface characteristics and higher production costs. This is the reason why ceramic membranes are mostly promoted as the better alternative to polymeric membranes for the treatment of aggressive environments that are too extreme for state-of-the-art polymeric membranes. This approach is still the most likely to help ceramic membranes succeed in MD processes although the in-depth assessment of the limitations of polymeric membranes was not part of this work. However, considering the good performance of ceramic membranes (permeate flux and selectivity) presented in this work it can also be argued that ceramic membranes could pose as an adequate solution for less extreme environments. This means that the optimization of ceramic membranes should focus on the improvement of the stability and the cost-efficiency of ceramic membranes. But even, if only one of these targets can be met (either improvement of the stability or improvement of their cost-efficiency of ceramic membranes) ceramic membranes can find their place in commercial MD applications. In respect to the results presented in chapter 4.2.5 and chapter 4.3 it can be stated that ceramic membranes and their modified surfaces are mechanically robust enough (symmetrically and asymmetrically structured membranes) to cope with highly saline and abrasive environments. The chemical stability towards extreme pH values is less distinct. For instance, highly acidic environments greatly affected the LEP of modified

ceramic membranes. The only membrane type stable enough to withstand this environment were symmetrically structured ceramic membranes modified with a fluorinated agent. Consequently, specific feed chemistry and membrane types require the identification of the most suitable hydrophobic agent. Thereby, not only the stability of the functionalized surface is of importance but the extent of the initial hydrophobicity. The stronger the initial hydrophobicity (quantifiable using the free surface energy, contact angle or LEP) the better the shielding of the membrane surface from aggressive components dissolved in the aqueous feed. The amount of hydroxyl groups available on the membrane surface may have an impact as well and should be considered. If the surface modification is adjusted (type, concentration and grafting procedure) in respect to a specific feed and membrane type many types of aggressive (waste) waters can be treated using ceramic membranes in VMD. Some examples are:

- Produced Waters
- Concentrated Brines
- Aqueous solutions close to point of crystallization in general and in combination with crystallization processes
- Extraction of aggressive components from aqueous media, e. g. ammonia, acids
- Food industry if the aggressive cleaning of membranes is required

The second approach in respect to the optimization of ceramic membranes puts emphasis on the improvement of their cost-efficiency. Even though it can be concluded that state-of-the-art ceramic membranes can achieve similar mass transfer rates as polymeric membranes in VMD (+ superb rejections) this is only one parameter required to assess the overall competitiveness of ceramic membranes for MD applications not characterized by harsh environments. In addition to the mass transfer of ceramic membranes, the cost-efficiency includes their capital cost (in consideration of manufacturing costs, lifespan and stability) and energy efficiency. While it is argued that ceramic membranes can be considered competitive with polymeric membranes in regard to their capital costs (despite their higher manufacturing cost) due to their superb stability and long lifespans [116] there is little scientific data to support that assumption in respect to MD applications. However, it is important to note that the capital costs related to MD processes (e. g. membranes costs, system components) are of minor importance compared the cost of the thermal energy needed to drive the MD process (if low-cost energy sources or efficient heat recovery systems cannot not be applied within the process). The Solarspring® and Memsys® MD systems (utilization of polymeric membranes) are operated with energy consumptions between 130 kWh/m³ and 350 kWh/m³ (> 97 % accounts for the thermal energy consumption in respect to the total energy consumption) [17]. These values do not come close to the thermal efficiencies that are achieved with reliable

conventional thermal desalination processes (MED: 42 kWh/m³ to 65 kWh/m³, MSF: 62 kWh/m³ to 85 kWh/m³) that are suited to treat higher concentrated saline solutions. Would the commercial MD membrane provider Solarspring or Memsys use ceramic membranes instead of polymeric membranes the energy consumption could be considerably higher (due to the higher thermal conductivity of ceramic membranes) and make the process even less competitive with established thermal desalination methods such as MSF and MED. This makes the reduction of the production costs of ceramic membranes neglectable. The most important goal should be the lowering of the thermal conductivity by using low conductivity materials and by increasing the porosity without sacrificing the mechanical integrity of the membranes. In addition, the development and implementation of innovative heat recovery strategies for ceramic membranes with high packing densities in respect to specific membrane geometries and MD configurations is imperative. Heat recovery strategies for ceramic membranes have not been reported by the literature yet while any commercial MD system using polymeric membranes facilitates heat recovery one way or another. Module integrated energy recovery concepts are an integral part to reduce the energy efficiency of MD processes using ceramic membranes. VMD is believed to be the MD configuration that allow heat recovery concepts most effectively while reducing the heat loss through conduction. Any concept must allow the use of the condensation energy released through the prior condensation stage in order to heat and evaporate the feed solution at a lower temperature level in a next stage. The number of stages must be considered in respect to the efficiency of the heat recovery process and eventually define the GOR of the MD process. On a module scale this requires the integration of permeate condensation and heat recovery devises. For ceramic membranes different concepts using tubular and flat sheet membrane geometries are currently being investigated. In addition, the facilitation of low-cost energy sources should be explored for every MD application especially if ceramic membranes with relatively high thermal conductivities are utilized and heat recovery is not efficiently applied.

Ideally ceramic membranes can be optimized in respect to their stability and their cost-efficiency. But since this poses a considerable technical challenge, the focus on one of those targets in respect to the specific MD applications is a good starting point.

5 Summary and Conclusion

As the global relevance of desalination processes increases and conventional desalination methods have technically matured without overcoming substantial limitations, unconventional desalination processes such as MD processes receive growing attention. It is a technology that hybridizes the benefits of thermal technologies with the flexibility (e.g. scaling and geometric control) offered by membrane processes. Hydrophobic polymeric membranes are predominantly used in MD processes but may not be robust enough if applied in aggressive solutions. Ceramic membranes have yet to find a foothold in the MD community due to several unfavorable characteristics (i.e. hydrophilicity, high cost, and high thermal conductivity). However, ceramic membranes could enable the treatment of solutions exhibiting extreme conditions and extent the areas of application for MD processes considerably.

This work was conducted to obtain a better understanding of the strengths and limitations of ceramic membranes in MD processes. This knowledge was then used to recommend an approach for membrane optimization to boost the use and the commercialization of ceramic membranes for a wide range of MD application. To guide the investigations several research questions with focus on the modification of ceramic membranes and the resulting hydrophobic characteristics, the characterization of membrane properties and the related membrane performance in MD processes (e.g. mass transfer, energy efficiency and stability) as well as mass transfer modelling were defined in the introduction section (chapter 1.2). The following section summarizes the findings throughout this work and demonstrates the successful approach of these research questions as well as the overall project objective.

5.1 Membrane Properties and Membrane Performance

Any Membrane Distillation (MD) process is highly dependent on the hydrophobic membrane that serves as the semi-selective barrier between a warm feed and a cooler permeate side. The membrane enables the selective separation and transportation of volatile components (e. g. water vapor) to the permeate side but also imposes a significant resistance to the mass transport of that component in dependence on its specific properties. Therefore, it is imperative to have knowledge of those membrane properties to understand their impact on the mass and heat transport as well as to validate the generally accepted mass transfer model for asymmetric ceramic membranes. Some membrane properties (e. g. pore size and porosity) were quantified using standard characterization methods as described in chapter 3.2.1 while others (for instance, the thermal

conductivity) required investigative methods that are not used by default. Therefore, a variety of ceramic membranes (e.g. different layer structure, pore size, support thickness, surface modification and thermal conductivity) were thoroughly investigated in respect to their unique properties using thermal conductivity scanning, N_2 permeance, contact angle (CA) and liquid entry pressure (LEP) tests to fully characterize asymmetrically and symmetrically structured single channel ceramic membranes.

The thermal conductivity scanning done on non-modified and modified tubular ceramic membranes made of four material types (Al_2O_3, TiO_2, cordierite and mixed oxides) exposed the following:

- The thermal conductivity of single channel membranes made of cordierite and mixed oxides was as low as 0.5 W/(m K) which is more than a magnitude higher than the thermal conductivity of polymeric MD membranes.
- The thermal conductivity of Al_2O_3 and TiO_2 single channel membranes differed by a factor of around 3 despite considerably stronger deviations regarding the thermal conductivity of the material.
- The thermal conductivity was highly dominated by the support characteristics (material and porosity) and not significantly affected by the membrane coating or modification process.
- The thermal conductivity must be determined experimentally due to the individual microstructure of ceramic membranes (e.g., grain sintering, grain growth and pore formation) that is highly dependent on the sintering regime and is not accounted for by accepted thermal conductivity models.

N_2 permeance tests were conducted on different symmetrically and consecutively coated asymmetrically structured ceramic membranes which led to the following findings:

- The support properties dominated the mass transfer through asymmetrically structured ceramic membranes.
- Larger support pore sizes led to higher mass transfer rates but also resulted in a stronger reduction of the mass transfer rate after subsequent layer coating steps.
- The mass transfer through symmetrically structured ceramic membranes was not competitive with the mass transfer facilitated by asymmetrically structured ceramic membranes even if 30 % thinner support walls were used.
- The surface modification did not impact the mass transfer in N_2 permeance tests.

Static, advancing and receding CA measurements were conducted on Al_2O_3 flat-sheet membranes modified with nine different hydrophobic agents. This was done to identify a non-fluorinated hydrophobic agent that could pose as a potential alternative to the fluorinated agents that were successfully used to modify ceramic single channel membranes prior to this work. Based on a static CA of 140° and an advancing and receding CA above 90° (resulting in a small CA hysteresis of 32°) the molecule n-Octyltriethoxysilane (labelled 'HOM') was chosen.

Liquid entry pressure tests conducted on a variety of different ceramic single channel membranes using different modification agents, concentrations and feeds revealed the following:

- The LEP was higher than 2.5 bar for all membranes with pore sizes smaller or equal of 400 nm indicating the general suitability of modified ceramic membranes for MD processes.
- The LEP of TiO_2 membranes was competitive with the LEP of polymeric membranes with the same pore size and tested at similar conditions.
- The non-fluorinated hydrophobic agent was as effective in rendering the surface of ceramic membranes hydrophobic as the fluorinated molecules.
- The use of 1 wt.% of the tested hydrophobic agents was sufficient for the modification of asymmetrically structured ceramic membranes.
- If high feed temperatures are applied modified ceramic membranes with pore sizes smaller than 400 nm should be used.
- The LEP increased linearly with increasing salinities from 50 g NaCl per kg H_2O
- The use of a 20 wt.% ethanol test solution led to reduction of the LEP of more than 50 % in comparison to the LEP determined using pure water as the test solution.

Subsequently to their thorough characterization DCMD and VMD test were conducted (under fixed standard operational parameters) on a variety of different ceramic single channel membranes. Using this approach, the MD results could be put in perspective and evaluated in respect to how specific membrane properties impact the MD performance. The most substantial observations were:

- In DCMD, the heat and mass transfer were affected by partial wetting of the large support pores.
- The intermediate and final membrane layer affected the mass transfer in DCMD significantly.
- The mass transfer achieved in DCMD was considerably lower than the mass transfer determined in VMD.

- The selectivity of the ceramic membranes was excellent in DCMD and VMD.
- Fluxes above 20 kg/(m² h) could be achieved in VMD at moderate driving forces (asymmetric TiO_2 membrane, T_{Feed}: 60 °C, p_{abs}: 100 mbar).
- The mass transfer in VMD was in accordance with the mass transfer determined via N_2 permeance tests and dominated by the support properties.
- The reduction of the wall thickness was only beneficial in VMD.
- The mass transfer of symmetric ceramic single channel membranes was not competitive with the mass transfer of their asymmetric counterparts.

Stability tests were conducted on symmetrically and asymmetrically structured ceramic membranes based on the assumption that asymmetrically structured ceramic membranes are more sensitive towards harsh environments due to the dependency of their selectivity on the integrity of a very thin final membrane layer. For this, the initial LEP of selected membranes was compared to the LEP determined after the membranes were contacted with abrasive (highly saline) solutions or were cooked in saline solutions characterized by extreme pH values. The following findings were made:

- The cooking of membranes modified with fluorinated or non-fluorinated hydrophobic agents in a neutral or neutral and saline solution did not (or slightly positively) affect the LEP.
- The treatment with the saline alkaline solution led to a moderate decline of the LEP for asymmetric membrane types independent of the hydrophobic agents while the LEP of symmetric membranes was not strongly affected.
- The treatment with the saline acidic solution led to a strong decline of the LEP for all membrane types and hydrophobic agents except for the symmetrically structured ceramic membranes modified with a fluorinated agent.
- The LEP of symmetrically and asymmetrically structured ceramic membranes was not affected by being contacted (run through at 0.73 m/s) with an abrasive solution for up to 56 hours.

In conclusion, modified ceramic membranes were successfully utilized in MD processes exhibiting excellent rejections and decent permeate fluxes. Ceramic membranes are more suited for the utilization in VMD than in DCMD processes due to their relatively high thermal conductivities. Asymmetrically structured ceramic membranes outperform symmetrically structured membranes in respect to the mass transport and their use in environments that are not highly aggressive (for instance, extreme pH values) should be favored. The optimization of the support properties (pore

size, porosity and thickness) is most important to maximize the mass transfer of asymmetrically structured ceramic membranes. Fluorinated and non-fluorinated hydrophobic agents can be applied to modify hydrophilic ceramic membranes and qualify them for MD processes. Symmetrically structured ceramic membranes modified with a fluorinated hydrophobic agent are considerably more resistant towards extreme pH values than their asymmetrically structured counterparts or membranes modified with non-fluorinated agents and their utilization should be favored in chemically aggressive environments. Harsh environments or feeds containing surface tension lowering substances require the use of membranes with pore sizes smaller than 400 nm to minimize the risk of wetting.

5.2 Operational Parameters, Real Solutions and Mass Transfer Modelling

The permeate yield and quality as well as the energy efficiency of the MD processes are not only dependent on the membrane but on the operational parameters such as the feed temperature and composition, flow velocity and permeate pressure. For instance, these parameters affect polarization effects, define the risk of wetting as well as the driving force. To understand the impact of specific process parameters asymmetric ceramic single channel membranes (Al_2O_3 and TiO_2) were tested in VMD under the variation of the feed temperature, salinity, flow velocity as well as the permeate pressure and cold trap temperature. In addition, a real RO concentrate from the dairy industry as well as an artificial leachate from the potassium mining industry was treated using asymmetric Al_2O_3 and TiO_2 membranes. The following observation were made:

- Even at very high feed concentrations (350 g NaCl per kg H_2O) excellent rejections above 99.9 % and permeate fluxes of more than 35 kg/(m² h) were achieved using TiO_2 membranes at relatively high driving forces (T_{Feed}: 75 °C, P_{abs}: 75 mbar).
- For all temperatures and permeate pressures TiO_2 membranes (final pore size: 100 nm) showed permeate fluxes of around 50 % higher than the permeate fluxes achieved with a Al_2O_3 membrane (final pore size: 100 nm).
- Despite the exponential relationship between the feed temperature and the driving force (water vapor partial pressure) the incline of flux with increasing temperatures was higher at lower feed temperatures than at higher feed temperatures.
- The increase of the feed flow velocity led to an increase of the permeate flux for both membrane types and all feed temperatures and concentrations.

- The increase of the permeate flux with increasing flow velocity was equally pronounced for all feed temperatures for TiO_2 membranes but stronger for Al_2O_3 membranes at higher feed temperatures.
- The energy efficiency of both membranes was relatively low (TiO_2 > Al_2O_3) and increased with increasing feed flow velocity.
- The increasing salinity affected the permeate flux of a Al_2O_3 membrane considerably. However, even concentrations (> 300 g NaCl per kg H_2O) a permeate flux of more than 10 kg/(m² h) was achieved.
- The permeate flux (Al_2O_3 membrane) declined to near zero when the NaCl concentration approached the saturation point.
- A highly concentrated leachate was treated successfully using a Al_2O_3 membrane achieving permeate fluxes of up to 17.5 kg/(m² h) and permeate qualities between 7.8 mS/cm and 15 mS/cm.
- A real RO concentrate containing 1 wt.% humic substances could only be treated (achieving up to 17 kg/(m² h) permeate) in VMD after the pretreatment of the feed using a 5 nm membrane (the permeate flux declined to around 10 kg/(m^2 h) over a time period of 24 hours).

A VMD mass transfer model proposed by the literature (based on the DGM) was adopted to facilitate the calculation of the mass transfer of asymmetrically structured TiO_2 membranes in respect to the feed temperature and feed flow velocity. Deficiencies of the model were identified and addressed by integrating correction factors for the feed temperature at the interface of the membrane adjusting the driving force accordingly. The main observations were:

- The VMD model in its natural state predicted permeate fluxes that were in good agreement with the experimentally obtained permeate flux data for low feed temperatures and low feed velocities.
- The deviations between the predicted and the measured values increased with increasing feed temperatures and decreasing feed flow velocities suggesting a gradually more pronounced underestimation of polarization effects (for instance, the VMD model does not account for temperature polarization via conduction).
- The integration of a correction factor that is dependent on the feed temperature and feed flow velocity led to an excellent agreement between the measured and calculated fluxes over all feed temperatures and feed flow velocities as well as for different membrane pore sizes and feed salinities.

In conclusion, modified ceramic membranes were successfully used to treat highly saline synthetic and real solutions achieving excellent rejections and good permeate fluxes in VMD if crystallization is avoided. In respect to the mass transfer and energy efficiency TiO_2 membranes outperform similar membranes made of Al_2O_3 due to the lower thermal conductivity moderating temperature polarization effects more effectively. The use of high feed temperatures in VMD is more attractive for ceramic membranes made of materials with relatively low thermal conductivities and is more beneficial if relatively high feed flow rates are applied. Feeds containing surface-active substances must be pretreated sufficiently to avoid wetting during MD processes and to guarantee process stability. The mass transfer through asymmetric ceramic membrane was successfully modelled using a model suggested by the literature based on the DGM. The use of the model for ceramic membranes is adequate for relatively low feed temperatures and high feed flow velocities even though the shape of the pores (slot-shaped) nor the pore size distribution is accounted for by the model.

The mass transfer rates of ceramic single channel membranes presented in this work are of the same magnitude of the permeate fluxes for ceramic membranes that are reported in the literature [36,51] indicating the consistency of performance data obtained and presented within this study. Ceramic membranes are competitive with polymeric membranes regarding their mass transfer but currently lack the cost-efficiency (lower energy efficiency) to make them truly attractive for a broader utilization in MD processes. The cost-efficiency could be improved by increasing the energy efficiency. This can be achieved by using low-conductivity materials or by increasing the membrane porosity to reduce the heat loss via conduction. Additionally, membrane geometries with high packing densities and respective modules need to be developed that allow the recovery of latent heat. In addition, it is imperative to exploit low grade energy sources such as waste heat or regenerative energy sources to drive the process using ceramic membranes. If the cost-efficiency of ceramic membranes in MD processes is improved, they can be a viable option for the treatment of aggressive solutions that are too extreme for polymeric membranes such as solutions that are close to the saturation point, have extreme pH values or are characterized by high temperatures. In this regard, it is also imperative to investigate if potential damages to ceramic membranes can be reversed using specific cleaning and restoration procedures. To facilitate the long-term application of ceramic membranes in harsh environments the layer design and surface modification must be tailored to the specific MD environment. Ideally both approaches can be pursued simultaneously and enable ceramic membranes for a great variety of MD applications.

References

[1] T. Russo, K. Alfredo, J. Fisher, Sustainable Water Management in Urban, Agricultural, and Natural Systems, Water 6 (2014) 3934–3956.

[2] United Nations - General Assembly, The human right to water and sanitation: A/RES/64/292, 2010.

[3] M.M. Mekonnen, A.Y. Hoekstra, Four billion people facing severe water scarcity, Science advances 2 (2016) e1500323.

[4] World population prospects, United Nations, New York, NY, 2019.

[5] U.N.E.S.A.C. Organization, united nations world water development report 2020: Water and climate change, united nations educationa, [S.l.], 2020.

[6] E. Jones, M. Qadir, M.T.H. van Vliet, V. Smakhtin, S.-M. Kang, The state of desalination and brine production: A global outlook, The Science of the total environment 657 (2019) 1343–1356.

[7] N.A. Ahmad, P.S. Goh, L.T. Yogarathinam, A.K. Zulhairun, A.F. Ismail, Current advances in membrane technologies for produced water desalination, Desalination 493 (2020) 114643.

[8] Nature-based solutions for water, United Nations Educational, Scientific and Cultural Organization, Paris, 2018.

[9] P. Pal, Membrane based technologies for environmental pollution control, Butterworth-Heinemann, Amsterdam, 2020.

[10] A. Bazargan, A Multidisciplinary Introduction to Desalination, River Publishers, Aalborg, 2017.

[11] J. Eke, A. Yusuf, A. Giwa, A. Sodiq, The global status of desalination: An assessment of current desalination technologies, plants and capacity, Desalination 495 (2020) 114633.

[12] The Role of Desalination in an Increasingly Water-Scarce World, World Bank, 2019.

[13] K. Elsaid, M. Kamil, E.T. Sayed, M.A. Abdelkareem, T. Wilberforce, A. Olabi, Environmental impact of desalination technologies: A review, The Science of the total environment 748 (2020) 141528.

[14] Y. Ghalavand, M.S. Hatamipour, A. Rahimi, A review on energy consumption of desalination processes, Desalination and Water Treatment 171 (2014) 1–16.

[15] S. Bhojwani, K. Topolski, R. Mukherjee, D. Sengupta, M.M. El-Halwagi, Technology review and data analysis for cost assessment of water treatment systems, The Science of the total environment 651 (2019) 2749–2761.

[16] M. Qasim, M. Badrelzaman, N.N. Darwish, N.A. Darwish, N. Hilal, Reverse osmosis desalination: A state-of-the-art review, Desalination 459 (2019) 59–104.

[17] L. Eykens, a comprehensive Study of membrane distillation development, configuration assessment and applications, Leuven, 2017.

[18] A. Yusuf, A. Sodiq, A. Giwa, J. Eke, O. Pikuda, G. de Luca, J.L. Di Salvo, S. Chakraborty, A review of emerging trends in membrane science and technology for sustainable water treatment, Journal of Cleaner Production 266 (2020) 121867.

[19] L.F. Greenlee, D.F. Lawler, B.D. Freeman, B. Marrot, P. Moulin, Reverse osmosis desalination: water sources, technology, and today's challenges, Water research 43 (2009) 2317–2348.

[20] A. Panagopoulos, K.-J. Haralambous, M. Loizidou, Desalination brine disposal methods and treatment technologies - A review, The Science of the total environment 693 (2019) 133545.

[21] S. Roy, S. Ragunath, Emerging Membrane Technologies for Water and Energy Sustainability: Future Prospects, Constrains and Challenges, Energies 11 (2018) 2997.

[22] H. Nassrullah, S.F. Anis, R. Hashaikeh, N. Hilal, Energy for desalination: A state-of-the-art review, Desalination 491 (2020) 114569.

[23] A. Giwa, V. Dufour, F. Al Marzooqi, M. Al Kaabi, S.W. Hasan, Brine management methods: Recent innovations and current status, Desalination 407 (2017) 1–23.

[24] N. Kress, Marine Environmental Impact of Seawater Desalination: Science, Management, and Policy, Elsevier, San Diego, 2019.

[25] K. Elsaid, E.T. Sayed, M.A. Abdelkareem, M.S. Mahmoud, M. Ramadan, A.G. Olabi, Environmental impact of emerging desalination technologies: A preliminary evaluation, Journal of Environmental Chemical Engineering 8 (2020) 104099.

[26] S. Yao, M. Ji, A Small RO and MCDI Coupled Seawater Desalination Plant and Its Performance Simulation Analysis and Optimization, Processes 8 (2020) 944.

[27] M. Reza Shirzad Kebria, A. Rahimpour, Membrane Distillation: Basics, Advances, and Applications, in: A. Abdelrasoul (Ed.), Advances in Membrane Technologies, IntechOpen, 2020.

[28] E. Drioli, A. Ali, F. Macedonio, Membrane distillation: Recent developments and perspectives, Desalination 356 (2015) 56–84.

[29] J.A. Sanmartino, M. Khayet, M.C. García-Payo, Desalination by Membrane Distillation, in: Emerging Membrane Technology for Sustainable Water Treatment, Elsevier, 2016, pp. 77–109.

[30] F. Benyahia, Membrane-distillation in desalination, CRC Press/Taylor & Francis Group, Boca Raton, FL, 2020.

[31] N. Thomas, M.O. Mavukkandy, S. Loutatidou, H.A. Arafat, Membrane distillation research & implementation: Lessons from the past five decades, Separation and Purification Technology 189 (2017) 108–127.

[32] M. Gryta, Calcium sulphate scaling in membrane distillation process, Chemical Papers 63 (2009) 177.

[33] M. Gryta, Degradation of Polypropylene Membranes Applied in Membrane Distillation Crystallizer, Crystals 6 (2016) 33.

[34] Z. Hendren, Novel Ceramic Membranes for Membrane distillation: Surface modification, performance comparison with PTFE membranes, and treatment of municipal wastewater, Durham, 2011.

[35] J.-W. Wang, L. Li, J.-W. Zhang, X. Xu, C.-S. Chen, β-Sialon ceramic hollow fiber membranes with high strength and low thermal conductivity for membrane distillation, Journal of the European Ceramic Society 36 (2016) 59–65.

[36] H. Ramlow, R.K.M. Ferreira, C. Marangoni, R.A.F. Machado, Ceramic membranes applied to membrane distillation: A comprehensive review, Int J Appl Ceram Technol 16 (2019) 2161–2172.

[37] N.A. Ahmad, C.P. Leo, A.L. Ahmad, Superhydrophobic alumina membrane by steam impingement: Minimum resistance in microfiltration, Separation and Purification Technology 107 (2013) 187–194.

[38] F. Brodard, J. Romero, M.P. Belleville, J. Sanchez, C. Combe-James, M. Dornier, G.M. Rios, New hydrophobic membranes for osmotic evaporation process, Separation and Purification Technology 32 (2003) 3–7.

[39] M. Khayet, T. Matsuura, Membrane Distillation: Principles and Applications, 1st ed., Elsevier professional, s.l., 2011.

[40] E. Drioli, Y. Wu, V. Calabro, Membrane distillataion in the treatment of aqueous solutions, Journal of Membrane Science 33 (1987) 277–284.

[41] Pervaporation, vapour permeation and membrane distillation: Principles and applications, Woodhead Publishing an imprint of Elsevier, Kidlington, UK, 2015.

[42] M. Khayet, Membranes and theoretical modeling of membrane distillation: a review, Advances in colloid and interface science 164 (2011) 56–88.

[43] I.C. Karagiannis, P.G. Soldatos, Water desalination cost literature: review and assessment, Desalination 223 (2008) 448–456.

[44] E. Curcio, E. Drioli, Membrane Distillation and Related Operations—A Review, Separation & Purification Reviews 34 (2005) 35–86.

[45] J. Swaminathan, H.W. Chung, D.M. Warsinger, J.H. Lienhard V, Energy efficiency of membrane distillation up to high salinity: Evaluating critical system size and optimal membrane thickness, Applied Energy 211 (2018) 715–734.

[46] M. Gryta, Fouling in direct contact membrane distillation process, Journal of Membrane Science 325 (2008) 383–394.

[47] A. Al-Karaghouli, L.L. Kazmerski, Energy consumption and water production cost of conventional and renewable-energy-powered desalination processes, Renewable and Sustainable Energy Reviews 24 (2013) 343–356.

[48] M. Khayet, Solar desalination by membrane distillation: Dispersion in energy consumption analysis and water production costs (a review), Desalination 308 (2013) 89–101.

[49] E. Drioli, G. Di Profio, E. Curcio, Progress in membrane crystallization, Current Opinion in Chemical Engineering 1 (2012) 178–182.

[50] M.S. El-Bourawi, Z. Ding, R. Ma, M. Khayet, A framework for better understanding membrane distillation separation process, Journal of Membrane Science 285 (2006) 4–29.

[51] Z.S. Tai, M.H. Abd Aziz, M.H.D. Othman, M.I.H. Mohamed Dzahir, N.A. Hashim, K.N. Koo, S.K. Hubadillah, A.F. Ismail, M. A Rahman, J. Jaafar, Ceramic Membrane Distillation for Desalination, Separation & Purification Reviews 49 (2020) 317–356.

[52] G. Gude, Emerging Technologies for Sustainable Desalination Handbook, Elsevier Science & Technology, San Diego, 2018.

[53] H.C. Duong, Membrane distillation for strategic desalination applications, 2017.

[54] P. Wang, T.-S. Chung, Recent advances in membrane distillation processes: Membrane development, configuration design and application exploring, Journal of Membrane Science 474 (2015) 39–56.

[55] J. Schnittger, J. McCutcheon, T. Hoyer, M. Weyd, G. Fischer, P. Puhlfürß, M. Halisch, I. Voigt, A. Lerch, Hydrophobic ceramic membranes in MD processes – Impact of material selection and layer characteristics, Journal of Membrane Science 618 (2021) 118678.

[56] D. Winter, Membrane distillation: A thermodynamic, technological and economic analysis. Zugl.: Kaiserslautern, Techn. Univ., Diss., 2015, Shaker, Aachen, 2015.

[57] G.C. Sarti, C. Gostoli, S. Bandini, Extraction of organic components from aqueous streams by vacuum membrane distillation, Journal of Membrane Science 80 (1993) 21–33.

[58] S. Bandini, G.C. Sarti, Heat and mass transport resistances in vacuum membrane distillation per drop, AIChE J. 45 (1999) 1422–1433.

[59] M. Rezaei, D.M. Warsinger, J.H. Lienhard V, M.C. Duke, T. Matsuura, W.M. Samhaber, Wetting phenomena in membrane distillation: Mechanisms, reversal, and prevention, Water research 139 (2018) 329–352.

[60] T. Mohammadi, M. Akbarabadi, Separation of ethylene glycol solution by vacuum membrane distillation (VMD), Desalination 181 (2005) 35–41.

[61] A. Alkhudhiri, N. Darwish, N. Hilal, Membrane distillation: A comprehensive review, Desalination 287 (2012) 2–18.

[62] M. Khayet, P. Godino, J.I. Mengual, Theory and experiments on sweeping gas membrane distillation, Journal of Membrane Science 165 (2000) 261–272.

[63] M. García-Payo, C. Rivier, I. Marison, U. von Stockar, Separation of binary mixtures by thermostatic sweeping gas membrane distillation, Journal of Membrane Science 198 (2002) 197–210.

[64] P. Biniaz, N. Torabi Ardekani, M. Makarem, M. Rahimpour, Water and Wastewater Treatment Systems by Novel Integrated Membrane Distillation (MD), ChemEngineering 3 (2019) 8.

[65] C. Rivier, Separation of binary mixtures by thermostatic sweeping gas membrane distillation I. Theory and simulations, Journal of Membrane Science 201 (2002) 1–16.

[66] A.E. Jansen, J.W. Assink, J.H. Hanemaaijer, J. van Medevoort, E. van Sonsbeek, Development and pilot testing of full-scale membrane distillation modules for deployment of waste heat, Desalination 323 (2013) 55–65.

[67] J.A. Andrés-Mañas, A. Ruiz-Aguirre, F.G. Acién, G. Zaragoza, Assessment of a pilot system for seawater desalination based on vacuum multi-effect membrane distillation with enhanced heat recovery, Desalination 443 (2018) 110–121.

[68] L. Francis, N. Ghaffour, A.A. Alsaadi, G.L. Amy, Material gap membrane distillation: A new design for water vapor flux enhancement, Journal of Membrane Science 448 (2013) 240–247.

[69] L. Cheng, Y. Zhao, P. Li, W. Li, F. Wang, Comparative study of air gap and permeate gap membrane distillation using internal heat recovery hollow fiber membrane module, Desalination 426 (2018) 42–49.

[70] A. Kullab, R. Fakhrai, A. Martin, Experimental evaluation of a modified air-gap membrane distillation prototype, Desalination and Water Treatment 51 (2013) 4998–5004.

[71] L.-H. Cheng, Y.-H. Lin, J. Chen, Enhanced air gap membrane desalination by novel finned tubular membrane modules, Journal of Membrane Science 378 (2011) 398–406.

[72] J. Cai, H. Yin, F. Guo, Transport analysis of material gap membrane distillation desalination processes, Desalination 481 (2020) 114361.

[73] A. Franken, J. Nolten, M. Mulder, D. Bargeman, C.A. Smolders, Wetting criteria for the applicability of membrane distillation, Journal of Membrane Science 33 (1987) 315–328.

[74] S.K. Hubadillah, Z.S. Tai, M.H.D. Othman, Z. Harun, M.R. Jamalludin, M.A. Rahman, J. Jaafar, A.F. Ismail, Hydrophobic ceramic membrane for membrane distillation: A mini review on preparation, characterization, and applications, Separation and Purification Technology 217 (2019) 71–84.

[75] ASTM International, Standard Practice for Surface Wettability of Coatings, Substrates and Pigments by Advancing Contact Angle Measurement, 2013.

[76] V. Gitis, G. Rothenberg, Ceramic membranes: New opportunities and practical applications, Wiley-VCH Verlag GmbH & Co. KGaA, Weinheim, 2016.

[77] R.E. Johnson, R.H. Dettre, Contact Angle Hysteresis. III. Study of an Idealized Heterogeneous Surface, J. Phys. Chem. 68 (1964) 1744–1750.

[78] A. Neumann, R. Good, Thermodynamics of contact angles. I. Heterogeneous solid surfaces, Journal of Colloid and Interface Science 38 (1972) 341–358.

[79] M.R. Rahimpour, M.A. Esmaeilbeig, Membrane Wetting in Membrane Distillation, in: Current Trends and Future Developments on (Bio-) Membranes, Elsevier, 2019, pp. 143–174.

[80] J. Tröger, K. Lunkwitz, W. Bürger, Determination of the Surface Tension of Microporous Membranes Using Contact Angle Measurements, Journal of Colloid and Interface Science 194 (1997) 281–286.

[81] G. Whyman, E. Bormashenko, T. Stein, The rigorous derivation of Young, Cassie–Baxter and Wenzel equations and the analysis of the contact angle hysteresis phenomenon, Chemical Physics Letters 450 (2008) 355–359.

[82] N.A. Ahmad, C.P. Leo, A.L. Ahmad, W.K.W. Ramli, Membranes with Great Hydrophobicity: A Review on Preparation and Characterization, Separation & Purification Reviews 44 (2015) 109–134.

[83] G. Rácz, S. Kerker, Z. Kovács, G. Vatai, M. Ebrahimi, P. Czermak, Theoretical and Experimental Approaches of Liquid Entry Pressure Determination in Membrane Distillation Processes, Period. Polytech. Chem. Eng. 58 (2014) 81–91.

[84] A.T. Servi, J. Kharraz, D. Klee, K. Notarangelo, B. Eyob, E. Guillen-Burrieza, A. Liu, H.A. Arafat, K.K. Gleason, A systematic study of the impact of hydrophobicity on the wetting of MD membranes, Journal of Membrane Science 520 (2016) 850–859.

[85] B.-S. Kim, P. Harriott, Critical entry pressure for liquids in hydrophobic membranes, Journal of Colloid and Interface Science 115 (1987) 1–8.

[86] K. Schneider, W. Hölz, R. Wollbeck, S. Ripperger, Membranes and modules for transmembrane distillation, Journal of Membrane Science 39 (1988) 25–42.

[87] García-Payo, Izquierdo-Gil, Fernández-Pineda, Wetting Study of Hydrophobic Membranes via Liquid Entry Pressure Measurements with Aqueous Alcohol Solutions, Journal of Colloid and Interface Science 230 (2000) 420–431.

[88] F. Varela-Corredor, S. Bandini, Testing the applicability limits of a membrane distillation process with ceramic hydrophobized membranes: The critical wetting temperature, Separation and Purification Technology 250 (2020) 117205.

[89] K.W. Lawson, D.R. Lloyd, Membrane distillation, Journal of Membrane Science 124 (1997) 1–25.

[90] R.A. Johnson, M.H. Nguyen, Understanding membrane distillation and osmotic distillation, John Wiley & Sons Inc, Hoboken, NJ, 2017.

[91] D. Winter, J. Koschikowski, D. Düver, P. Hertel, U. Beuscher, Evaluation of MD process performance: Effect of backing structures and membrane properties under different operating conditions, Desalination 323 (2013) 120–133.

[92] J. Woods, J. Pellegrino, J. Burch, Generalized guidance for considering pore-size distribution in membrane distillation, Journal of Membrane Science 368 (2011) 124–133.

[93] L. Li, K.K. Sirkar, Influence of microporous membrane properties on the desalination performance in direct contact membrane distillation, Journal of Membrane Science 513 (2016) 280–293.

[94] L. Eykens, K. de Sitter, C. Dotremont, L. Pinoy, B. van der Bruggen, How To Optimize the Membrane Properties for Membrane Distillation: A Review, Ind. Eng. Chem. Res. 55 (2016) 9333–9343.

[95] J. Phattaranawik, R. Jiraratananon, A. Fane, Heat transport and membrane distillation coefficients in direct contact membrane distillation, Journal of Membrane Science 212 (2003) 177–193.

[96] I. Hitsov, L. Eykens, K. de Sitter, C. Dotremont, L. Pinoy, B. van der Bruggen, I. Nopens, Calibration and analysis of a direct contact membrane distillation model using Monte Carlo filtering, Journal of Membrane Science 515 (2016) 63–78.

[97] A.R. Kurdian, M. Bahreini, G.H. Montazeri, S. Sadeghi, Modeling of direct contact membrane distillation process: Flux prediction of sodium sulfate and sodium chloride solutions, Desalination 323 (2013) 75–82.

[98] M. Khayet, T. Matsuura, J.I. Mengual, M. Qtaishat, Design of novel direct contact membrane distillation membranes, Desalination 192 (2006) 105–111.

[99] Current Trends and Future Developments on (Bio-) Membranes, Elsevier, 2019.

[100] M. Khayet, K. KHULBE, T. Matsuura, Characterization of membranes for membrane distillation by atomic force microscopy and estimation of their water vapor transfer coefficients in vacuum membrane distillation process, Journal of Membrane Science 238 (2004) 199–211.

[101] J. Phattaranawik, Effect of pore size distribution and air flux on mass transport in direct contact membrane distillation, Journal of Membrane Science 215 (2003) 75–85.

[102] R.W. Schofield, A.G. Fane, C. Fell, Gas and vapour transport through microporous membranes. II. Membrane distillation, Journal of Membrane Science 53 (1990) 173–185.

[103] F. Laganà, G. Barbieri, E. Drioli, Direct contact membrane distillation: modelling and concentration experiments, Journal of Membrane Science 166 (2000) 1–11.

[104] J. Zhang, S. Gray, J.-D. Li, Modelling heat and mass transfers in DCMD using compressible membranes, Journal of Membrane Science 387-388 (2012) 7–16.

[105] J. Zhang, J.-D. Li, S. Gray, Effect of applied pressure on performance of PTFE membrane in DCMD, Journal of Membrane Science 369 (2011) 514–525.

[106] S. Adnan, M. Hoang, H. Wang, Z. Xie, Commercial PTFE membranes for membrane distillation application: Effect of microstructure and support material, Desalination 284 (2012) 297–308.

[107] L. Camacho, L. Dumée, J. Zhang, J.-D. Li, M. Duke, J. Gomez, S. Gray, Advances in Membrane Distillation for Water Desalination and Purification Applications, Water 5 (2013) 94–196.

[108] S.M.F. Hasani, A.S. Sowayan, M. Shakaib, The Effect of Spacer Orientations on Temperature Polarization in a Direct Contact Membrane Distillation Process Using 3-d CFD Modeling, Arab J Sci Eng 44 (2019) 10269–10284.

[109] J. Kujawa, S. Cerneaux, W. Kujawski, M. Bryjak, J. Kujawski, How To Functionalize Ceramics by Perfluoroalkylsilanes for Membrane Separation Process? Properties and Application of Hydrophobized Ceramic Membranes, ACS applied materials & interfaces 8 (2016) 7564–7577.

[110] K. Li, Ceramic Membranes for Separation and Reaction, John Wiley & Sons, Ltd, Chichester, UK, 2007.

[111] R. Sondhi, R. Bhave, G. Jung, Applications and benefits of ceramic membranes, Membrane Technology 2003 (2003) 5–8.

[112] L. Li, M. Chen, Y. Dong, X. Dong, S. Cerneaux, S. Hampshire, J. Cao, L. Zhu, Z. Zhu, J. Liu, A low-cost alumina-mullite composite hollow fiber ceramic membrane fabricated via phase-inversion and sintering method, Journal of the European Ceramic Society 36 (2016) 2057–2066.

[113] I. Voigt, S. Tudyka, Keramische Membranen und Hohlfasern, in: K. Ohlrogge, K. Ebert (Eds.), Membranen, Wiley-VCH Verlag GmbH & Co. KGaA, Weinheim, FRG, 2006, pp. 103–146.

[114] A. Basile, A. Cassano, N.K. Rastogi, Advances in membrane technologies for water treatment: Materials, processes and applications, Elsevier, Boston, MA, 2015.

[115] H.K. Oh, S. Takizawa, S. Ohgaki, H. Katayama, K. Oguma, M.J. Yu, Removal of organics and viruses using hybrid ceramic MF system without draining PAC, Desalination 202 (2007) 191–198.

[116] K. Guerra, J. Pellegrino, Development of a Techno-Economic Model to Compare Ceramic and Polymeric Membranes, Separation Science and Technology 48 (2013) 51–65.

[117] V. Boffa, C. Lunghi, C.A. Quist-Jensen, G. Magnacca, P. Calza, Fabrication and Surface Interactions of Super-Hydrophobic Silicon Carbide for Membrane Distillation, Nanomaterials (Basel, Switzerland) 9 (2019).

[118] H.P. Hsieh, Inorganic Membranes for Separation and Reaction, Elsevier, Burlington, 1996.

[119] Brevier technische Keramik, 4th ed., Fahner, Lauf, 2003.

[120] J. Kujawa, W. Kujawski, S. Koter, A. Rozicka, S. Cerneaux, M. Persin, A. Larbot, Efficiency of grafting of Al2O3, TiO2 and ZrO2 powders by perfluoroalkylsilanes, Colloids and Surfaces A: Physicochemical and Engineering Aspects 420 (2013) 64–73.

[121] S. KRAJEWSKI, W. KUJAWSKI, M. BUKOWSKA, C. PICARD, A. LARBOT, Application of fluoroalkylsilanes (FAS) grafted ceramic membranes in membrane distillation process of NaCl solutions, Journal of Membrane Science 281 (2006) 253–259.

[122] T. Materne, F.D. Buyl, G. Witucki (Eds.), Organosilane Technology in Coating Applications Review and Perspectives, 2012.

[123] M.V. Solmi, M. Schmitz, W. Leitner, CO2 as a Building Block for the Catalytic Synthesis of Carboxylic Acids, in: Horizons in Sustainable Industrial Chemistry and Catalysis, Elsevier, 2019, pp. 105–124.

[124] J. Kujawa, S. Cerneaux, W. Kujawski, Highly hydrophobic ceramic membranes applied to the removal of volatile organic compounds in pervaporation, Chemical Engineering Journal 260 (2015) 43–54.

[125] M. Dawood, Durability of steel components strengthened with fiber-reinforced polymer (FRP) composites, in: Rehabilitation of Metallic Civil Infrastructure Using Fiber Reinforced Polymer (FRP) Composites, Elsevier, 2014, pp. 96–114.

[126] S.A. Kulinich, M. Farzaneh, Hydrophobic properties of surfaces coated with fluoroalkylsiloxane and alkylsiloxane monolayers, Surface Science 573 (2004) 379–390.

[127] DOW Corning Corperation, A guide to silane solutions: The basic of silane chemistry, USA, 2009, https://www.google.com/url?sa=t&rct=j&q=&esrc=s&source=web&cd=&ved=2ahUKEwih-JCo0I7tAhVBQhoKHV_eBZ0QFjAAegQICBAC&url=https%3A%2F%2Fwww.researchgate.net%2Fprofile%2FTalaat_El-Emary%2Fpost%2FIs_the_reaction_between_Si-OH_and_NH2-Ar_possible%2Fattachment%2F59d6328679197b8077990409%2FAS%253A370824558202888%2540465422872980%2Fdownload%2FSilane%2BChemistry-1a-95-718-01-F2.pdf&usg=AOvVaw3U3_DKDOdZGJHis9H4wTwC, accessed 19 November 2020.

[128] C. PICARD, A. LARBOT, E. Tronel-Peyroz, R. Berjoan, Characterisation of hydrophilic ceramic membranes modified by fluoroalkylsilanes into hydrophobic membranes, Solid State Sciences 6 (2004) 605–612.

[129] J. Schnittger, M. Weyd, I. Voigt, A. Lerch, Keramische Membranen in der Membrandestillation, Chemie Ingenieur Technik 91 (2019) 1101–1109.

[130] J. Lu, Y. Yu, J. Zhou, L. Song, X. Hu, A. Larbot, FAS grafted superhydrophobic ceramic membrane, Applied Surface Science 255 (2009) 9092–9099.

[131] J. Kujawa, S. Cerneaux, S. Koter, W. Kujawski, Highly efficient hydrophobic titania ceramic membranes for water desalination, ACS applied materials & interfaces 6 (2014) 14223–14230.

[132] S. Koonaphapdeelert, K. Li, Preparation and characterization of hydrophobic ceramic hollow fibre membrane, Journal of Membrane Science 291 (2007) 70–76.

[133] Y. Yu, W. Hou, X. Hu, Y. Yu, Le Mi, L. Song, Superhydrophobic modification of an Al 2 O 3 microfiltration membrane with TiO 2 coating and PFDS grafting, RSC Adv 4 (2014) 48317–48321.

[134] S. Khemakhem, R. Ben, Synthesis and Characterization of a Novel Hydrophobic Membrane: Application for Seawater Desalination with Air Gap Membrane Distillation Process, in: F. Shi (Ed.), Ceramic Materials - Progress in Modern Ceramics, InTech, 2012.

[135] D. Schondelmaier, S. Cramm, R. Klingeler, J. Morenzin, C. Zilkens, W. Eberhardt, Orientation and Self-Assembly of Hydrophobic Fluoroalkylsilanes, Langmuir 18 (2002) 6242–6245.

[136] Y.-F. Lin, W.-W. Wang, C.-Y. Chang, Environmentally sustainable, fluorine-free and waterproof breathable PDMS/PS nanofibrous membranes for carbon dioxide capture, J. Mater. Chem. A 6 (2018) 9489–9497.

[137] J. Kujawa, S. Al-Gharabli, W. Kujawski, K. Knozowska, Molecular Grafting of Fluorinated and Nonfluorinated Alkylsiloxanes on Various Ceramic Membrane Surfaces for the Removal of Volatile Organic Compounds Applying Vacuum Membrane Distillation, ACS applied materials & interfaces 9 (2017) 6571–6590.

[138] J. Kujawa, S. Cerneaux, W. Kujawski, K. Knozowska, Hydrophobic Ceramic Membranes for Water Desalination, Applied Sciences 7 (2017) 402.

[139] J.-W. Wang, X.-Z. Li, M. Fan, J.-Q. Gu, L.-Y. Hao, X. Xu, C.-S. Chen, C.-M. Wang, Y.-Z. Hao, S. Agathopoulos, Porous β-Sialon planar membrane with a robust polymer-derived hydrophobic ceramic surface, Journal of Membrane Science 535 (2017) 63–69.

[140] Y. Dong, L. Ma, C.Y. Tang, F. Yang, X. Quan, D. Jassby, M.J. Zaworotko, M.D. Guiver, Stable Superhydrophobic Ceramic-Based Carbon Nanotube Composite Desalination Membranes, Nano letters 18 (2018) 5514–5521.

[141] S.P. Agashichev, A.V. Sivakov, Modeling and calculation of temperature-concentration polarisation in the membrane distillation process (MD), Desalination 93 (1993) 245–258.

[142] R.W. Schofield, A.G. Fane, C. Fell, Heat and mass transfer in membrane distillation, Journal of Membrane Science 33 (1987) 299–313.

[143] A.G. Fane, R.W. Schofield, C. Fell, The efficient use of energy in membrane distillation, Desalination 64 (1987) 231–243.

[144] D.C. Abbott, Book Reviews Pollution of our Atmosphere by B. Henderson-Sellers. Published by Adam Hilger Ltd., Bristol, 1984. Price: £13.95. Pp 210. ISBN: 0 85274-763-2, Journal of the Royal Society of Health 105 (1985) 37.

[145] M. Khayet, A. Velázquez, J.I. Mengual, Modelling mass transport through a porous partition: Effect of pore size distribution, Journal of Non-Equilibrium Thermodynamics 29 (2004).

[146] I. Hitsov, T. Maere, K. de Sitter, C. Dotremont, I. Nopens, Modelling approaches in membrane distillation: A critical review, Separation and Purification Technology 142 (2015) 48–64.

[147] A.I. Simion, C. Grigoraş, A. Roșu, L. Gavrilă, Mathematical modelling of density and viscosity of nacl aqueous solutions, Journal of Agroalimentary Processes and Technologies 2015 (2015) 41–52.

[148] M. Gryta, M. Tomaszewska, A.W. Morawski, Membrane distillation with laminar flow, Separation and Purification Technology 11 (1997) 93–101.

[149] M. Gryta, M. Tomaszewska, Heat transport in the membrane distillation process, Journal of Membrane Science 144 (1998) 211–222.

[150] A.Z. Borucka, J.O. Bockris, J.A. Kitchener, Test of the Applicability of the Nernst-Einstein Equation to Self-Diffusion and Conduction of Ions in Molten Sodium Chloride, The Journal of chemical physics 24 (1956) 1282.

[151] J. Sedlbauer, R.H. Wood, Thermodynamic Properties of Dilute NaCl(aq) Solutions near the Critical Point of Water, J. Phys. Chem. B 108 (2004) 11838–11849.

[152] C. Fernández-Pineda, M. Izquierdo-Gil, M. García-Payo, Gas permeation and direct contact membrane distillation experiments and their analysis using different models, Journal of Membrane Science 198 (2002) 33–49.

[153] G.V. Barbossa-Cánovas, A.J. Fontana, S.J. Schmidt, T.P. Labuza, Water activity in foods: Fundamentals and applications Gustavo V. Barbossa-Cánovas, Anthony J. Fontana, Shelly J. Schmidt, Theodore P. Labuza, editors, 1st ed., Blackwell Publishing, Ames, Iowa, 2007.

[154] M. Khayet, M.P. Godino, J.I. Mengual, Modelling Transport Mechanism Through A Porous Partition, Journal of Non-Equilibrium Thermodynamics 26 (2001) 1–14.

[155] E.A. Mason, A.P. Malinauskas, Gas transport in porous media, Elsevier, Amsterdam, 1983.

[156] R.G. Rinker, Transport in porous catalysts, by R. Jackson, Chemical Engineering Monographs Vol. 4, Elsevier Scientific Publishing Co., New York, 1977.(197 pages,$29.80), AIChE J. 25 (1979) 205–206.

[157] Synthetic Membranes for Membrane Processes, in: Synthetic Polymeric Membranes, Springer Berlin Heidelberg, Berlin, Heidelberg, 2008, pp. 5–18.

[158] S. ALOBAIDANI, E. CURCIO, F. MACEDONIO, G. DIPROFIO, H. ALHINAI, E. DRIOLI, Potential of membrane distillation in seawater desalination: Thermal efficiency, sensitivity study and cost estimation, Journal of Membrane Science 323 (2008) 85–98.

[159] A.F. Mills, Basic heat and mass transfer, 2nd ed., Prentice Hall, Upper Saddle River, N.J., 1999.

[160] K.W. Lawson, D.R. Lloyd, Membrane distillation. I. Module design and performance evaluation using vacuum membrane distillation, Journal of Membrane Science 120 (1996) 111–121.

[161] Bohl, Elmendorf, Technische Strömungslehre, 15th ed., Vogel Buchverlag, 2014.

[162] S. Gunko, S. Verbych, M. Bryk, N. Hilal, Concentration of apple juice using direct contact membrane distillation, Desalination 190 (2006) 117–124.

[163] S. SRISURICHAN, R. Jiraratananon, A. FANE, Mass transfer mechanisms and transport resistances in direct contact membrane distillation process, Journal of Membrane Science 277 (2006) 186–194.

[164] M. Qtaishat, T. Matsuura, B. Kruczek, M. Khayet, Heat and mass transfer analysis in direct contact membrane distillation, Desalination 219 (2008) 272–292.

[165] T.-C. Chen, C.-D. Ho, H.-M. Yeh, Theoretical modeling and experimental analysis of direct contact membrane distillation, Journal of Membrane Science 330 (2009) 279–287.

[166] J. Phattaranawik, R. Jiraratananon, Direct contact membrane distillation: effect of mass transfer on heat transfer, Journal of Membrane Science 188 (2001) 137–143.

[167] Emerging Membrane Technology for Sustainable Water Treatment, Elsevier, 2016.

[168] L. Eykens, T. Reyns, K. de Sitter, C. Dotremont, L. Pinoy, B. van der Bruggen, How to select a membrane distillation configuration? Process conditions and membrane influence unraveled, Desalination 399 (2016) 105–115.

[169] T.Y. Cath, V. Adams, A.E. Childress, Experimental study of desalination using direct contact membrane distillation: a new approach to flux enhancement, Journal of Membrane Science 228 (2004) 5–16.

[170] R.W. Schofield, A.G. Fane, C. Fell, R. Macoun, Factors affecting flux in membrane distillation, Desalination 77 (1990) 279–294.

[171] L. Martínez-Díez, M.I. Vázquez-González, Effects of Polarization on Mass Transport through Hydrophobic Porous Membranes, Ind. Eng. Chem. Res. 37 (1998) 4128–4135.

[172] L. Martínez-Díez, M. Vázquez-González, Temperature and concentration polarization in membrane distillation of aqueous salt solutions, Journal of Membrane Science 156 (1999) 265–273.

[173] S. Bouguecha, R. Chouikh, M. Dhahbi, Numerical study of the coupled heat and mass transfer in membrane distillation, Desalination 152 (2003) 245–252.

[174] A.M. Alklaibi, N. Lior, Membrane-distillation desalination: Status and potential, Desalination 171 (2005) 111–131.

[175] ISO, Evaluation of pore size distribution and porosity of solid materials by mercury porosimetry and gas adsorption — Part 1: Mercury porosimetry 19.120 Particle size analysis. Sieving, 2016.

[176] DIN, Non-destructive testing - X-ray diffraction from polycristalline and amorphous material - Part 1: General principles, 2003.

[177] ISO, Fine ceramics (advanced ceramics, advanced technical ceramics) — Determination of density and apparent porosity 81.060.30 Advanced ceramics, 2020.

[178] Fraunhofer IKTS, Arbeitsanweisung AAW 274: Bestimmung der Innendruckfestigkeit (Berstdruck), Fraunhofer Institut für Keramische Technologien und Systeme, 2015.

[179] Y.A. Popov, D.F. Pribnow, J.H. Sass, C.F. Williams, H. Burkhardt, Characterization of rock thermal conductivity by high-resolution optical scanning, Geothermics 28 (1999) 253–276.

[180] F. Gao, X. Chen, G. Yu, C. Asumana, Compressible gases transport through porous membrane: A modified dusty gas model, Journal of Membrane Science 379 (2011) 200–206.

[181] J. Kestin, H.E. Khalifa, R.J. Correia, Tables of the dynamic and kinematic viscosity of aqueous NaCl solutions in the temperature range 20–150 °C and the pressure range 0.1–35 MPa, Journal of Physical and Chemical Reference Data 10 (1981) 71–88.

[182] E.C.W. Clarke, D.N. Glew, Erratum: Evaluation of the Thermodynamic Functions for Aqueous Sodium Chloride from Equilibrium and Calorimetric Measurements below 154 °C [J. Phys. Chem. Ref. Data 14 489 (1985)], Journal of Physical and Chemical Reference Data 18 (1989) 545–550.

[183] I.M. Abdulagatov, U.B. Magomedov, Thermal conductivity of aqueous solutions of NaCl and KCl at high pressures, Int J Thermophys 15 (1994) 401–413.

[184] J. Wen, K. Shi, Q. Sun, Z. Sun, H. Gu, Measurement for Surface Tension of Aqueous Inorganic Salt, Front. Energy Res. 6 (2018).

[185] P.B. Petersen, R.J. Saykally, On the nature of ions at the liquid water surface, Annual review of physical chemistry 57 (2006) 333–364.

[186] G. Jones, W.A. Ray, The Surface Tension of Solutions of Electrolytes as a Function of the Concentration. III. Sodium Chloride, J. Am. Chem. Soc. 63 (1941) 3262–3263.

[187] Thomas Hoyer, Personal notice. verbal, 2021.

[188] Z. Wang, Y. Chen, X. Sun, R. Duddu, S. Lin, Mechanism of pore wetting in membrane distillation with alcohol vs. surfactant, Journal of Membrane Science 559 (2018) 183–195.

[189] L. Eykens, I. Hitsov, K. de Sitter, C. Dotremont, L. Pinoy, I. Nopens, B. van der Bruggen, Influence of membrane thickness and process conditions on direct contact membrane distillation at different salinities, Journal of Membrane Science 498 (2016) 353–364.

[190] G.R. Carvalho, F. Chenlo, R. Moreira, J. Telis-Romero, Physicothermal Properties of Aqueous Sodium Chloride Solutions, J Food Process Eng 38 (2015) 234–242.

[191] U. Braukmann, D. Böhme, Salt pollution of the middle and lower sections of the river Werra (Germany) and its impact on benthic macroinvertebrates, Limnologica 41 (2011) 113–124.

[192] J. Kujawa, E. Chrzanowska, W. Kujawski, Transport properties and fouling issues of membranes utilized for the concentration of dairy products by air-gap membrane distillation and microfiltration, Chem. Pap. 73 (2019) 565–582.

[193] A. Hausmann, P. Sanciolo, T. Vasiljevic, E. Ponnampalam, N. Quispe-Chavez, M. Weeks, M. Duke, Direct contact membrane distillation of dairy process streams, Membranes 1 (2011) 48–58.

[194] A. Hausmann, P. Sanciolo, T. Vasiljevic, M. Weeks, K. Schroën, S. Gray, M. Duke, Fouling of dairy components on hydrophobic polytetrafluoroethylene (PTFE) membranes for membrane distillation, Journal of Membrane Science 442 (2013) 149–159.

[195] B.J. James, Y. Jing, X. Dong Chen, Membrane fouling during filtration of milk—a microstructural study, Journal of Food Engineering 60 (2003) 431–437.

[196] H. Rezaei, F.Z. Ashtiani, A. Fouladitajar, Fouling behavior and performance of microfiltration membranes for whey treatment in steady and unsteady-state conditions, Braz. J. Chem. Eng. 31 (2014) 503–518.

[197] E. Guillen-Burrieza, A. Ruiz-Aguirre, G. Zaragoza, H.A. Arafat, Membrane fouling and cleaning in long term plant-scale membrane distillation operations, Journal of Membrane Science 468 (2014) 360–372.

[198] E.M. Thurman, R.L. Wershaw, R.L. Malcolm, D.J. Pinckney, Molecular size of aquatic humic substances, Organic Geochemistry 4 (1982) 27–35.

[199] M. Safavi, T. Mohammadi, High-salinity water desalination using VMD, Chemical Engineering Journal 149 (2009) 191–195.

[200] H.J. Hwang, K. He, S. Gray, J. Zhang, I.S. Moon, Direct contact membrane distillation (DCMD): Experimental study on the commercial PTFE membrane and modeling, Journal of Membrane Science 371 (2011) 90–98.